First Search for Heavy Neutral Leptons with IceCube DeepCore

Dissertation
zur Erlangung des akademischen Grades
doctor rerum naturalium
(Dr. rer. nat.)

im Fach: Physik
Spezialisierung: Experimentalphysik

eingereicht an der
Mathematisch-Naturwissenschaftlichen Fakultät
der Humboldt-Universität zu Berlin

von
Leander Fischer M. Sc.
geboren am 24. Oktober 1992
in Heidelberg

Präsidentin der Humboldt-Universität zu Berlin
Prof. Dr. Julia von Blumenthal

Dekanin der Mathematisch-Naturwissenschaftlichen Fakultät
Prof. Dr. Caren Tischendorf

Colophon
This document was typeset with the help of KOMA-Script and LaTeX using the open-source kaobook template class.

The source code of this thesis is available at:
https://github.com/LeanderFischer/phd_thesis

Foreword

Before diving into the scientific content of my work, I would like to give some editorial remarks to smoothen the reading experience. Throughout the thesis, acronyms and experiment names are introduced in *italic font*, the first time they are mentioned, but are used in normal font from then on. The same goes for software packages, which are initially mentioned in SMALL CAPS FONT. One of the key features of the kaobok template - the big margin - is put to good use to house tables, figures, and additional notes, but also to highlight selected references. Of course, all references are listed in their full extent in the bibliography at the end, but additionally, some (but not necessarily all) of them will be highlighted in the margin next to where they appear to allow for an uninterrupted flow of reading.

Abstract

The observation of neutrino oscillations has established that neutrinos have non-zero masses. This phenomenon is not explained by the *standard model (SM)* of particle physics, but one viable explanation to this dilemma is the existence of *heavy neutral leptons (HNLs)* in the form of right-handed neutrinos. Depending on their mass and coupling to SM neutrinos, these particles could also play an important role in solving additional unexplained observations such as *dark matter (DM)* and the *baryon asymmetry of the universe (BAU)*. This work presents the first search for HNLs with the IceCube Neutrino Observatory. The standard three flavor neutrino model is extended by adding a fourth GeV-scale mass state and allowing mixing with the tau neutrino through the mixing parameter $|U_{\tau 4}|^2$. Three HNL mass values, m_4, of 0.3 GeV, 0.6 GeV, and 1.0 GeV are tested using ten years of data, collected between 2011 and 2021, resulting in constraints for the mixing parameter of $|U_{\tau 4}|^2 < 0.19$ ($m_4 = 0.3\,\text{GeV}$), $|U_{\tau 4}|^2 < 0.36$ ($m_4 = 0.6\,\text{GeV}$), and $|U_{\tau 4}|^2 < 0.40$ ($m_4 = 1.0\,\text{GeV}$) at 90 % confidence level. No significant signal of HNLs is observed for any of the tested masses. This first analysis lays the fundamental groundwork for future searches for HNLs in IceCube.

Zusammenfassung

The observation of neutrino oscillations has established that neutrinos have non-zero masses. This phenomenon is not explained by the *standard model (SM)* of particle physics, but one viable explanation to this dilemma is the existence of *heavy neutral leptons (HNLs)* in the form of right-handed neutrinos. Depending on their mass and coupling to SM neutrinos, these particles could also play an important role in solving additional unexplained observations such as *dark matter (DM)* and the *baryon asymmetry of the universe (BAU)*. This work presents the first search for HNLs with the IceCube Neutrino Observatory. The standard three flavor neutrino model is extended by adding a fourth GeV-scale mass state and allowing mixing with the tau neutrino through the mixing parameter $|U_{\tau 4}|^2$. Three HNL mass values, m_4, of 0.3 GeV, 0.6 GeV, and 1.0 GeV are tested using ten years of data, collected between 2011 and 2021, resulting in constraints for the mixing parameter of $|U_{\tau 4}|^2 < 0.19$ ($m_4 = 0.3\,\text{GeV}$), $|U_{\tau 4}|^2 < 0.36$ ($m_4 = 0.6\,\text{GeV}$), and $|U_{\tau 4}|^2 < 0.40$ ($m_4 = 1.0\,\text{GeV}$) at 90 % confidence level. No significant signal of HNLs is observed for any of the tested masses. This first analysis lays the fundamental groundwork for future searches for HNLs in IceCube.

Todo list

Contents

1 Introduction

Write introduction (RED)

The observation of neutrino oscillations has established that neutrinos have non-zero masses. This phenomenon is not explained by the standard model of particle physics, but one viable explanation to this dilemma is the existence of *heavy neutral leptons (HNLs)*, in the form of right-handed neutrinos with masses much larger than the observed neutrino masses ($\gg$eV). Depending on their mass and coupling to standard model neutrinos, these particles could also play an important role in solving further problems such as baryogenesis or serve as dark matter candidates.

This work presents the first search for HNLs with the IceCube Neutrino Observatory. The standard three flavor neutrino model is extended by adding a fourth GeV-scale mass state and allowing mixing with the tau neutrino through the mixing parameter $|U_{\tau 4}|^2$. The strength of this mixing is tested using atmospheric neutrinos as a source flux. Muon neutrinos that oscillated into tau neutrinos can produce HNLs through neutral current interactions, which then decay back to standard model particles. Both production and decay may produce observable light in the detector, leading to a unique signature of two cascades at low energies.

The measurement is performed through a binned, maximum likelihood fit, comparing the observed data to the expected events from atmospheric neutrinos and HNLs. Three HNL mass values, m_4, of 0.3 GeV, 0.6 GeV, and 1.0 GeV are tested using ten years of data, collected between 2011 and 2021. The fits constrain the mixing parameter to $|U_{\tau 4}|^2 < 0.19$ ($m_4 = 0.3$ GeV), $|U_{\tau 4}|^2 < 0.36$ ($m_4 = 0.6$ GeV), and $|U_{\tau 4}|^2 < 0.40$ ($m_4 = 1.0$ GeV) at 90 % confidence level. No significant signal of HNLs is observed for any of the tested masses, and the best fit mixing values obtained are consistent with the null hypothesis of no mixing.

Additionally, a thorough investigation of the unique low energy double cascade signature of HNLs in IceCube is performed. A benchmark reconstruction performance is estimated using a well established IceCube reconstruction tool, after optimizing it for low energy double cascade events. The limitations of the detector to observe these events are identified, and their origins are discussed. This first analysis lays the fundamental groundwork for future searches for HNLs in IceCube.

notes for the introduction

- observation of non-zero neutrino masses indicates likely existence of new physics beyond the standard model
- multiple SM neutral fermions (right handed) could explain the neutrino masses and their smallness
- if they are heavy enough to not be produced in oscillations, they are called heavy neutral laptons
-
- In 1984 the PS191 [G. Bernardi et al., Phys. Lett. B 166, 479 (1986), G. Bernardi et al., Phys. Lett. B 203, 332 (1988)] experiment at CERN

appears to have been the earliest beam dump to report HNL bounds from the direct production and decay.

- ►

During my time at desy and in IceCube, I have been involved in several projects, which are not all directly related to the main analysis presented in this thesis. I will give a brief overview of my scientific contributions and how they are related to the main analysis.

In close collaboration with a former colleague (Alex Trettin), we developed a novel method to treat detector uncertainty effects in IceCube, which we documented in a few author paper, and which is now one of the default method to incorporate detector uncertainties in atmospheric neutrino analyses in IceCube. This method will also be used in the main analysis of this thesis and is briefly introduced in Section 7.2.3.

Throughout the last years, I was also involved in updating and maintaining the open source analysis framework PISA, which is used in many analyses.

Work related (what is my original work):

- ► the model independent simulation chain described in Section 4.1 was developed exclusively by myself
- ► for the model dependent generator presented in Section **??**, the skeletal structure was constructed by collaborators, before I took over and implemented the full model dependent simulation chain, including the correct decay widths calculations, custom cross-section, and the weighting scheme, continuously optimizing and testing it, before producing and processing the full samples for the main analysis
- ► both the study on how well IceCube can detect low energy double cascades in Chapter 6 and the main analysis in Chapter **??** were developed and performed by myself independently and are original work

[1]: Pauli (1978), "Dear radioactive ladies and gentlemen"

The neutrino was postulated by Wolfgang Pauli [1] in 1930 to explain the continuous energy spectrum of electrons originating from beta decay. Cowan and Reines confirmed this prediction of a light, neutral particle in 1956 when they discovered the electron neutrino using inverse beta decay [2]. Two additional neutrino flavors were found in the following years, and with the discovery of the muon neutrino in 1962 [3] and the tau neutrino in 2001 [4], the current theory of neutrinos in the standard model (SM) was established.

[2]: Cowan et al. (1956), "Detection of the Free Neutrino: a Confirmation"

[3]: Danby et al. (1962), "Observation of High-Energy Neutrino Reactions and the Existence of Two Kinds of Neutrinos"

[4]: Kodama et al. (2001), "Observation of tau neutrino interactions"

Although neutrinos were first believed to be massless, experimental evidence showing the existence of mixed neutrino states started to appear in the 1960s [5]. Mixing between different physical representations of neutrinos is proof for differences in their masses. The resulting phenomenon of neutrino oscillations can be incorporated into the standard model by extending it to include massive neutrinos. How massive they are and how strong is the mixing between neutrino states has to be obtained from measurement. Today there are a variety of precision oscillation experiments using solar, reactor and atmospheric neutrinos to tighten the constraints on the neutrino oscillation parameters. IceCube is one of those leading experiments probing the oscillation theory with atmospheric neutrinos.

[5]: Davis et al. (1968), "Search for Neutrinos from the Sun"

[6]: Aartsen et al. (2017), "The IceCube Neutrino Observatory: instrumentation and online systems"

The IceCube Neutrino Observatory [6] was constructed between 2004 and 2010 at the geographic South Pole. It is the first cubic kilometer Cherenkov

neutrino detector and consists of 5160 optical sensors attached to 86 strings, drilled down to a maximum depth of $\sim$ 2500 m into the Antarctic ice. Neutrinos are detected by the Cherenkov light that is emitted by secondary particles produced in neutrino-nucleon scattering interactions in the ice. With DeepCore, a more densely instrumented sub-array of IceCube, the neutrino detection energy threshold can be lowered to approximately 5 GeV.

At these energies, the similarity in event signatures poses difficulties in identifying different neutrino flavor interactions. Muon neutrino charged-current interactions produce light tracks as opposed to charged-current interactions of electron and tau neutrinos as well as neutral-current interactions of all neutrinos that produce light cascades. The sparse instrumentation of IceCube makes it more challenging to separate track- and cascade-like events. In this thesis, a novel method to distinguish those two event types is developed. In contrast to previously used univariate separation techniques, the multivariate machine learning method applied here maximizes the use of information from the detector response. Through the use of a Gradient Tree Boosting algorithm the separation of events in track and cascade is improved. As a result of the improved separation, the uncertainty to the atmospheric neutrino oscillation parameters Δm^2_{32} and θ_{23} is significantly reduced.

Standard Model Neutrinos and Beyond

2

2.1 The Standard Model

The SM of particle physics is a Yang-Mills theory [7] providing very accurate predictions of weak, strong, and *electromagnetic (EM)* interactions. It is a relativistic quantum field theory that relies on gauge invariance, where all matter is made up of fermions, which are divided into quarks and leptons, and bosons describe the interactions between the fermions that have to fulfil the overall symmetry of the theory. Leptons are excitations of Dirac-type fermion fields.

[7]: Yang et al. (1954), "Conservation of Isotopic Spin and Isotopic Gauge Invariance"

The initial idea of the theory is associated with the works of Weinberg [8], Glashow [9], and Salam [10], that proposed a unified description of EM and weak interactions as a theory of a spontaneously broken SU(2) x U(1) symmetry for leptons, predicting a neutral massive vector boson Z^0, a massive charged vector boson $W^{\pm}$, and a massless photon γ as the gauge bosons. The Higgs mechanism [11], describing the breaking of the symmetry, predicts the existence of an additional scalar particle, the Higgs boson, giving the $W^{\pm}$ and Z^0 bosons their mass. The Higgs boson was discovered in 2012 at the LHC [12, 13].

[8]: Weinberg (1967), "A Model of Leptons"
[9]: Glashow (1961), "Partial-symmetries of weak interactions"
[11]: Higgs (1964), "Broken symmetries, massless particles and gauge fields"
[12]: Chatrchyan et al. (2012), "Observation of a New Boson at a Mass of 125 GeV with the CMS Experiment at the LHC"
[13]: Aad et al. (2012), "Observation of a new particle in the search for the Standard Model Higgs boson with the ATLAS detector at the LHC"

Gell-Mann and Zweig proposed the quark model in 1964 [14, 15], which was completed by the discovery of non-abelian gauge theories [16] to form the SU(3) symmetry of the strong interaction called *quantum chromodynamics (QCD)*. QDC describes the interaction between quarks and gluons which completed the full picture of the SM in the mid-1970s. Together with the electroweak theory, the SM is a $SU(3)_C$ x $SU(2)_L$ x $U(1)_Y$ local gauge symmetry, with the conserved quantities C, *color*, L, *left-handed chirality*, and Y, *weak hypercharge*

[14]: Gell-Mann (1964), "A Schematic Model of Baryons and Mesons"
[15]: Zweig (1964), "An SU(3) model for strong interaction symmetry and its breaking. Version 2"

In the following, the basic properties of the SM are described, following the derivations of [17, 18].

[17]: Giunti et al. (2007), *Fundamentals of Neutrino Physics and Astrophysics*
[18]: Schwartz (2013), *Quantum Field Theory and the Standard Model*

2.1.1 Fundamental Fields

Fermions in the SM are Weyl fields with either *left-handed (LH)* or *right-handed (RH)* chirality, meaning they are eigenvectors of the chirality operator γ_5 with $\gamma_5\psi_{R/L} = \pm\psi_{R/L}$. Only LH particles transform under $SU(2)_L$. The Higgs field is a complex scalar field, a doublet of $SU(2)_L$, which is responsible for the spontaneous symmetry breaking of $SU(2)_L$ x $U(1)_Y$ to $U(1)_{EM}$. Local gauge transformations of the fields are given by

$$\psi \rightarrow e^{ig\theta^a(x)T^a}\psi \ , \tag{2.1}$$

where g is the coupling constant, $\theta^a(x)$ are the parameters of the transformation, and T^a are the generators of the group, with a counting them. The number of bosons is dependent on the generators of the symmetry groups, while the strength is defined by the coupling constants. There are eight massless gluons corresponding to the generators of the $SU(3)_C$ group. These

mediate the strong force which conserves color charge. The W_1, W_2, W_3, and B boson fields of the SU(2)$_L$ x U(1)$_Y$ group are mixed into the massive bosons through spontaneous symmetry breaking as

$$W^{\pm} = \frac{1}{\sqrt{2}}(W_1 \mp iW_2) \tag{2.2}$$

and

$$Z^0 = \cos\theta_W W_3 - \sin\theta_W B \ , \tag{2.3}$$

with θ_W being the *Weinberg angle*. The massless photon field is given by

$$A = \sin\theta_W W_3 + \cos\theta_W B \tag{2.4}$$

and its conserved quantity is the EM charge Q, which depends on the weak hypercharge, Y, and the third component of the weak isospin, T_3, as $Q = T_3 + Y/2$.

	Type			Q
quarks	u	c	t	+2/3
	d	s	b	-1/3
leptons	ν_e	ν_μ	ν_τ	0
	e	μ	τ	-1

Table 2.1: Fermions in the Standard Model. Shown are all three generations of quarks and leptons with their electric charge Q.

Fermions are divided into six quarks and six leptons. Weak, strong, and EM force act on the quarks, and they are always found in bound form as baryons or mesons. Leptons do not participate in the strong interaction and only the electrically charged leptons are massive and are effected by the EM force, while neutrinos are massless and only interact via the weak force. Each charged lepton has an associated neutrino, which it interacts with in *charged-current (CC)* weak interactions, that will be explained in more detail in Section 2.1.4. The fermions are listed in Table 2.1.

2.1.2 Electroweak Symmetry Breaking

To elaborate the process of spontaneous symmetry breaking through which the gauge bosons of the weak interaction acquire their masses, the Lagrangian of the Higgs field is considered as

$$\mathscr{L}_{\text{Higgs}} = (D_\mu\Phi^\dagger)(D^\mu\Phi) - \lambda\left(\Phi^\dagger\Phi - \frac{v^2}{2}\right)^2 \ , \tag{2.5}$$

with parameters λ and v, where λ is assumed to be positive. Φ is the Higgs doublet, which is defined as

$$\Phi = \begin{pmatrix} \Phi^+ \\ \Phi^0 \end{pmatrix} , \tag{2.6}$$

with the charged component Φ^+ and the neutral component Φ^0. The covariant derivative is given by

$$D_\mu = \partial_\mu - ig_2\frac{\sigma^i}{2}W_\mu^i - \frac{1}{2}ig_1B_\mu \ , \tag{2.7}$$

with the Pauli matrices σ^i and the gauge boson fields W_μ^i and B_μ of the SU(2)$_L$ and U(1)$_Y$ groups, respectively. The coupling constants g_2 and g_1 are the respective coupling constants which are related to the Weinberg angle as $\tan\theta_W = \frac{g_1}{g_2}$. The Higgs potential has a non-zero *vacuum expectation value (vev)* at the minimum of the potential at $\Phi^\dagger\Phi = \frac{v^2}{2}$. Since the vacuum is electrically neutral, it can only come from a neutral component of the Higgs

doublet as

$$\Phi_{\text{vev}} = \frac{1}{\sqrt{2}}\begin{pmatrix}0\\ v\end{pmatrix}. \tag{2.8}$$

2.1.3 Fermion Masses

The mass term for charged fermions with spin-1/2 is given by

$$\mathcal{L}_{\text{Dirac}} = m(\bar{\Psi}_R\Psi_L - \bar{\Psi}_L\Psi_R)\,, \tag{2.9}$$

composed of the product of LH and RH Weyl spinors $\Psi_{L/R}$. This term is not invariant under SU(2)$_L$ x U(1)$_Y$ gauge transformations, but adding a Yukawa term

$$\mathcal{L}_{\text{Yukawa}} = -Y^e\bar{L}_L\Phi e_R + h.c.\,, \tag{2.10}$$

coupling the fermion fields e_R to the Higgs field Φ, recovers the invariance and gives the fermions their masses. Here, Y^e is the Yukawa coupling constant and $\bar{L}_L$ is the SU(2)$_L$ doublet. With the vev, this results in the mass term for the charged leptons and down-type quarks of $-m_e(\bar{e}_L e_R + \bar{e}_R e_L)$ with $m_e = \frac{Y^e v}{\sqrt{2}}$. With $\tilde{\Phi} = i\sigma_2\Phi^*$, a similar Yukawa term can be written as $-Y^u\bar{L}_L\tilde{\Phi}u_R + h.c.$, which leads to the masses of the up-type quarks.

2.1.4 Leptonic Weak Interactions after Symmetry Breaking

After the spontaneous symmetry breaking, the leptonic part of the electroweak Lagrangian can be written as

$$\mathcal{L}^{\ell}_{\text{EW}} = \frac{g}{\sqrt{2}}W^+\sum_{\alpha=e,\mu,\tau}\bar{\nu}_\alpha\gamma^\mu P_L\ell_\alpha + \frac{g}{4c_w}Z \times\left\{\sum_{\alpha=e,\mu,\tau}\bar{\nu}_\alpha\gamma^\mu P_L\nu_\alpha + \sum_\alpha\bar{\ell}_\alpha\gamma^\mu\left[2s_w^2P_R - (1-2s_w^2)P_L\right]\ell_\alpha\right\} + h.c.\,, \tag{2.11}$$

where $c_w \equiv \cos\theta_w$, $s_w \equiv \sin\theta_w$, P_L and P_R are the left and right projectors, respectively, while ν_α and ℓ_α, are the neutrino and charged lepton weak eigenstates. The W^+ and Z bosons are the massive gauge bosons of the weak interaction. The large boson masses $m_W \sim 80\,\text{GeV}$ and $m_Z \sim 90\,\text{GeV}$ result in a short range of the force of about 1×10^{-18} m. Interactions carried out by the $W^\pm$ bosons are called *charged current (CC)* interactions, as they propagate a charge, therefore changing the interacting lepton to its charged/neutral counterpart. *Neutral current (NC)* interactions are those mediated by the Z^0 boson, where no charge is transferred. NC interactions couple neutrinos to neutrinos and charged leptons to charged leptons, but not to each other. The Feynman diagrams for CC and NC interactions are shown in Figure 2.1.

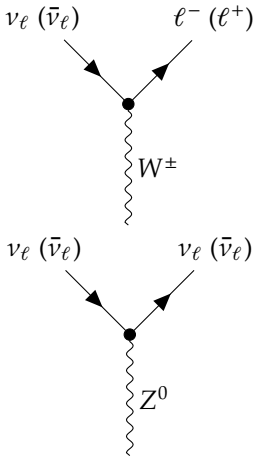

Figure 2.1: Feynman diagrams of charged-current (top) and neutral-current (bottom) neutrino weak interactions, modified from [19].

2.2 Beyond the Standard Model

The fundamentals of the SM described above **are not** enough to explain all observed phenomena. Gravity cannot be explained by the SM, as it is incompatible with general relativity, neither can some of the cosmological observations like DM, and the matter-antimatter asymmetry be explained. But most importantly, the SM does not predict neutrinos to have mass, which

is experimentally proven by neutrino oscillations, so some extension to the SM is needed in order to explain the observed phenomena.

The standard cosmological model ΛCDM [20] assumes that equal amounts of matter and anti-matter were produced in the early universe. However, the universe today is dominantly made up of matter. This BAU can be measured by the difference between the number densities of baryons and anti-baryons normalized to the number density of photons as

$$\eta_B = \frac{n_B - n_{\bar{B}}}{n_\gamma} \,, \tag{2.12}$$

where n_B, $n_{\bar{B}}$, and n_γ are the number densities of baryons, anti-baryons, and photons, respectively. Baryons are the dominant component with η_B being observed to be at the order of 10^{-9} [21]. Leptogenesis and EW baryogenesis are scenarios that could explain this phenomenon, where the former could be realized by the existence of heavy RH neutrinos [22].

The observation of neutrino flavor conversions and neutrino oscillations in a multitude of experiments [5, 23, 24] is the strongest evidence for physics *beyond the standard model (BSM)* measured in laboratories to date. The observation that neutrinos change their flavor while they propagate through space can only be explained, if at least two neutrinos have a non-zero mass. From those measurements we know the mass differences are very small as compared to the lepton masses, but neither their existence, nor their smallness is predicted by the SM. There are upper limits on the sum of all neutrino masses from cosmological observations at 1.2 eV [25, 26] and at 0.8 eV from the KATRIN experiment [27]. Adding RH neutrino states to the theory could explain the origin of the observed non-zero neutrino masses and could be tested for by searching for corresponding signatures in experiments.

highlight a few more neutrino related open questions, to circle back to related to the HNL searches maybe? (YELLOW)

2.2.1 Mass Mechanisms

Since there are no RH neutrinos in the SM, the mass mechanism described in Section 2.1.3, which couples the Higgs field to LH and RH Weyl fields, predicts the LH neutrinos to be massless. From experimental observations it is known that at least two of the three neutrino generations need to have a non-zero mass. Assuming the existence of RH neutrinos fields ν_R, one way of producing the neutrino masses is by adding a Yukawa coupling term similar to the one for up-type quarks mentioned in Section 2.1.3, to write the full Yukawa Lagrangian as

$$\mathcal{L}_{\text{Yukawa}} = -Y^e_{ij} \bar{L}^i_L \Phi e^j_R - Y^\nu_{ij} \bar{L}^i_L \tilde{\Phi} \nu^j_R + h.c. \,, \tag{2.13}$$

with i, j running over the three generations of leptons e, μ, and τ, and Y^e and Y^ν being the Yukawa coupling matrices. Diagonalizing the Yukawa coupling matrices through unitary transformations U^e and U^ν leads to the **Dirac mass term** in the mass basis as

$$\mathcal{L}^{\text{mass}}_{\text{Dirac}} = \frac{v}{\sqrt{2}} \left(\bar{e}_L M_e e_R - \bar{\nu}_L M_\nu \nu_R \right) \,, \tag{2.14}$$

where M_e and M_ν are the diagonal mass matrices of leptons and neutrinos, respectively. A purely Dirac mass term would not explain the smallness of

[20]: Deruelle et al. (2018), *Relativity in Modern Physics*

[21]: Workman et al. (2022), "Review of Particle Physics"

[22]: Fukugita et al. (1986), "Baryogenesis without grand unification"

[5]: Davis et al. (1968), "Search for Neutrinos from the Sun"

[23]: Fukuda et al. (1998), "Evidence for Oscillation of Atmospheric Neutrinos"

[24]: Ahmad et al. (2002), "Direct Evidence for Neutrino Flavor Transformation from Neutral-Current Interactions in the Sudbury Neutrino Observatory"

[25]: Alam et al. (2021), "Completed SDSS-IV extended Baryon Oscillation Spectroscopic Survey: Cosmological implications from two decades of spectroscopic surveys at the Apache Point Observatory"

[26]: Aghanim et al. (2020), "Planck2018 results: VI. Cosmological parameters"

[27]: Aker et al. (2022), "Direct neutrino-mass measurement with sub-electronvolt sensitivity"

the neutrino masses in a straightforward way. Only fine-tuning the Yukawa coupling constants to small values would lead to small neutrino masses.

An additional way of generating neutrino masses is by adding a Majorana mass term of the form

add Majorana condition and mention what this means for interactions (LNV of 2) (ORANGE)

$$\mathcal{L}_{\text{Majorana}} = -\frac{1}{2} M_{ij} (\nu_R^i)^c \nu_R^j + h.c. \,, \tag{2.15}$$

with M_{ij} being the Majorana mass matrix and the indices i, j running over all n_R RH neutrino generations. The superscript c denotes the charge conjugate field. Combining the charge conjugated RH neutrino fields with the LH neutrino fields as

$$\boldsymbol{N} = \begin{pmatrix} \boldsymbol{\nu}_L \\ \boldsymbol{\nu}_R^c \end{pmatrix} , \tag{2.16}$$

with $\boldsymbol{\nu}_R$ containing the n_R RH fields. The full neutrino mass Lagrangian is then given by the combined **Dirac and Majorana mass term** as

$$\mathcal{L}^{\text{mass},\nu}_{\text{Dirac+Majorana}} = \frac{1}{2} \boldsymbol{N}^T \hat{C} M^{\text{D+M}} \boldsymbol{N} + h.c. \,, \tag{2.17}$$

and the mass matrix is given by

$$M^{\text{D+M}} = \begin{pmatrix} 0 & (M^D)^T \\ M^D & M^R \end{pmatrix} . \tag{2.18}$$

On top of explaining the origin of neutrino masses itself, a combined Dirac and Majorana mass term could also solve the question of their smallness. If the mass of the RH neutrinos is very large, the masses of the active neutrino flavors is suppressed, which is known as *see-saw mechanism*.

Discuss lepton number conservation (pure dirac) and lepton number violation (dirac+majorana) (ORANGE)

2.2.2 Minimal Extensions and the νMSM

So far we have described neutrinos in their flavor eigenstates, which are relevant for weak interactions, where the three weak flavor states ν_e, ν_μ, and ν_τ are related to the charged leptons they interact with in CC interactions. In order to *just* explain the three oscillating flavor eigenstates, three mass states are needed, which are related to the flavor eigenstates by the unitary, 3x3 *Pontecorvo-Maki-Nakagawa-Sakata (PMNS)* mixing matrix U, where the flavor states are a superposition of the mass states as

$$|\nu_\alpha\rangle = \sum_k U^*_{\alpha k} |\nu_k\rangle \ , \tag{2.19}$$

with the weak flavor states $|\nu_\alpha\rangle$, $\alpha = e, \mu, \tau$, and the mass states $|\nu_k\rangle$ with $k = 1, 2, 3$. In its generic form the PMNS matrix is given by

$$U = \begin{pmatrix} U_{e1} & U_{e2} & U_{e3} \\ U_{\mu 1} & U_{\mu 2} & U_{\mu 3} \\ U_{\tau 1} & U_{\tau 2} & U_{\tau 3} \end{pmatrix} , \tag{2.20}$$

which will be the basis for the discussion of neutrino oscillations in Section 2.3.2.

This however is not enough to explain the neutrino masses observed in oscillation experiments. The most minimal model required to give rise to two non-zero active neutrino masses, is an additional two RH neutrinos,

assuming the mass of the lightest SM neutrino is zero. If the additional neutrino states have masses ≫eV they are referred to as HNL, which are almost sterile, with a small mass mixing with the active neutrinos.

But the SM also fails to explain additional observations of physics beyond the standard model (BAU, DM), which could be solved by the *neutrino minimal standard model (νMSM)* [28, 29]. In the νMSM, three RH neutrinos are added, where two of them are heavy, to explain the observed neutrino masses and oscillations, and a third one is light and serves as a DM candidate. The mixing between mass and flavor eigenstates is then described by an extended 6x6 mixing matrix as

[28]: Asaka et al. (2005), "The nuMSM, dark matter and neutrino masses"
[29]: Asaka et al. (2005), "The νMSM, dark matter and baryon asymmetry of the universe"

elaborate on Leptogenesis in νMSM and sterile neutrino DM, or link some papers? (ORANGE)

$$\begin{pmatrix} \nu_e \\ \nu_\mu \\ \nu_\tau \\ N_1 \\ N_2 \\ N_3 \end{pmatrix} = \begin{pmatrix} U_{e1} & U_{e2} & U_{e3} & U_{e4} & U_{e5} & U_{e6} \\ U_{\mu 1} & U_{\mu 2} & U_{\mu 3} & U_{\mu 4} & U_{\mu 5} & U_{\mu 6} \\ U_{\tau 1} & U_{\tau 2} & U_{\tau 3} & U_{\tau 4} & U_{\tau 5} & U_{\tau 6} \\ U_{N_1 1} & U_{N_1 2} & U_{N_1 3} & U_{N_1 4} & U_{N_1 5} & U_{N_1 6} \\ U_{N_2 1} & U_{N_2 2} & U_{N_2 3} & U_{N_2 4} & U_{N_2 5} & U_{N_2 6} \\ U_{N_3 1} & U_{N_3 2} & U_{N_3 3} & U_{N_3 4} & U_{N_3 5} & U_{N_3 6} \end{pmatrix} \begin{pmatrix} \nu_1 \\ \nu_2 \\ \nu_3 \\ \nu_4 \\ \nu_5 \\ \nu_6 \end{pmatrix}, \tag{2.21}$$

where N_i and ν_{i+3} ($i \in [1, 2, 3]$) are the sterile flavor states and the additional RH mass states, respectively. In the νMSM, the two heavy RH neutrinos generate the active neutrino masses through the type I seesaw mechanism [30–34], where they are assumed to be SM scalars and couple to the Higgs field as such.

[30]: Minkowski (1977), "$\mu \to e\,\gamma$ at a rate of one out of 10^9 muon decays?"
[31]: Yanagida (1980), "Horizontal Symmetry and Masses of Neutrinos"
[32]: Glashow (1980), "The Future of Elementary Particle Physics"
[33]: Gell-Mann et al. (1979), "Complex Spinors and Unified Theories"
[34]: Mohapatra et al. (1980), "Neutrino Mass and Spontaneous Parity Nonconservation"

I think here I'd want the extended leptonic EW lagrangien, so I can explain the mass mixing and the interactions it opens up (RED)

2.2.3 Observational Avenues for Right-Handed Neutrinos

If the RH neutrinos have masses at the eV scale, they can be observed through distortion effects in measurements of neutrino oscillation experiments. Several analyses looking for these so-called light sterile neutrinos exist in IceCube, where [35] is using atmospheric neutrinos in the higher energy range of 500 GeV to 10 000 GeV and [19] is using the lower energy region of 6 GeV to 156 GeV. The latter work includes a detailed description of the expected oscillation effects and the various anomalies observed in oscillation experiments that could be explained by the existence of a light sterile neutrino, which is not covered in this work.

[35]: Aartsen et al. (2020), "eV-Scale Sterile Neutrino Search Using Eight Years of Atmospheric Muon Neutrino Data from the IceCube Neutrino Observatory"
[19]: Trettin (2023), "Search for eV-scale sterile neutrinos with IceCube DeepCore"

Here, the focus will be on heavy RH neutrinos, interchangeably also called heavy sterile neutrinos, or HNLs. A defining property is that they are too massive to be produce in oscillations and to be observed as distortions thereof. Several ways to observe HNLs are possible through direct production and decay experiments, which will be discussed in the following. Most of the existing searches assume the minimal model, where only one coupling between the new mass states and the SM neutrinos is non-zero and the coupling is just through mass mixing in a type I seesaw scenario, but more complex scenarios are of course also possible and might produce various additional signatures, or stronger signals.

In general, the constraints discussed in the following are based on models, where only the coupling between the HNL and one SM flavor is non-zero. While this is the straight forward approach to test the mixing parameters individually, this might make the constraints stronger than they would be in a more complex scenario, where the HNLs couple to more than one SM flavor as was show in [36] for collider bounds.

[36]: Tastet et al. (2021), "Reinterpreting the ATLAS bounds on heavy neutral leptons in a realistic neutrino oscillation model"

Extracted Beamline Searches

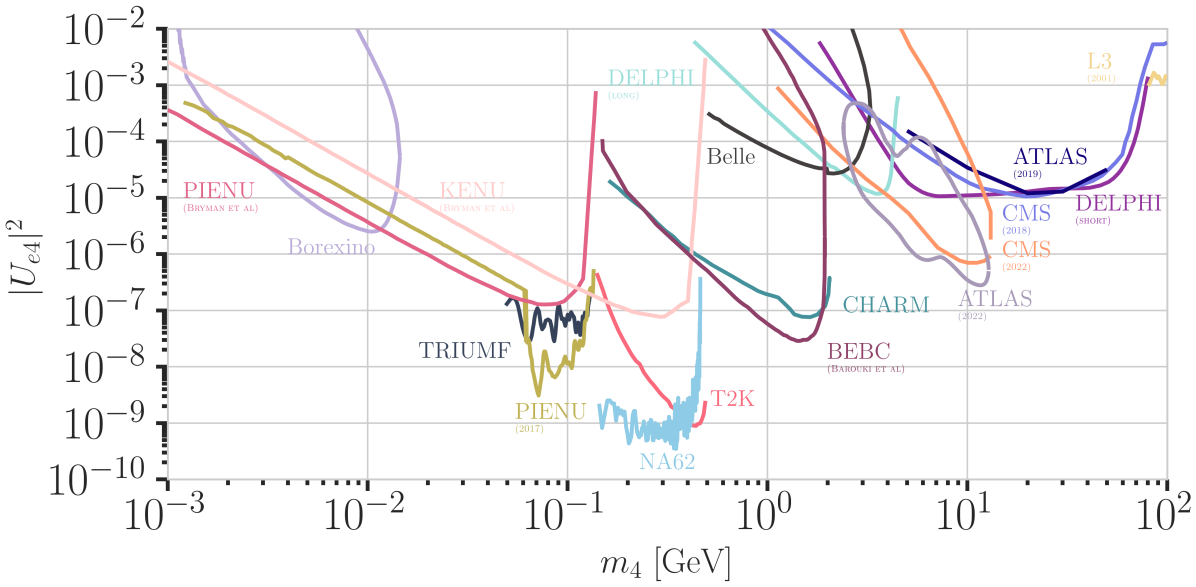

Figure 2.2: Current leading $|U_{e4}^2| - m_4$ limits from PIENU [37, 38], BOREXINO [39], KENU , TRIUMF [40], NA62 [41], T2K [42], DELPHI [43], BEBC [44], Belle , L3 , CHARM [45], ATLAS [46, 47], CMS [48, 49], and NuTeV [50]. Modified from [51].

mention KENU, Belle, L3 in the text and add references (RED)

Protons interacting with a target or a beam dump can produce pions, kaons, and heavy-quark hadrons, whose subsequent decays would also produce HNLs. The energies of the HNLs produced in those interactions are between 1 MeV and 4 GeV and could decay at several distances, depending on their lifetime, which is model dependent. Experiments along the extracted beamline, which are using a spectrometer with particle identification, can search for unique decay signatures at displaced vertices. Example signatures are $\nu_4 \to l_\alpha \pi$, $\nu_4 \to l_\alpha^+ l_\alpha^-$, or $\nu_4 \to \nu\pi^0$ (or other neutral mesons), which cannot be explained by SM neutrinos. Depending on the decay channel, a specific mixing can be probed. The other way of searching for HNLs with these interactions is to look for peaks in the missing mass spectrum, measured around the production vertex at the target, which usually is not possible for beam dumps, as the beam dump region is not calorimetrically instrumented.

HNL search pioneer work was done by experiments at extracted beam lines, with first results from *PS191* [52] and *CHARM* [45], reporting bounds from direct production and decay of HNLs for $|U_{e4}|^2$, $|U_{\mu 4}|^2$, and combinations of them, at masses from 10 MeV to 500 MeV at orders of 10^{-3} to 10^{-6}. Since then, there has been and still is a large activity of searches for HNLs at extracted beamlines and the strongest bounds on $|U_{e4}|^2$ and $|U_{\mu 4}|^2$ are currently set by *PIENU* [37, 38, 53], *TRIUMF* [40], *NA62* [41], *T2K* [42], *BNL-E949* [54], *MicroBooNE* [55], and *NuTev* [50] in the mass range from 1 MeV to 4 GeV, reaching from 10^{-4} at the lower mass to 10^{-9} at 4 at the highest masses. The current strongest bounds are shown in Figure 2.2 and Figure 2.3, which also shows bounds from other experiments, which will be discussed in the following.

Especially noteworthy are the results of analyses probing the mixing with the third lepton generation, $|U_{\tau 4}|^2$, from *NOMAD* [56] and reinterpretations of the CHARM results and the BEBC results in the context of the mixing

[52]: Bernardi et al. (1986), "Search for Neutrino Decay"

[45]: Bergsma et al. (1983), "A Search for Decays of Heavy Neutrinos"

[37]: Bryman et al. (2019), "Constraints on Sterile Neutrinos in the MeV to GeV Mass Range"

[38]: Aguilar-Arevalo et al. (2018), "Improved search for heavy neutrinos in the decay $\pi \to e\nu$"

[53]: Ito et al. (2021), "Search for heavy neutrinos in $\pi^+ \to \mu^+\nu$ decay and status of lepton universality test in the PIENU experiment"

[40]: Britton et al. (1992), "Improved search for massive neutrinos in π + →e + ν decay"

[41]: Parkinson et al. (2022), "Search for heavy neutral lepton production at the NA62 experiment"

[42]: Abe et al. (2019), "Search for heavy neutrinos with the T2K near detector ND280"

[54]: Artamonov et al. (2015), "Search for heavy neutrinos in $K^+ \to \mu^+\nu_H$ decays"

[55]: Abratenko et al. (2024), "Search for Heavy Neutral Leptons in Electron-Positron and Neutral-Pion Final States with the MicroBooNE Detector"

[50]: Vaitaitis et al. (1999), "Search for neutral heavy leptons in a high-energy neutrino beam"

[56]: Astier et al. (2001), "Search for heavy neutrinos mixing with tau neutrinos"

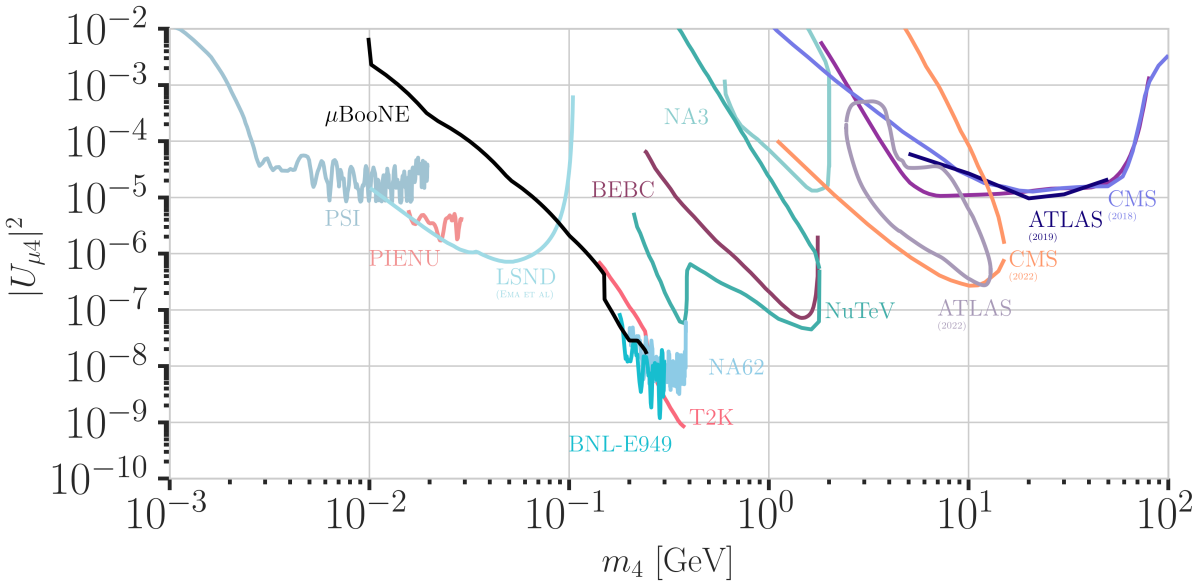

Figure 2.3: Current leading $|U^2_{\mu 4}| - m_4$ limits from PSI , μBooNE [55], PIENU [37], LSND , BNL-E949 [54], NA62 [41], T2K [42], BEBC [59], ATLAS [46, 47], CMS [48, 49], NuTeV [50], and NA3 . Modified from [51]. Modified from [51].

[44]: Barouki et al. (2022), "Blast from the past II: Constraints on heavy neutral leptons from the BEBC WA66 beam dump experiment"
[57]: Orloff et al. (2002), "Limits on the mixing of tau neutrino to heavy neutrinos"
[58]: Boiarska et al. (2021), "Constraints from the CHARM experiment on heavy neutral leptons with tau mixing"

mention PSI, LSND, NA3 in the text and add references (RED)

[46]: Aad et al. (2019), "Search for heavy neutral leptons in decays of W bosons produced in 13 TeV pp collisions using prompt and displaced signatures with the ATLAS detector"
[47]: Aad et al. (2023), "Search for Heavy Neutral Leptons in Decays of W Bosons Using a Dilepton Displaced Vertex in $\sqrt{s}$ = 13TeV pp Collisions with the ATLAS Detector"
[48]: Sirunyan et al. (2018), "Search for heavy neutral leptons in events with three charged leptons in proton-proton collisions at $\sqrt{s}$ = 13 TeV"
[49]: Tumasyan et al. (2022), "Search for long-lived heavy neutral leptons with displaced vertices in proton-proton collisions at $\sqrt{s}$ =13 TeV"
[60]: Shuve et al. (2016), "Revision of the LHCb Limit on Majorana Neutrinos"
[61]: Aaij et al. (2021), "Search for heavy neutral leptons in $W^+ \to \mu^+\mu^\pm$jet decays"

$|U_{\tau 4}|^2$, where the latter is place the most stringent limits from 10^{-3} to 10^{-6} in the 0.1 GeV to 2 GeV range [44, 57, 58]. In Figure 2.4 the current strongest bounds on $|U_{\tau 4}|^2$ are shown.

Collider Searches

So far, collider searches have been conducted at the *large electron positron collider (LEP)* and at the *large hadron collider (LHC)* in proton-proton mode. Strongest results are from the *ATLAS* and *CMS* experiments, which are nearly hermetic, general purpose detectors around the interaction point, and from the *DELPHI* and the *LHCb* experiments, which are forward detectors that can be used to search for new particles in decays of heavy particles produced. In the minimal model, HNLs in the GeV mass range can be produced through mass mixing in decays of heavy mesons, tau leptons, Z/W bosons, H bosons, or top quarks originating from the collisions. Depending on the dirac or majorana nature of the HNL, they can decay to lepton number conserving or lepton number violating channels.

Using prompt and displaced decays of the HNL, both ATLAS and CMS have set constraints on $|U_{e4}|^2$ and $|U_{\mu 4}|^2$ at the level of 10^{-4} to 10^{-6} in the mass range between 1 GeV to 100 GeV [46–49]. The LHCb experiment has HNL search results at HNL masses below and above the W boson mass, where the low mass searches are using the decay channel $B^- \to \pi^+\mu^-\mu^-$, setting limits at the 10^{-3} level for $|U_{\mu 4}|^2$ in the mass range of 0.5 GeV to 3.5 GeV [60]. At high masses, the $W^+ \to \mu^-\mu^\pm$jet channel is used to set limits at the order of 10^{-3} to 10^{-2} for $|U_{\mu 4}|^2$ in the mass range of 5 GeV to 50 GeV in the LNC channel and at the order of 10^{-4} to 10^{-3} in the LNV channel [61].

Nuclear Decays Measurements

A novel approach of searching for irregularities in energy-momentum conservation measurements in nuclear reactions might be a viable way of

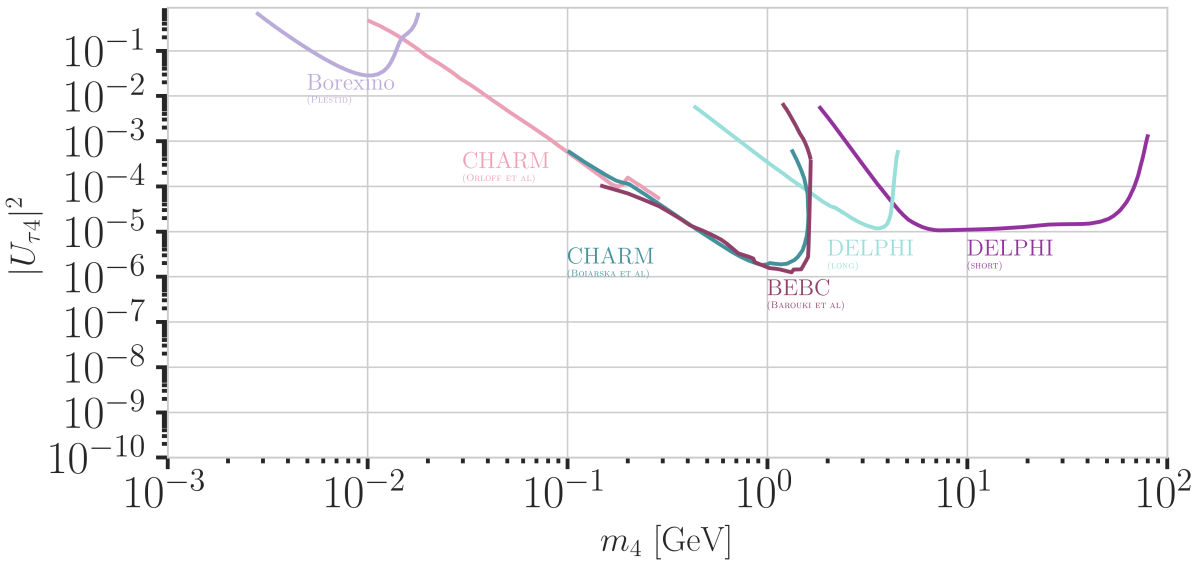

Figure 2.4: Current leading $|U^2_{\tau 4}| - m_4$ limits from BOREXINO [62], CHARM [57, 58], DELPHI [43], and BEBC [44]. Modified from [51].

searching for HNLs, as they could be interpreted as constraints on $|U_{e4}|^2$ and $m4$.

Kinks in **beta decay** spectra would show up at $Q - m_4c^2$, where the HNL mass, $m4$, can be measured between the lower energy detection threshold and the energy released in the decay, which is called Q value. Analyses using the tritium decay, with $Q = 18.6\,\text{keV}$, are planned in *KATRIN* [63] and *TRISTAN* [64] in the 1 keV to 18 keV range. Their projected statistical limits are around $10^{-}7$ for $|U_{e4}|^2$, but will require further detector upgrades [64]. A first result from KATRIN measurements during commissioning sets limits at the order of 10^{-2} to 10^{-3} in the mass range of 0.1 keV to 1.6 keV [65]. *DUNE* is planning to measure the ionization charge of atmospheric argon decays, with $Q = 565\,\text{keV}$, to probe $|U_{e4}|^2$ at in the 20 keV to 450 keV mass range. The projected sensitivity is at the 10^{-5} level, and might improve to 10^{-7} with additional detector improvements [66].

To test for the existence of HNLs using **electron capture** measurements, total energy-momentum reconstruction of all non-neutrino final states is needed. Electron capture is a pure two body decay process, where the recoiling atom and the electron neutrino are the only final state particles, but additional energy is carried away by the de-excitation x-ray or auger electron. The energy-momentum conservation can be probed by measuring the atom and the associated de-excitation products. The mixing $|U_{e4}|^2$ can be probed by looking for a separated non-zero missing mass peak. The *BeEST* experiment has set limits at the 10^{-4} level in the 100 keV to 850 keV mass range, using berillium-7, which has a Q value of 862 keV. After planned upgrades to the experiment, the sensitivity is expected to improve to the 10^{-7} level [67].

Reactor searches up to 12 MeV in mass are possible at short baseline experiments using commercial or research reactors, which are a strong source of electron antineutrinos and could therefore also produce HNLs if $|U_{e4}|^2$ is non-zero. Visible decay channels at these energies are $\nu_4 \to \nu_e e^+ e^-$, $\nu_4 \to \nu\gamma$, and $\nu_4 \to \nu\gamma\gamma$, where the first dominates. The first analysis in this field, reports limits at the 10^{-4} level in the 2 MeV to 7 MeV mass range [68].

mention the Z boson decay results from DELPHI (because they are strong in Utau4, too (RED))

[63]: Osipowicz et al. (2001), "KATRIN: A Next generation tritium beta decay experiment with sub-eV sensitivity for the electron neutrino mass. Letter of intent"

[64]: Mertens et al. (2019), "A novel detector system for KATRIN to search for keV-scale sterile neutrinos"

[65]: Aker et al. (2023), "Search for keV-scale sterile neutrinos with the first KATRIN data"

[66]: Abi et al. (2020), "Deep Underground Neutrino Experiment (DUNE), Far Detector Technical Design Report, Volume II: DUNE Physics"

[67]: Friedrich et al. (2021), "Limits on the Existence of sub-MeV Sterile Neutrinos from the Decay of ^{7}Be in Superconducting Quantum Sensors"

[68]: Hagner et al. (1995), "Experimental search for the neutrino decay v3+vj+e++e- and limits on neutrino mixing"

Atmospheric and Solar

Natural sources of neutrinos are provided up to 20 MeV by the sun and up to 100s of GeV by neutrino production in the atmosphere. Both fluxes contain all flavors of neutrinos, due to mixing and oscillations, and can therefore be used to directly probe the mixings with ν_e, ν_μ, and ν_τ. Depending on the HNL mass and the strength of the mixing, which both govern the decay length, different signatures can be used to experimentally access large regions of the HNL parameter space. The strength of the mixing defines the total rate of HNL events, which is additionally affected by whether solely the minimal mass mixing is assumed, or also more complicated mixing scenarios, like the dipole portal, are considered.

So far, only very few analyses exist, which are performed by the experimental collaborations themselves. Several external theoretical groups have predicted the expected sensitivities to HNLs, produced from solar or atmospheric neutrinos, based on various coupling scenarios and decay lengths. A selection of the potential analyses will be discussed in the following.

For very long-lived particles, **production inside the sun** can be used as a source to search for HNLs in detectors on earth. This will only allow production through non-zero $|U_{e4}|^2$, because the initial solar neutrino flux is only ν_e. By searching for HNL decays to a SM neutrino and an electron positron pair $\nu_4 \to \nu_e e^+ e^-$ and comparing to the expected inter planetery positron flux, *Borexino* has placed the strongest limits on the mixing $|U_{e4}|^2$ a the order of 10^{-5} in the few MeV mass range [39].

[39]: Bellini et al. (2013), "New limits on heavy sterile neutrino mixing in B8 decay obtained with the Borexino detector"

For HNL decay length scales of the order of the Earth's diameter, HNL **up-scattering outside the detector** is possible, where a neutrino from the solar or the atmospheric neutrino flux scatters in the Earth and transfers some kinetic energy into the mass of the HNL, which can then later decay inside the detector. For HNL masses below 18 MeV produced from solar neutrinos, (external) limits were derived using the Borexino data for purely tau coupling through mass mixing [62] and for all flavor coupling through the dipole portal [69]. At similar decay length scales, the HNL could also be produced directly in the atmosphere, but neither this channel, nor the production anywhere in the Earth from atmospheric neutrinos has been investigated yet.

[62]: Plestid (2021), "Luminous solar neutrinos I: Dipole portals"

[69]: Plestid (2021), "Luminous solar neutrinos II: Mass-mixing portals"

If the HNL decay lengths are sufficiently short, **production and decay in the detector** can happen and the observation of two vertices could be used to constrain the mixing parameters. In principle, this could be possible with any neutrino flavor produced in the sun or the atmosphere, but so far only theoretical studies have been performed for mass-mixing and dipole-portal couplings for the atmospheric neutrino detectors *IceCube* [70, 71] and *Super-K*, *Hyper-K*, and Dune [72, 73]. Due to the high complexity of these experiments, several simplified assumptions were made in the studies, which might not hold in reality, and the results should be taken with caution. For reliable sensitivity estimates and limits the collaborations should perform their own analyses.

[70]: Coloma et al. (2017), "Double-Cascade Events from New Physics in Icecube"

[71]: Coloma (2019), "Icecube/DeepCore tests for novel explanations of the MiniBooNE anomaly"

[72]: Atkinson et al. (2022), "Heavy Neutrino Searches through Double-Bang Events at Super-Kamiokande, DUNE, and Hyper-Kamiokande"

[73]: Coloma et al. (2021), "GeV-scale neutrinos: interactions with mesons and DUNE sensitivity"

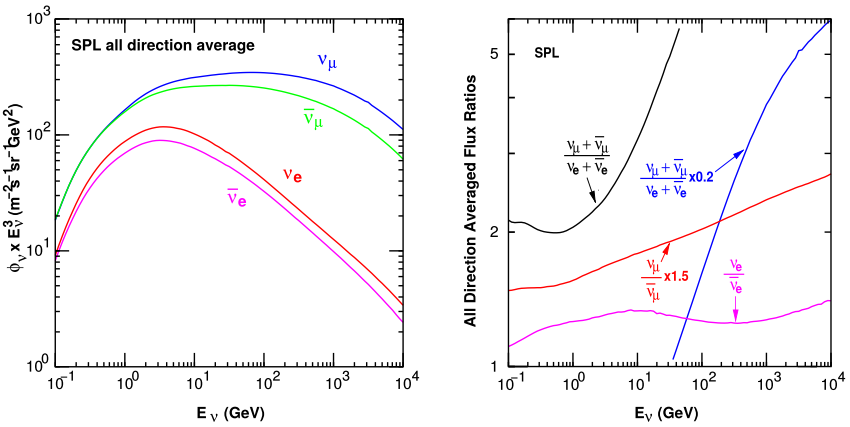

Figure 2.5: The atmospheric fluxes of different neutrino flavors as a function of energy (left) and the ratios between muon neutrinos and electron neutrinos as well as the ratios between neutrinos and antineutrinos for both those flavors (right). Results from the calculations performed for the geographic South Pole, taken from [75].

2.3 Atmospheric Neutrinos as Source of Heavy Neutral Leptons

This work focuses on the search for HNLs using atmospheric neutrinos as source for the production and decay inside the IceCube detector. The following sections will give a brief overview of the production of neutrinos in the atmosphere and the oscillations they undergo, before discussing the expected signatures of HNLs in the detector, where they are produced from the incoming neutrinos and subsequently decay.

2.3.1 Production of Neutrinos in the Atmosphere

The analysis performed in this work is based on the sample of neutrinos observed in IceCube DeepCore at energies below 100 GeV. At these energies, the flux exclusively originates in the Earth's atmosphere. Highly relativistic cosmic rays (protons and heavier nuclei [74]) interact in the upper atmosphere, producing showers of secondary particles. Neutrinos are produced in decays of charged pions and kaons (π and K mesons) present in those showers, where the dominant contribution comes from the decay chain

[74]: Tanabashi et al. (2018), "Review of Particle Physics"

$$\begin{aligned} \pi^\pm &\longrightarrow \mu^\pm + \nu_\mu(\bar{\nu}_\mu) \,, \\ \mu^\pm &\longrightarrow e^\pm + \bar{\nu}_\mu(\nu_\mu) + \nu_e(\bar{\nu}_e) \,, \end{aligned} \tag{2.22}$$

where muon neutrinos ν_μ and muons $\mu^\pm$ are produced in the first decay and both electron and muon neutrinos $\nu_{e/\mu}$ are produced in the second decay. Atmospheric muons, which are also produced in these decays, are the main background component for IceCube DeepCore analyses.

The different atmospheric flux components are shown in Figure 2.5 (left), for a much broader energy range than relevant for this work. Both neutrinos and antineutrino fluxes are shown for electron and muon neutrinos and all fluxes are the directionally averaged expectation calculated at the South Pole. Muon neutrinos are dominating the flux and from Equation 2.22 the naive assumption would be that the ratio between muon and electron neutrinos is $(\nu_\mu + \bar{\nu}_\mu)/(\nu_e + \bar{\nu}_e) = 2$. This is roughly true at energies below 1 GeV, where all muons decay in flight, but at larger energies muons can reach the detector before decaying, which increases the ratio to approximately 10:1 at around 100 GeV. Additionally, kaon decays start to contribute which also increases the number of muons and muon neutrinos. The increasing ratio can be seen

in Figure 2.5 (right), which also shows the ration between neutrinos and antineutrinos for both flavors.

Charged mesons or tau particles can also be produced in cosmic ray interactions. Their decays lead to the production of tau neutrinos. At the energies relevant for this work however, the resulting tau neutrino flux is negligible as compared to the muon neutrino flux [76] and is not considered in the analysis. This is because both charged mesons and tau particles are much heavier than pions and kaons and therefore their production is suppressed at high energies.

[76]: Fedynitch et al. (2015), "Calculation of conventional and prompt lepton fluxes at very high energy"

Say something about atmospheric neutrino flux uncertainties, based on recent JP/Anatoli papers. (YELLOW)

2.3.2 Neutrino Oscillations

Describing neutrinos in their mass state as introduced in Section **??** is crucial to understand their propagation through space and time and to explain neutrino oscillations. Oscillations mean that a neutrino changes from its initial flavor, that it was produced with, to another flavor and back after traveling a certain distance.

The neutrino propagation in vacuum can be expressed by applying a plane wave approach, where the mass eigenstates evolve as

$$|\nu_k(t)\rangle = e^{-iE_k t/\hbar} |\nu_k\rangle \ . \tag{2.23}$$

The energy of the mass eigenstate $|\nu_k\rangle$ is $E_k = \sqrt{\vec{p}^2c^2 + m_k^2c^4}$, with momentum $\vec{p}$ and mass m_k, $\hbar$ is the reduced Planck constant, and c is the speed of light in vacuum. A neutrino is produced as a flavor eigenstate $|\nu_\alpha\rangle$ in a CC weak interaction, but its propagation happens as the individual mass states it is composed of. The probability of finding the neutrino with initial flavor $|\nu_\alpha\rangle$ in the flavor state $\left|\nu_\beta\right\rangle$ after the time t is calculated as

$$P_{\nu_\alpha \to \nu_\beta}(t) = |\left\langle \nu_\beta | \nu_\alpha(t) \right| \left. \nu_\beta | \nu_\alpha(t) \right\rangle|^2 \ , \tag{2.24}$$

[77]: Dirac (1927), "The Quantum Theory of the Emission and Absorption of Radiation"

by applying Fermi's Golden Rule [77], which defines the transition rate from one eigenstate to another by the strength of the coupling between them. This coupling strength is the square of the matrix element and using the fact that the mixing matrix is unitary ($U^{-1} = U^\dagger$) to describe the mass eigenstates as flavor eigenstates, we find the time evolution of the flavor state $|\nu_\alpha(t)\rangle$, which can be inserted into Equation 2.24 to find the probability as

$$P_{\nu_\alpha \to \nu_\beta}(t) = \sum_{j,k} U^*_{\beta j} U_{\alpha j} U_{\beta k} U^*_{\alpha k} e^{-i(E_k - E_j)t/\hbar} \ . \tag{2.25}$$

The indices j and k run over the mass eigenstates.

We can approximate the energy as

$$E_k \approx E + \frac{c^4 m_k^2}{2E} \quad \longrightarrow \quad E_k - E_j \approx \frac{c^4 \Delta m_{kj}^2}{2E} \ , \tag{2.26}$$

for small neutrino masses compared to their kinetic energy. Here, $\Delta m_{kj}^2 = m_k^2 - m_j^2$ is the mass-squared splitting between states k and j. Replacing the time in Equation 2.25 by the distance traveled by relativistic neutrinos

$t \approx L/c$ we get

$$P_{\nu_\alpha \to \nu_\beta}(t) = \delta_{\alpha\beta} - 4 \sum_{j>k} \mathbf{Re}(U^*_{\beta j} U_{\alpha j} U_{\beta k} U^*_{\alpha k}) \sin^2\left(\frac{c^3 \Delta m^2_{kj}}{4E\hbar} L\right) + 2 \sum_{j>k} \mathbf{Im}(U^*_{\beta j} U_{\alpha j} U_{\beta k} U^*_{\alpha k}) \sin^2\left(\frac{c^3 \Delta m^2_{kj}}{4E\hbar} L\right), \tag{2.27}$$

which is called the survival probability if $\alpha = \beta$, and the transition probability if $\alpha \neq \beta$. Once again, this probability is only non-zero if there are neutrino mass eigenstates with masses greater than zero. Additionally, there must be a mass-squared difference Δm^2 and non-zero mixing between the states. Since we assumed propagation in vacuum in Equation 2.23, the transition and survival probabilities correspond to vacuum mixing.

The mixing matrix can be parameterized as [74]

$$U = \begin{pmatrix} 1 & 0 & 0 \\ 0 & c_{23} & s_{23} \\ 0 & -s_{23} & c_{23} \end{pmatrix} \begin{pmatrix} c_{13} & 0 & s_{13} e^{-i\delta_{CP}} \\ 0 & 1 & 0 \\ -s_{13} e^{i\delta_{CP}} & 0 & c_{13} \end{pmatrix} \begin{pmatrix} c_{12} & s_{12} & 0 \\ -s_{12} & c_{12} & 0 \\ 0 & 0 & 1 \end{pmatrix}, \tag{2.28}$$

where $c_{ij} = \cos\theta_{ij}$ and $s_{ij} = \sin\theta_{ij}$ are cosine and sine of the mixing angle θ_{ij}, that defines the strength of the mixing between the mass eigenstates i and j, and δ_{CP} is the neutrino CP-violating phase. Experiments are sensitive to different mixing parameters, depending on the observed energy range, neutrino flavor, and the distance between the source and the detector L, commonly referred to as *baseline*. To be able to resolve oscillations the argument

$$\frac{\Delta m^2 L}{4E} \tag{2.29}$$

should be at the order of 1. This divides experiments into ones that are sensitive to very slow oscillations from $\Delta m^2_{21} \approx \mathcal{O}(10^{-5}\text{eV}^2)$ and ones that are sensitive to faster oscillations from $\Delta m^2_{31} \approx \mathcal{O}(10^{-3}\text{eV}^2)$. Relevant for this work are the parameters that can be measured at the earths surface using atmospheric neutrinos, which are Δm^2_{31}, θ_{23}, and θ_{13}, because the flux is primarily composed of muon neutrinos and antineutrinos. Applying the parameterization from Equation 2.28 to Equation 2.27 and using the fact that θ_{13} is small and θ_{12} is close to $\pi/4$, the survival probability of muon neutrinos can be approximated as

$$\begin{aligned} P_{\nu_\mu \to \nu_\mu} &\simeq 1 - 4|U_{\mu 3}|^2(1 - |U_{\mu 3}|^2) \sin^2\left(\frac{\Delta m^2_{31} L}{4E}\right) \\ &\simeq 1 - \sin^2\left(2\theta_{23}\right) \sin^2\left(\frac{\Delta m^2_{31} L}{4E}\right), \end{aligned} \tag{2.30}$$

while the tau neutrino appearance probability is

$$\begin{aligned} P_{\nu_\mu \to \nu_\tau} &\simeq 4|U_{\mu 3}|^2 |U_{\tau 3}|^2 \sin^2\left(\frac{\Delta m^2_{31} L}{4E}\right) \\ &\simeq \sin^2\left(2\theta_{23}\right) \sin^2\left(\frac{\Delta m^2_{31} L}{4E}\right). \end{aligned} \tag{2.31}$$

The latest global fit [78] of all the parameters is shown in Table 2.2.

[74]: Tanabashi et al. (2018), "Review of Particle Physics"

Parameter	Global Fit
θ_{12} [°]	$33.41^{+0.75}_{-0.72}$
θ_{13} [°]	$8.54^{+0.11}_{-0.12}$
θ_{23} [°]	$49.1^{+1.0}_{-1.3}$
Δm^2_{21} [10^{-5}eV^2]	$7.41^{+0.21}_{-0.20}$
Δm^2_{31} [10^{-3}eV^2]	$2.511^{+0.028}_{-0.027}$
δ_{CP} [°]	197^{+42}_{-25}

Table 2.2: Results from the latest global fit of neutrino mixing parameters from [78].

[78]: Esteban et al. (2020), "The fate of hints: updated global analysis of three-flavor neutrino oscillations"

say something about matter effect? (ORANGE)

say something about mass ordering? (ORANGE)

2.3.3 Neutrino Interactions with Nuclei

The neutrino detection principle of IceCube DeepCore is explained in Chapter 3 and relies on the weak interaction processes between neutrinos and the nuclei of the Antarctic glacial ice. At neutrino energies above 5 GeV, the cross-sections are dominated by ***deep inelastic scattering (DIS)***, where the neutrino is energetic enough to resolve the underlying structure of the nucleons and interact with one of the composing quarks individually. As a result the nucleon breaks and a shower of hadronic secondary particles is produced. Depending on the type of interaction, the neutrino either remains in the final state for NC interactions or is converted into its charged lepton counterpart for CC interactions. The CC DIS interactions have the form

$$\begin{aligned} \nu_l + N &\rightarrow l^- + X \,, \\ \bar{\nu}_l + N &\rightarrow l^+ + X \,, \end{aligned} \tag{2.32}$$

where $\nu_l / \bar{\nu}_l$ and l^- / l^+ are the neutrino/antineutrino and its corresponding lepton/antilepton, and l can be either an electron, muon, or tau. N is the nucleon and X stands for any set of final state hadrons. The NC DIS interactions are

$$\begin{aligned} \nu_l + N &\rightarrow \nu_l + X \text{ and} \\ \bar{\nu}_l + N &\rightarrow \bar{\nu}_l + X \,. \end{aligned} \tag{2.33}$$

Figure 2.6 shows the Feynman diagrams for both processes DIS interactions

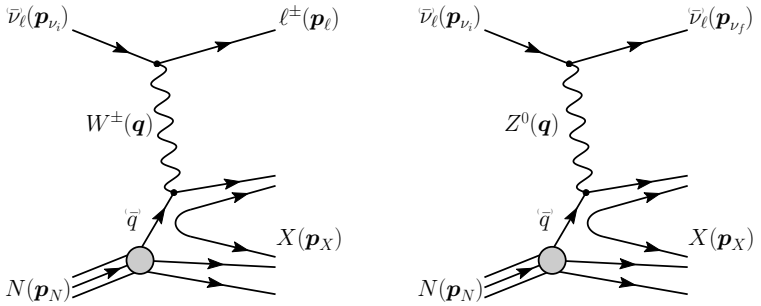

Figure 2.6: Feynman diagrams for deep inelastic scattering of a neutrino with a nucleon via charged-current (left) and neutral current (right) interactions. $\boldsymbol{p}_{\nu_i}$, $\boldsymbol{p}_N$ and $\boldsymbol{p}_{\nu_f}$, $\boldsymbol{p}_l$, $\boldsymbol{p}_N$ are the input and output four-momenta, while $\boldsymbol{q}$ is the momentum transfer. Taken from [79].

have a roughly linear energy dependent cross-section above ~20 GeV and are well measured and easy to theoretically calculate. They are the primary interaction channel for neutrinos detected with IceCube.

At energies below 5 GeV, ***quasi-elastic scattering (QE)*** and ***resonant scattering (RES)*** become important. At these energies the neutrinos interact with the approximately point-like nucleons, without breaking them up in the process. RES describes the process of a neutrino scattering off a nucleon producing an excited state of the nucleon in addition to a charged lepton. It is the dominant process at 1.5 GeV to 5 GeV for neutrinos and 1.5 GeV to 8 GeV for antineutrinos. Below 1.5 GeV QE is the main process, where protons are converted to neutrons in antineutrino interactions and vice-versa for neutrino interactions. Additionally, a charged lepton corresponding to the neutrino/antineutrino flavor is produced. The cross-sections of QE and RES scattering processes are not linear in energy and the transition region from QE/RES to DIS is poorly understood. The total cross-sections and their composition is shown in Figure 2.7. It can be seen that the interaction cross-sections are very small at the order of 10^{-38} cm^2. This is the reason why very

large volume detectors are required to measure atmospheric neutrinos with sufficient statistics to perform precision measurements of their properties. The interaction length of a neutrino with $E_\nu = 10\,\text{GeV}$ is of $\mathcal{O}(10 \times 10^{10}\,\text{km})$, for example.

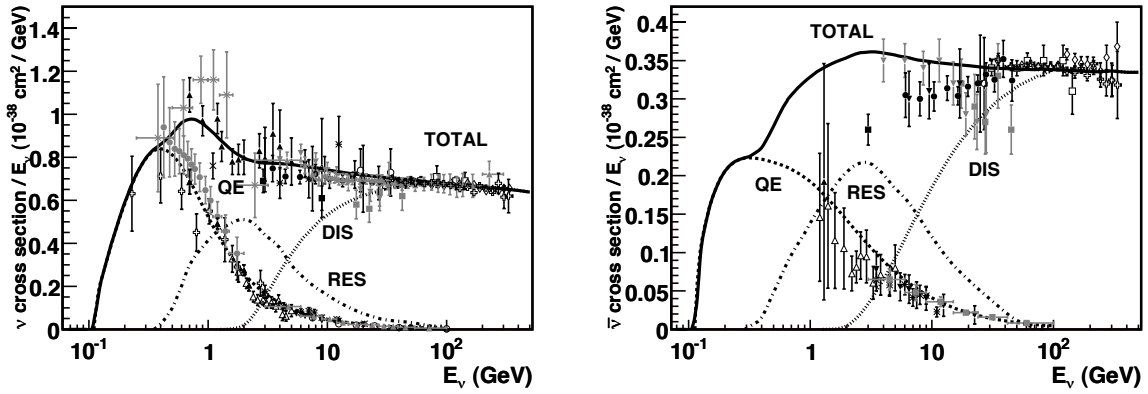

Figure 2.7: Total neutrino (left) and antineutrino (right) per nucleon cross-section divided by neutrino energy plotted against energy. The three main scattering processes quasi-elastic scattering (QE), resonant scattering (RES), and deep-inelastic scattering (DIS) are shown. Taken from [80].

2.3.4 Heavy Neutral Lepton Production and Decay

For the search conducted in this work, both production and decay are assumed to happen inside the detector, therefore probing decay lengths ranges at the scale of the detector size, which is below 1000 m. Since the mixing with the first two generations of leptons is already strongly constrained as was discussed in Section 2.3, only the mixing with the tau neutrino will be considered in the following. Due to the effect of oscillations, described in Section 2.3.2, the initial atmospheric muon neutrino flux provides a sizable tau neutrino flux at the detector.

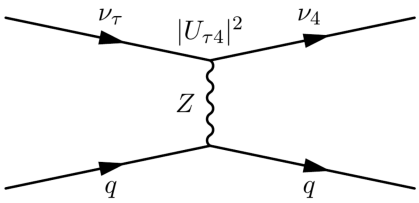

Figure 2.8: Feynman diagram of the HNL production. The heavy mass state is produced in the up-scattering of a tau neutrino.

For a non-zero $|U_{\tau 4}|^2$, the HNL can be produced through **up-scattering in the ice**. An incoming tau neutrinos scatters on an ice nucleus and transfers some of its kinetic energy to the heavy neutrino. The Feynman diagram of this process is shown in Figure 2.8. The custom NC cross-sections calculated for this purpose are explained in more detail in Section 4.2.1, but are similar to the SM tau neutrino NC cross-sections, with a reduction scaling with the mixing $|U_{\tau 4}|^2$ and energy dependent reductions, due to kinematic constraints because of the heavy neutrino mass. The scattering process produces a hadronic cascade, which will produce light in the detector.

After a certain distance, the HNL will **decay in the ice**, where the possible decay channels considered in this work are shown in Figure 2.9 and the underlying, explicit calculations are discussed in Section 4.2.1. The decay can be a CC or NC and both purely leptonic and leptonic+mesonic modes

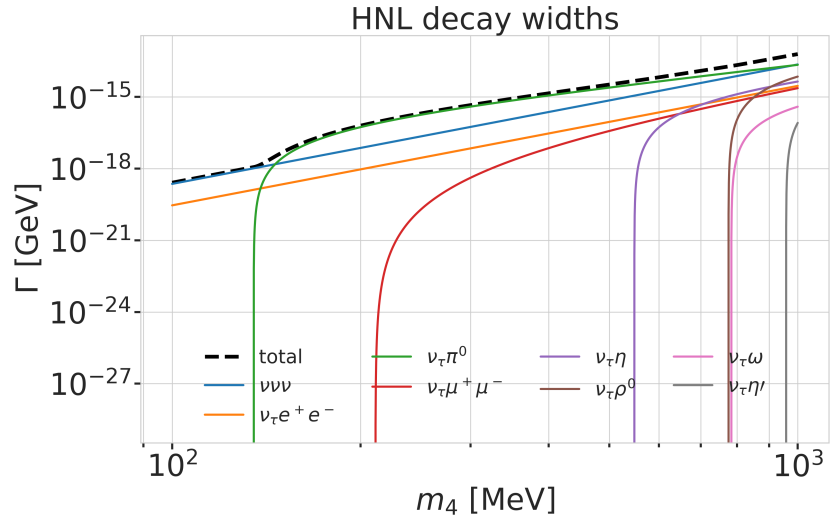

Figure 2.9: Decay widths of the HNL within the mass range considered, calculated based on the results from [73]. Given the existing constraints on $|U_{e4}|^2$ and $|U_{\mu 4}|^2$, we consider that the corresponding decay modes are negligible.

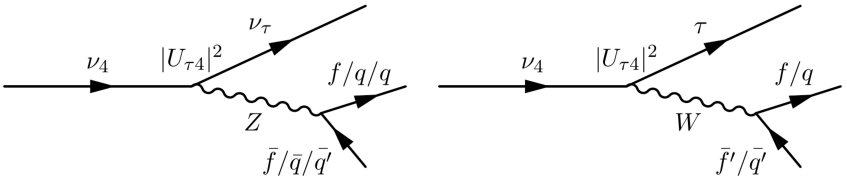

Figure 2.10: Feynman diagram of the HNL decay. The heavy mass state can decay through neutral current interaction (left) into a tau neutrino and a charged lepton or quark pair, or through charged current interaction (right) into a tau lepton and a charged lepton or quark.

are possible. The Feynman diagrams of the decays can be seen in Section **??**. Only the mass range relevant for this work is presented and mixing with $\nu_{e/\mu}$ is assumed to be negligible. Depending on the decay channel, an electromagnetic or a hadronic cascade is produced, while some energy is carried away by the invisible neutrino. The decay length of the HNL is defined by its proper lifetime[1], which is given by

$$\tau_{\text{proper}} = \frac{\hbar}{\Gamma_{\text{total}}(m_4) \cdot |U_{\tau 4}|^2} \,, \tag{2.34}$$

where $\hbar$ is the reduced Planck constant, $\Gamma_{\text{total}}(m_4)$ is the total decay width of the HNL for the given mass, and $|U_{\tau 4}|^2$ is the mixing with the tau neutrino. The total decay width is the sum of the partial decay widths for all possible decay channels. The mean lab frame decay length is then given by

$$L_{\text{decay}} = \gamma v \tau_{\text{proper}} \,, \tag{2.35}$$

where γ is the Lorentz factor of the HNL, defined by the kinetic energy. This will be further discussed on Section 4.2.1. Figure 2.11 shows the mean decay lengths for an example mass of $m_4 = 0.6\,\text{GeV}$ and several mixing values.

1: A particle decay time follows an exponential distribution, with mean lifetime given by the proper lifetime. The proper lifetime is the lifetime in the rest frame of the particle.

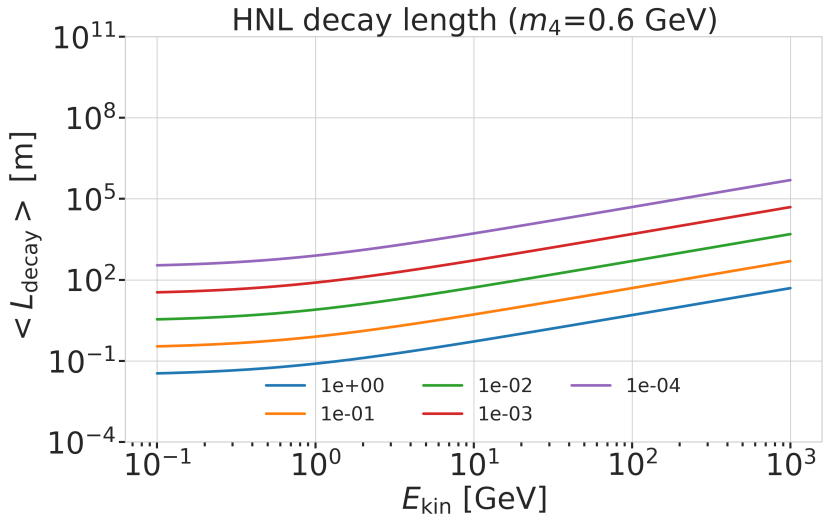

Figure 2.11: Theoretical mean decay length of the HNL for a mass of 0.6 GeV and different mixing values.

The IceCube Neutrino Observatory

3

The IceCube Neutrino Observatory [6] is a cubic-kilometer, ice-Cherenkov detector located at the geographic South Pole. IceCube utilizes the Antarctic glacial ice as detector medium to observe neutrinos by measuring the Cherenkov light produced from secondary charged particles. It was deployed between 2006 and 2011 and has been taking data since the installation of the first modules. The primary goal of IceCube is the observation of astrophysical neutrinos as a telescope, but it can also be used to study fundamental particle physics properties using the same astrophysical neutrinos, and by measuring atmospheric neutrinos as well as studying cosmic rays.

This chapter first describes the detector and its subcomponents in Section 3.1, the propagation of particles through ice is explained in Section 3.2, and finally, the signatures that IceCube can observe of the different particles are introduced in Section 3.3.

[6]: Aartsen et al. (2017), "The IceCube Neutrino Observatory: instrumentation and online systems"

3.1 Detector Components

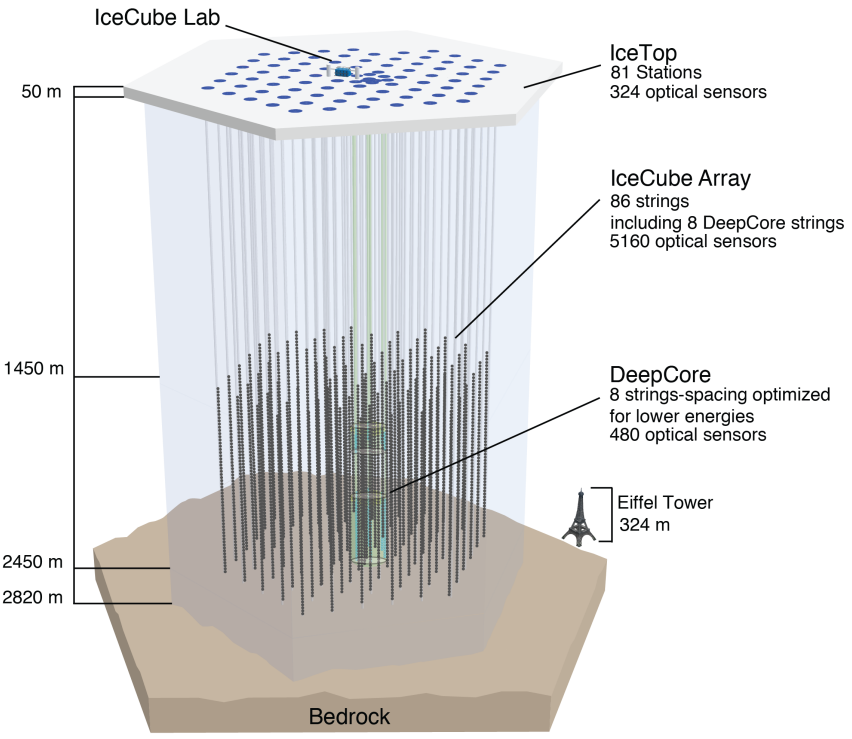

Figure 3.1: Overview of the IceCube detector showing the in-ice main- and sub-array IceCube and DeepCore, IceTop, and the IceCube Laboratory. From [6].

The full IceCube detector array consists of 86 vertical, in-ice strings and 81 surface stations as shown in Figure 3.1. The in-ice part is composed of 60 optical modules per string deployed at depths of 1450 m - 2450 m below the ice, while the surface stations of the cosmic air-shower array, *IceTop*, are ice-filled tanks. The surface stations and the majority of the strings are arranged in a hexagonal grid with the operations building, the *IceCube Laboratory* (ICL), central to the grid on the surface. A top view of the hexagonal arrangement

is shown in Figure 3.4. The in-ice array is designed to detect neutrinos in the energy range from GeV to PeV.

3.1.1 Digital Optical Modules and the Antarctic Ice

The IceCube detection medium is the Antarctic glacial ice itself, which was formed over 100 000 years by accumulation of snow that was subsequently compressed by its own weight to form a dense crystal structure [81]. As a result of this formation process, the optical properties, scattering and absorption, primarily change with depth. Within the detector volume the absorption length ranges from 100 m - 400 m, while the scattering length lies between 20 m and 100 m. They are correlated, with the absorption length being roughly four times the scattering length [82]. The vertical distribution of the absorption length can be seen in Figure 3.2, where one dominant feature is the *dust layer* between 2000 m and 2100 m depth. This region has a higher concentration of dust particles that were deposited in a period of high volcanic activity, which leads to bad optical properties in form of larger scattering and absorption.

[81]: Price et al. (2000), "Age vs depth of glacial ice at South Pole"

SB: there are more properties than just these. Somehow need a half sentence that explains why these are particularly important to single out (see ice papers for inspiration) (RED)

CL: maybe define what absorption and scattering lengths are? they are defined differently so this invites a comparison that is not so obvious (RED)

[82]: Abbasi et al. (2022), "In-situ estimation of ice crystal properties at the South Pole using LED calibration data from the IceCube Neutrino Observatory"

Add reference for the dust layer! Maybe also from the ice paper? mention/cite dust logger paper/procedure? (RED)

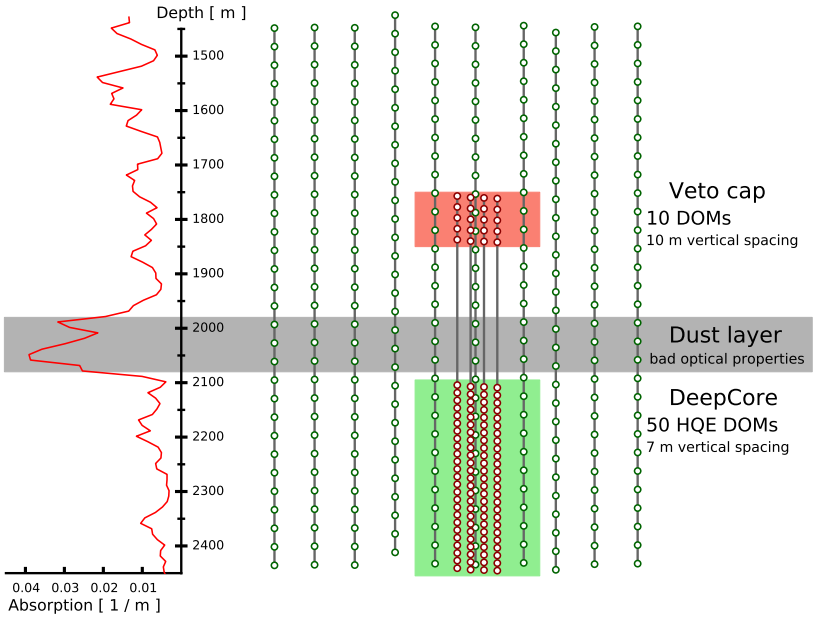

Figure 3.2: Side view of IceCube and DeepCore showing the depth dependent scattering and absorption length (left panel) and the DOM positions around the dust layer.

The ice is instrumented by 5160 optical sensors called *digital optical modules* (DOMs) [83], which can detect the Cherenkov light produced by charged particles traveling through the ice. Each DOM is made of a spherical glass housing, containing a downward-facing *photomultiplier tube (PMT)*, the mainboard with control, readout, and processing-electronics, and a LED flasherboard for calibration purposes. The design and the individual components of a DOM can be seen in Figure 3.3.

[83]: Abbasi et al. (2009), "The IceCube data acquisition system: Signal capture, digitization, and timestamping"

The majority of PMTs are the 10 " Hamamatsu R7081-02, which have a bialkali photocathode and are sensitive to wavelengths in the range of 300 nm to 650 nm, with a peak quantum efficiency of 25 % at 390 nm. The average dark count rate during operation in the ice is ~300 Hz. The DOM electronics measure the PMT voltage and control the gain. At a voltage crossing of the equivalent to 0.25 PE the waveform readout is activated [83]. Only when either one of the nearest or next to nearest DOMs above or below also sees a

[83]: Abbasi et al. (2009), "The IceCube data acquisition system: Signal capture, digitization, and timestamping"

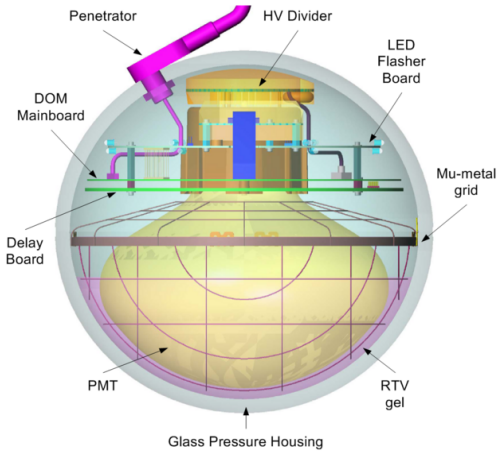

Figure 3.3: Design and components of a digital optical module (DOM) [83]

voltage crossing within a 1 µs time window [1], the voltages are digitized and sent to the ICL. Through the application of a waveform unfolding algorithm, called *WaveDeform* [84], the waveforms are compressed, and the results are the reconstructed times and charges of the photo-electrons. This is the basis for all further IceCube data processing.

1: This is referred to as a *hard local coincidence (HLC)* [83].

[84]: Aartsen et al. (2014), "Energy Reconstruction Methods in the IceCube Neutrino Telescope"

The PMT is covered with a mu-metal grid (made from wire mesh), shielding the photocathode from Earth's magnetic field, and it is optically coupled to the glass sphere by RTV silicone gel. The glass sphere is a pressure vessel, designed to withstand both the constant ice pressure and the temporary pressure during the refreezing process of the water in the drill hole during deployment (peaking at around 690 bar). The sphere is held by a harness that connects the DOMs along a string and also guides the cable for power supply and communication beside them.

The flasher-board controls 12 LEDs that produce optical pulses with a wavelength of 405 nm [6]. The LEDs can be pulsed separately or in combination with variable output levels and pulse lengths. Using the known information of the light source positions and times this can be used for in-situ calibration of the detector by measuring absorption and scattering properties of the ice. Calibrating the absolute efficiency of the DOMs itself is more accurately done using minimum ionizing muons [85, 86], since the total amplitude of the LED light is not well known.

[6]: Aartsen et al. (2017), "The IceCube Neutrino Observatory: instrumentation and online systems"

[85]: Feintzeig (2014), "Searches for Point-like Sources of Astrophysical Neutrinos with the IceCube Neutrino Observatory"
[86]: Kulacz (2019), "In Situ Measurement of the IceCube DOM Efficiency Factor Using Atmospheric Minimum Ionizing Muons"

3.1.2 IceCube Main-Array

The 78 strings that are arranged in a hexagonal pattern from the main part of the in-ice array, which is called *IceCube*. With a ~125 m horizontal spacing between the strings and a ~17 m vertical spacing between DOMs, IceCube has a lower energy threshold of around 100 GeV. IceCube was designed to detect high energy neutrinos of astrophysical origin.

The coordinate system that is used in IceCube is centered at 46500'E, 52200'N at an elevation of 883.9 m [6]. Per definition, it is a right-handed coordinate system where the y-axis points along the Prime Meridian (Grid North) towards Greenwich, UK, and the x-axis points 90° clockwise from the y-axis (Grid East). The z-axis is normal to the ice surface, pointing upwards. For IceCube analyses depth is defined as the distance along the z axis from the ice surface, fixed at an elevation of 2832 m.

[6]: Aartsen et al. (2017), "The IceCube Neutrino Observatory: instrumentation and online systems"

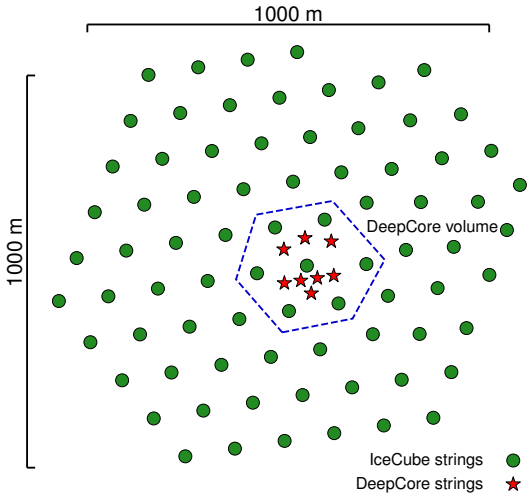

Figure 3.4: Top view of the IceCube array.

3.1.3 DeepCore Sub-Array

The additional 8 strings form a denser sub-array of IceCube called *DeepCore* [87]. It is located at the bottom-center of the in-ice array and its *fiducial volume* also includes the 7 surrounding IceCube strings as shown in Figure 3.4. The strings in this region have a closer average horizontal distance of about 70 m. The lower 50 DeepCore DOMs on each string are placed in the region of clear ice below the dust layer between 2100 m to 2450 m depth, where their vertical spacing is ~7 m. The remaining 10 modules on each string are placed above the dust layer to be used as veto against atmospheric muons as can be seen in Figure 3.2. Additionally, the DeepCore DOMs are equipped with higher quantum efficiency PMTs[2]. The combination of the denser spacing, the high quantum efficiency modules, and the most favorable ice properties below the dust layer leads to a lower energy detection threshold of around 5 GeV, allowing the more efficient observation of atmospheric neutrinos. This lower energy threshold enables measurements of neutrino oscillations and many other BSM studies such as dark matter, non-standard interactions, and sterile neutrinos [87].

[87]: Abbasi et al. (2012), "The design and performance of IceCube DeepCore"

2: At 400 nm they are 35 % more efficient than the IceCube PMTs [87].

[87]: Abbasi et al. (2012), "The design and performance of IceCube DeepCore"

3.2 Particle Propagation in Ice

Neutrinos interacting in the ice via DIS produce muons, electromagnetic showers, and hadronic showers, depending on their flavor and the interaction type. The particles produced in those processes mainly lose their energy through *ionization*, *bremsstrahlung*, *pair production*, and the *photo-nuclear interaction*. Electrically charged particles also emit Cherenkov light when traveling through the ice, which is the main observable in IceCube, but only contributes a small amount to the total energy loss. The Cherenkov effect and the energy losses of the particles are described in the following sections, followed by an overview of the different particle signatures in IceCube.

3.2.1 Cherenkov Effect

The detection principle of IceCube DeepCore is based on the observation of Cherenkov photons that are emitted by the charged secondary particles

produced in the neutrino interactions that were introduced in Section 2.3.3. The Cherenkov effect was first observed by Pavel Cherenkov in 1934 [88] and occurs when the charged particle travels faster than the phase velocity of light, therefore polarizing the medium. Upon de-excitation the molecules emit the received energy as photons in a spherical wavefront. Since the particle moves past this wavefront, the superposition of the spherical light emissions forms a cone, which is shown in blue in the bottom panel of Figure 3.5.

[88]: Cherenkov (1937), "Visible Radiation Produced by Electrons Moving in a Medium with Velocities Exceeding that of Light"

Using trigonometry, the angle θ_c at which the Cherenkov light is emitted can be calculated as

$$\theta_c = \arccos\left(\frac{1}{\beta n}\right), \tag{3.1}$$

where $\beta = v/c_{\text{vacuum}}$ is the velocity of the particle in units of the speed of light, and n is the refractive index of the medium that defines the speed of light in the medium $c = c_{\text{vacuum}} * n$. When the particle velocity is close to the speed of light, the equation holds and the angle is only dependent on the refractive index of the medium. For the ice, the refractive index is $n \approx 1.3$ and as a result $\theta_c \approx 41°$ [89].

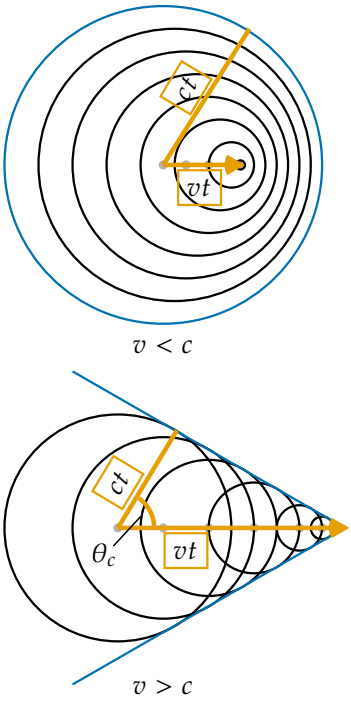

Figure 3.5: Schematic depiction of the spherical light front produced by a particle traveling slower than the speed of light in the medium (top) and the formation of the Cherenkov light front produced by a charged particle traveling faster than the speed of light in the medium (bottom). The speed of light in the medium is c, v is the speed of the particle, and t is the time that has passed. Blue is the resulting wavefront, while the black circles are spherically emitted light at each position and the orange arrows show the direction of the particle.

The frequency of the emission depends on the charge z and the wavelength-dependent index of refraction $n(\omega)$ and is given by the Frank-Tamm formula [90, 91]

$$\frac{d^2N}{dxd\lambda} = \frac{2\pi\alpha z^2}{\lambda^2}\left(1 - \frac{1}{\beta^2 n(\omega)^2}\right), \tag{3.2}$$

with $\alpha \approx 1/137$ the fine structure constant, λ the wavelength of the emitted light, and x the path length traversed by the particle. Relativistic particles in ice produce roughly 250 photons per cm in the wavelength range of 300 nm - 500 nm [92].

3.2.2 Energy Losses

Even though relativistic, charged particles traveling through matter produce Cherenkov radiation, their energy is mainly lost through other processes that are dependent on the particle type and energy. The exact principles of energy loss for the different types can broadly be categorized into the three groups: quasi-continuous energy loss by muons, electromagnetic cascades, and hadronic cascades.

Muons

Muons lose their energy by ionization, bremsstrahlung, pair production, and the photo-nuclear effect. The energy loss by ionization is the dominant process for muons above 1 GeV and has a weak energy dependence given by [21]

$$\left\langle -\frac{\mathrm{d}E}{\mathrm{d}x} \right\rangle = a_I(E) + b_R(E) \cdot E\,, \tag{3.3}$$

where E is the energy and $a_I(E)$ and $b_R(E) \cdot E$ are the energy loss by ionization and the combined radiative losses, respectively. In the energy range relevant for this work (10 GeV - 100 GeV), the parameters a_I and b_R only depend on

[89]: Petrenko et al. (2002), "214Optical and electronic properties"

[90]: Frank et al. (1937), "Coherent visible radiation from fast electrons passing through matter"

[91]: Tamm (1991), "Radiation Emitted by Uniformly Moving Electrons"

[92]: Rädel et al. (2012), "Calculation of the Cherenkov light yield from low energetic secondary particles accompanying high-energy muons in ice and water with Geant4 simulations"

[21]: Workman et al. (2022), "Review of Particle Physics"

energy very weakly and can be approximated by constants. The energy loss is then given by

$$\left\langle -\frac{\mathrm{d}E}{\mathrm{d}x} \right\rangle = a + b \cdot E \ . \tag{3.4}$$

Based on this description, there is a critical energy which divides the regimes where ionization and radiative losses dominate. The critical energy is given by $E_{\mathrm{crit}} = a/b$ and for muons in ice it is ~713 GeV (using $a \approx 2.59\,\mathrm{MeVcm}^{-1}$ and $b \approx 3.63 \times 10^{-6}\,\mathrm{cm}^{-1}$ [93]). Since the energy range of interest is well below this critical energy, the range of a muon can easily be related to its energy by

[93]: Chirkin et al. (2004), "Propagating leptons through matter with Muon Monte Carlo (MMC)"

$$\langle L \rangle = \frac{E_0}{a} \ . \tag{3.5}$$

Measuring the length of a muon track therefore allows for an estimation of its energy if the full track is contained within the instrumented volume of IceCube. Using the given numbers a 30 GeV muon travels ~116 m, which is well within the instrumented volume of IceCube, which spans across distances of up to 1000 m. This approximate treatment does not take into account the stochastic nature of some energy losses. Bremsstrahlung and photo-nuclear interactions for example rarely occur, but when they do, they deposit a large chunk of energy. A thorough investigation of the energy losses of muons in ice can be found in [94].

[94]: Raedel (2012), "Simulation Studies of the Cherenkov Light Yield from Relativistic Particles in High-Energy Neutrino Telescopes with Geant4"

Electromagnetic Showers

Photons as well as electrons and positrons are produced either directly in neutrino interactions or in secondary particle interactions. Above a critical energy E_c, they lose their energy through repeated pair production and bremsstrahlung emission forming an expanding, electromagnetic shower profile. The particles' energy reduces with every interaction and their number increases until they fall below the critical energy where ionization and excitation of surrounding atoms become the dominant energy loss processes for electrons and positrons. For photons the remaining energy is lost through the Compton effect and the photoelectric effect [21]. Below the critical energy no new shower particles are produced.

[21]: Workman et al. (2022), "Review of Particle Physics"

Electromagnetic cascades can be characterized by the radiation length, X_0, after which electrons/positrons reduced their energy to $1/e$ of their initial energy. For photons, it's equivalent to 7/9 of the mean free path of pair production. The critical energy for ice is $E_c \approx 78$ MeV, with a radiation length of $X_0 \approx 39.3$ cm [74].

[74]: Tanabashi et al. (2018), "Review of Particle Physics"

The radiation length governs the longitudinal shower profile and using $t = x/X_0$, the shower intensity can be described by a gamma distribution [21, 95]

[21]: Workman et al. (2022), "Review of Particle Physics"
[95]: Longo et al. (1975), "Monte Carlo Calculation of Photon Initiated Electromagnetic Showers in Lead Glass"

$$\frac{dE}{dt} = E_0 b \frac{(bt)^{a-1} e^{-bt}}{\Gamma(a)} \ , \tag{3.6}$$

where a and b are parameters that have to be estimated from experiment, and E_0 is the initial shower energy. Based on the work from [94], performed with GEANT4 [96], the parameters for electromagnetic showers in ice are

[94]: Raedel (2012), "Simulation Studies of the Cherenkov Light Yield from Relativistic Particles in High-Energy Neutrino Telescopes with Geant4"
[96]: Agostinelli et al. (2003), "Geant4—a simulation toolkit"

$$e^- : \ a \approx 2.01 + 1.45 \log_{10}(E_0/\mathrm{GeV}),\ b \approx 0.63 \ , \tag{3.7a}$$

$$e^+ : \ a \approx 2.00 + 1.46 \log_{10}(E_0/\mathrm{GeV}),\ b \approx 0.63 \ , \tag{3.7b}$$

$$\gamma : \ a \approx 2.84 + 1.34 \log_{10}(E_0/\mathrm{GeV}),\ b \approx 0.65 \ . \tag{3.7c}$$

The maximum of the shower is at $t_{max} = (a-1)/b$ and the Cherenkov emission of the charged particles produced in the shower is peaked around the Cherenkov angle, since they are produced in the forward direction.

Add angular profile plot (Summer agrees!) (create one based on Leif Rädel as Alex did) (RED)

Hadronic Showers

In DIS interactions, a cascade is always produced by the hadrons coming from the target nucleus that is breaking apart. The cascade is a result of secondary particles produced in strong interactions between the hadrons and the traversed matter. The charged particles produced in the shower will emit Cherenkov radiation, while neutral particles will be invisible to the detector. There is also an electromagnetic component of the shower, for example, due to the decay of neutral pions into photons. Hadronic showers of the same energy as electromagnetic showers have larger fluctuations in energy deposition and shape, since they depend on the produced particle types. Hadrons also have a higher energy threshold for Cherenkov light production, because of their higher mass. Based on [94, 97], the visible electromagnetic fraction of hadronic showers can be parameterized as

$$F(E_0) = \frac{T_{\text{hadron}}}{T_{\text{EM}}} = 1 - (1 - f_0)\left(\frac{E_0}{E_s}\right)^{-m} , \tag{3.8}$$

where $T_{\text{hadron/EM}}$ is the total track length of a hadronic/electromagnetic shower with the same energy, f_0 is the ratio of hadronic and electromagnetic light yield, E_0 is the initial energy, and E_s is an energy scale. The parameter m is a free model parameter. The ratio $F(E_0)$ increases with energy, but is always smaller than 1. The variance of this distribution is given by

$$\sigma_F(E_0) = \sigma_0 \log(E_0)^{-\gamma} . \tag{3.9}$$

The parameters m, E_s, and f_0 were estimated by fitting the model to the results of Geant4 simulations. Cherenkov light from hadronic showers also peaks around the Cherenkov angle, but the angular distribution is more smeared out, due to the variations in particle type and their energy depositions.

[94]: Raedel (2012), "Simulation Studies of the Cherenkov Light Yield from Relativistic Particles in High-Energy Neutrino Telescopes with Geant4"
[97]: Gabriel et al. (1994), "Energy dependence of hadronic activity"

3.3 Event Morphologies

The event morphologies produced by particles detected in IceCube are combinations of the three energy loss types described in Section 3.2.2, e.g. *cascades* from electromagnetic and hadronic showers and elongated *tracks* from muons traveling through the detector. Table 3.1 gives an overview of the possible event signatures.

Neutrino interactions are observed as cascades, tracks, or a combination of both, depending on the initial flavor and the interaction type for the specific event.

In ν_μ - CC interactions, a muon is produced in addition to a hadronic shower from the breaking nucleus. If the interaction happens outside the detector, but the muon passes through the detector, this will create a track-like signature. The same happens if the interaction happens inside, but the

Table 3.1: IceCube low energy event signatures, their underlying interaction type, and the particles that produce them. Also shown are the secondary particles produced in the interactions. Black dashed lines represent neutrinos, green lines muons, orange line leptons, and blue and red lines are particles in electromagnetic and hadronic cascades, respectively. Adapted from [79].

Interaction	Secondary particles	Signature
CC $\overset{(-)}{\nu}_\mu$	 $\mu^\pm$ track	Track-only
	 $\mu^\pm$ track and hadrons	Cascade + track
CC $\overset{(-)}{\nu}_\tau$	 $\tau^\pm$ decaying into $\mu^\pm$ (~17% BR), hadrons	
	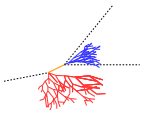 $\tau^\pm$ decaying into $e^\pm$ or hadrons (~83% BR)	
CC $\overset{(-)}{\nu}_e$	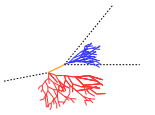 $e^\pm$, hadrons	Cascade-only
NC $\overset{(-)}{\nu}_\ell$	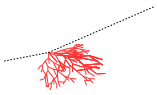 hadrons	

energy transfer to the nucleus is small ($y \approx 0$). At energies relevant for this work, tracks have length at the same order of the distance between DOMs, so they can be observed as such.

If the interaction happens inside the detector and the energy transfer to the hadronic part of the shower is larger, it will create a cascade with a track leaving it. A similar signature is observed after a ν_τ - CC interaction, in which a tau is produced that later decays into a muon, with a branching ratio of 17 %. In those cases the muon usually has a lower energy and the track will be fainter and harder to observe.

The other 83 % of ν_τ - CC interactions produce a tau that decays into an electron or hadrons, leaving a cascade-only signature through the electromagnetic or hadronic shower. All ν_e - CC interactions also produce pure cascades, since the electron quickly loses its energy in an electromagnetic shower. In all ν - NC interactions, the produced neutrino escapes and only the hadronic shower is observable. Since the size of the cascades at the energy range of interest is smaller than the spacing of the DOMs, they are approximately observed as point-like, spherical light sources. This is just an approximation, though, and some asymmetry remains in the light profile, which can be used to reconstruct the direction of the incoming neutrino.

Atmospheric muons also produce pure track like signatures, similar to ν_μ - CC interactions happening outside the detector. They are one of the main backgrounds for analyses using atmospheric neutrinos and are therefore the target of many filter steps described in Section 5.2.1.

Heavy Neutral Lepton Event Generation

4

The central part of this thesis is the HNL signal simulation itself. Since this is the first search for HNLs with IceCube DeepCore, there was no prior knowledge of the number of events expected per year nor of the expected performance in terms of reconstruction and classification accuracy. This chapter describes the first HNL event generation developed for IceCube DeepCore. Two avenues of generation were pursued in parallel. A collection of model-independent simulation samples is explained in Section 4.1. They were used for performance benchmarking and for cross-checks to validate the physically accurate, model-dependent simulation, which is described in Section 4.2. For completeness, the event generation for SM background events is briefly described in Section 4.3. The default low-energy event selection and processing chain, which is applied identically to both background and signal, is introduced in Chapter 5.

JVS: I would describe simulation sets you produced in past rather than present tense (ORANGE)

4.1 Model-Independent Simulation

To investigate the potential of IceCube to detect HNLs by identifying the unique double cascade morphology explained in Section 2.3.4, a model-independent double cascade generator was developed, where the kinematics of each cascade can be controlled directly. Using this generator, several simulation samples were produced to investigate the performance of IceCube DeepCore to detect low-energy double cascades, dependent on their properties. All samples are produced using a collection of custom generator functions [98] that place two EM cascade vertices with variable energy and direction at configurable locations in the detector.

4.1.1 Simplistic Samples

add/move event views to here? or draw a schematic of these events? (ORANGE)

To investigate the best-case and the worst-case double cascade event scenarios, two samples are produced in the DeepCore volume: straight up-going events ($\cos(\theta) = -1$) that are centered on a string and horizontal events ($\cos(\theta) = 0$).

Sample	Variable	Distribution	Range/Value
Up-going			
	energy	uniform	0.0 GeV to 60.0 GeV
	zenith	fixed	180.0°
	azimuth	fixed	0.0°
	x, y position	fixed	(41.6, 35.49) m
	z position	uniform	−480.0 m to −180.0 m
Horizontal			
	energy	uniform	0.0 GeV to 60.0 GeV
	zenith	fixed	90.0°
	azimuth	uniform	0.0° to 360.0°
	x, y position	uniform (circle)	c=(46.29, -34.88) m, r=150.0 m
	z position	fixed	−330.0 m

Table 4.1: Generation level sampling distributions and ranges/values of up-going and horizontal model-independent simulation.

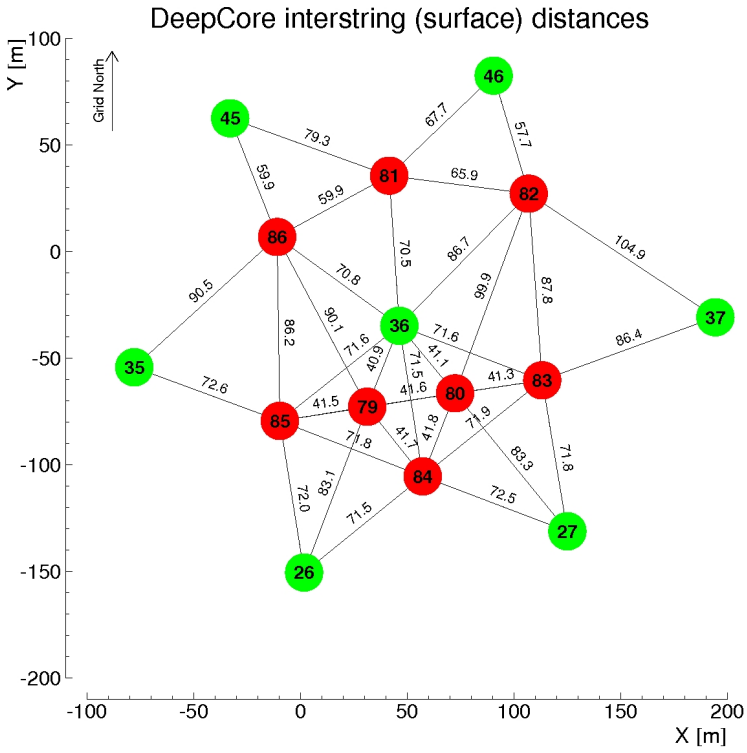

Figure 4.1: Horizontal positions and distances between DeepCore strings. Red strings are instrumented more densely (vertically) and partially have higher quantum efficiency (HQE) DOMs.

The first sample is used to investigate one of the most promising scenarios to detect a double cascade, where both cascade centers are located on a DeepCore string and the directions are directly up-going. From the DeepCore strings, string 81 was randomly chosen as the x-y coordinate for this sample. The horizontal positions and distances of all DeepCore fiducial volume strings are shown in Figure 4.1 and string 81 is at a medium distance of $\sim 70\,\mathrm{m}$ to its neighboring strings. As already mentioned in Section 3.1.3, DeepCore strings have higher quantum efficiency DOMs and a denser vertical spacing, making them better to detect low-energy events that produce little light. To produce the events, the x, y position of the cascades is fixed to the center of string 81 while the z positions are each sampled uniformly along the axis of the string. Note that this will therefore not produce a uniform length distribution between the cascades. The positions are defined in the IceCube coordinate system that was introduced in Section 3.1.2. The energies are sampled uniformly between 0.0 GeV and 60.0 GeV, to generously cover the region where $\nu_\mu \rightarrow \nu_\tau$ appearance is maximized. The specific sampling distributions/values for the cascades are listed in Table 4.1. The time of the lower cascade is set to $t_0 = 0.0\,\mathrm{ns}$ and for the upper one to $t_1 = L/c$, assuming the HNL travels at the speed of light, c.

The second sample is used to investigate the reconstruction performance for horizontal events, where the spacing between DOMs is much larger. The cascades are placed uniformly on a circle with radius of $r = 150\,\mathrm{m}$ centered in DeepCore at the depth of $z = -330\,\mathrm{m}$. The direction is always horizontal and azimuth is defined by the connecting vector of both cascade positions. The energies are again sampled uniformly between 0.0 GeV and 60.0 GeV and the detailed sampling distributions/values are also listed in Table 4.1. Some examples of the generation level distributions of the simplified samples are shown in Figure 4.2, while further distributions can be found in Figure A.1.

Re-make plot with all energies (cascades and total, both samples (they are the same)) (RED)

Re-make plot with all decay lengths (both samples) (RED)

Re-make energy with better y-axis limits (RED)

don't add overflow and/or mention it in the caption? (RED)

describe why these are shown to highlight some key aspect (uniformity in both energies to sample the whole space, decay length as a result of the z sampling etc..), also add this shortly to the caption (RED)

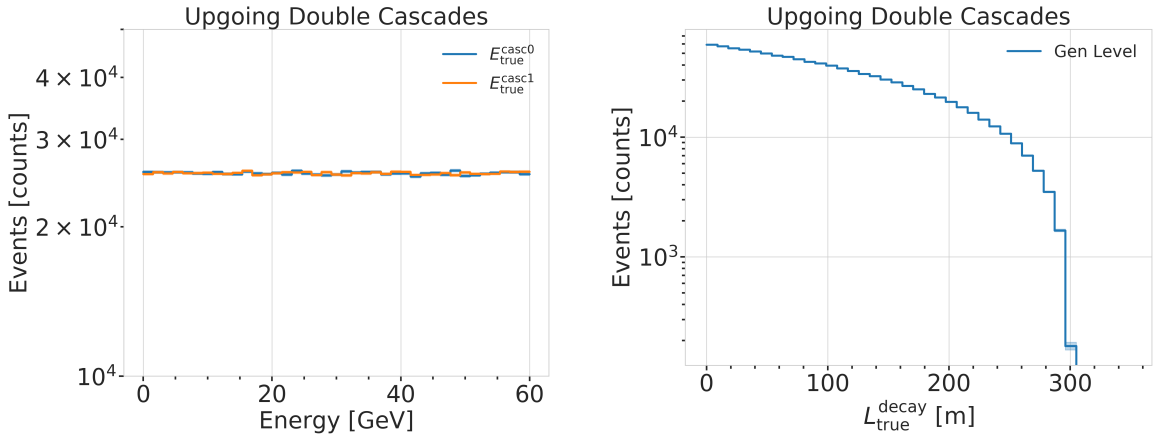

Figure 4.2: Generation level distributions of the simplistic simulation samples. Cascade and total energies (left) and decay lengths (right) of both samples are shown.

4.1.2 Realistic Sample

To thoroughly investigate the potential of IceCube DeepCore to detect double cascade events, a more realistic simulation sample is produced that aims to be as close as possible to the expected signal simulation explained in Section 4.2, while still allowing additional freedom to control the double cascade kinematics. This sample is particularly useful for validating the model-dependent HNL simulation described in Section 4.2. For this purpose the total energy is sampled from an E^{-2} power law, mimicking the energy spectrum of the primary neutrinos as stated in Section 4.3.1. The total energy is divided into two parts, by assigning a fraction between 0 % and 100 % to one cascade and the remaining part to the other cascade. This is a generic approximation of the realistic process described in Section 4.2, and chosen such that the whole sample covers various cases of energy distributions between the two cascades. To efficiently generate events in a way that produces distributions similar to what would be observed with DeepCore, one of the cascade positions is sampled inside the DeepCore volume by choosing its coordinates uniformly on a cylinder that is centered in DeepCore. This is similar to a trigger condition of one cascade always being inside the DeepCore fiducial volume. Choosing the direction of the event by sampling zenith and azimuth uniformly between 70° and 180° and 0° and 360°, respectively, the position of the other cascade can be inferred for a given decay length, assuming a travel speed of c, and choosing whether the cascade position that was sampled is the first cascade or the second with a 50 % chance. The zenith angle is chosen between straight up-going (zenith of 180°) and slightly down-going from above the horizon (70°) to mimic an event selection that reduces atmospheric muons by rejecting events coming from above the horizon, but still incorporates some down-going events. The decay length is sampled from an exponential distribution, as expected for a decaying heavy mass state. The sampling distributions/values are listed in Table 4.2. Example distributions of the generation level variables are shown in Figure 4.3, while further distributions can be found in Figure A.2.

again, describe what is shown and why this is interesting (e.g. energy distribution between the cascades, realistic exponential decay length distribtuion..) also add this to the captions shortly (RED)

Table 4.2: Generation level sampling distributions and ranges/values of the realistic model-independent simulation.

Variable	Distribution	Range/Value
energy (total)	power law E^{-2}	1 GeV to 1000 GeV
decay length	exponential $e^{-0.01L}$	0 m to 1000 m
zenith	uniform	70° to 180°
azimuth	uniform	0° to 360°
x, y (one cascade)	uniform (circle)	c=(46.29, -34.88) m, r=150 m
z (one cascade)	uniform	−480.0 m to −180.0 m

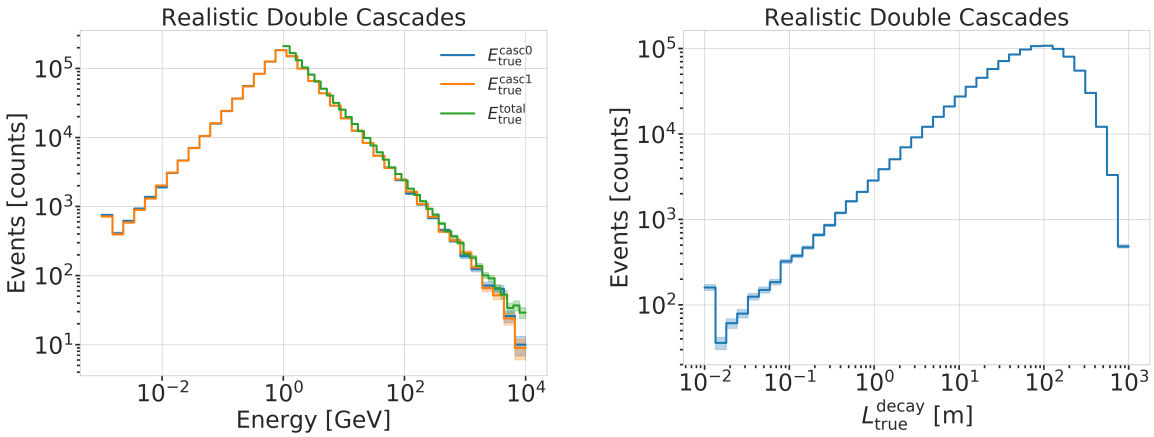

Figure 4.3: Generation level distributions of the simplistic realistic sample. Shown are the cascade and total energies (left) and decay lengths (right).

4.2 Model-Dependent Simulation

To estimate the HNL event expectation in IceCube DeepCore, depending on the specific model parameters, a generator was developed that is based on the HNL theory introduced in Section 2.3. For this work, only the interaction with the τ-sector was taken into account ($|U^2_{\alpha 4}| = 0$, $\alpha = e, \mu$), which reduces the physics parameters of interest and relevent for the simulation to the fourth heavy lepton mass, m_4, and the mixing, $|U^2_{\tau 4}|$. The generator uses a customized *LeptonInjector (LI)* version to create the events and *LeptonWeighter (LW)* to weight them [99]. The modified LI and the essential components needed for the HNL simulation are described in the next sections, followed by the description of the weighting scheme and the sampling distributions chosen for the generation.

[99]: Abbasi et al. (2021), "LeptonInjector and LeptonWeighter: A neutrino event generator and weighter for neutrino observatories"

4.2.1 Custom LeptonInjector

In its standard version, the LI generator produces neutrino interactions by injecting a lepton and a hadronic cascade at the interaction vertex of the neutrino, where the lepton is the charged (neutral) particle produced in a CC (NC) interaction and the cascade is the hadronic cascade from the breaking nucleus. The hadronic cascade is stored as a specific object of type *Hadrons*, which triggers the correct simulation of the shower development in the following simulation steps, identical to what is described for neutrinos in Section 4.3.1. Below 30 GeV the individual hadrons are simulated using Geant4 [96] while for higher energies an analytical approximation from [92] is used. The main differences to an EM cascade is that part of the energy will not be observed, because it goes into neutral particles, and that the spatial

[96]: Agostinelli et al. (2003), "Geant4—a simulation toolkit"

[92]: Rädel et al. (2012), "Calculation of the Cherenkov light yield from low energetic secondary particles accompanying high-energy muons in ice and water with Geant4 simulations"

development of the shower is different as discussed in Section 3.2.2. Both objects are injected with the same (x, y, z, t) coordinates and the kinematics are sampled from the differential and total cross-sections that are one of the inputs to LI.

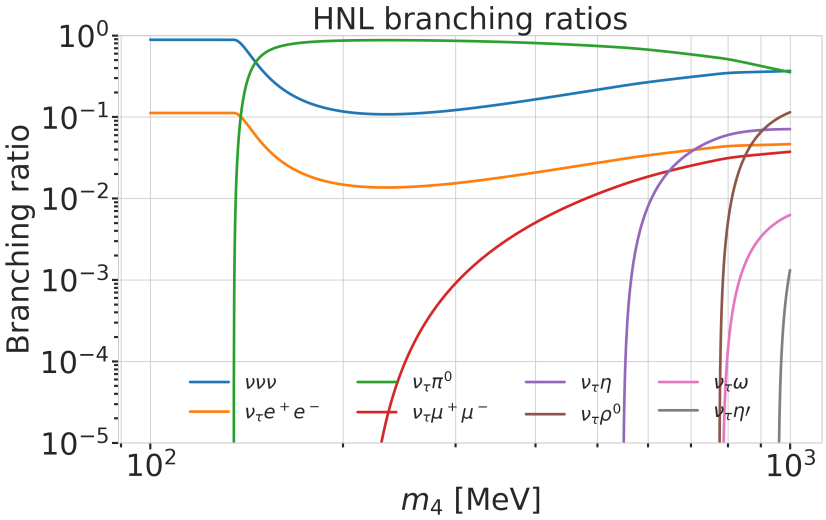

Figure 4.4: Branching ratios of the HNL within the mass range considered in this work, only considering $|U^2_{\tau 4}| \neq 0$, calculated based on the results from [73].

In the modified version, the SM lepton at the interaction vertex is replaced by the new HNL particle, where the interaction cross-sections are replaced by custom, mass dependent HNL cross-sections. The HNL is forced to decay after a chosen distance[1] to produce secondary SM particles, where the decay mode is chosen with a probability given by the mass dependent branching ratios from the kinematically accessible decay modes shown in Figure 4.4. The cross-section and decay width calculations were implemented for this purpose and will be explained in more detail in the following. Another addition to LI is that the decay products of the HNL are also stored. These HNL daughter particles form the second cascade, not as a single hadronic cascade object, but as the explicit particles forming the shower. They are injected with the correctly displaced position and delayed time from the interaction vertex, given the HNL decay length. The kinematics of the two-body decays are computed analytically, while the 3-body decay kinematics are calculated with MadGraph [100], which will also be explained further below. Independent of the number of particles in the final state of the HNL decay, the kinematics are calculated/simulated at rest and then boosted along the HNL momentum.

1: The explicit sampling distributions and ranges can be found in Section 4.2.2.

[100]: Alwall et al. (2014), "The automated computation of tree-level and next-to-leading order differential cross sections, and their matching to parton shower simulations"

The injection is done using the LI *volume mode*, for the uniform injection of the primary particle on a cylindrical volume, adding 50 % of the events with ν_τ and the other half with $\bar{\nu}_\tau$ as primary particle types. The generator takes the custom double-differential/total cross-section splines described below and the parameters defining the sampling distributions as inputs.

Cross-Sections

The cross-sections are calculated using the NuXSSplMkr [101] software, which is a tool to calculate neutrino cross-sections from *parton distribution functions (PDFs)* and then fit to an N-dimensional tensor-product B-spline surface [102] to produce the splines that can be read and used with LI/LW. The tool was modified to produce the custom HNL cross-sections, where the

[102]: Whitehorn et al. (2013), "Penalized splines for smooth representation of high-dimensional Monte Carlo datasets"

main modification to calculate the cross-sections for the ν_τ-NC interaction into the new heavy mass state, is the addition of a kinematic condition to ensure that there is sufficient energy to produce the heavy mass state. It is the same condition fulfilled for the CC case, where the outgoing charged lepton mass is non-zero. Following [103] (equation 7), the condition

[103]: Levy (2009), "Cross-section and polarization of neutrino-produced tau's made simple"

$$(1 + x\delta_N)h^2 - (x + \delta_4)h + x\delta_4 \leq 0 \tag{4.1}$$

is implemented for the NC case in the NuXSSplMkr code. Here

$$\delta_4 = \frac{m_4^2}{s - M^2}\,, \tag{4.2}$$

$$\delta_N = \frac{M^2}{s - M^2}\,, \text{and} \tag{4.3}$$

$$h \overset{def}{=} xy + \delta_4\,, \tag{4.4}$$

with x and y being the Bjorken variables, m_4 and M the mass of the heavy state and the target nucleon, respectively, and s the center of mass energy squared. The custom version was made part of the open source NuXSSplMkr software and can thus be found in [101]. The result of this kinematic condition is that events cannot be produced for energy, x, y combinations that do not have sufficient energy to produce the outgoing, massive lepton. This results in a reduction of the cross-section towards lower energies, which scales with the assumed mass of the HNL. This effect can be seen in Figure 4.5.

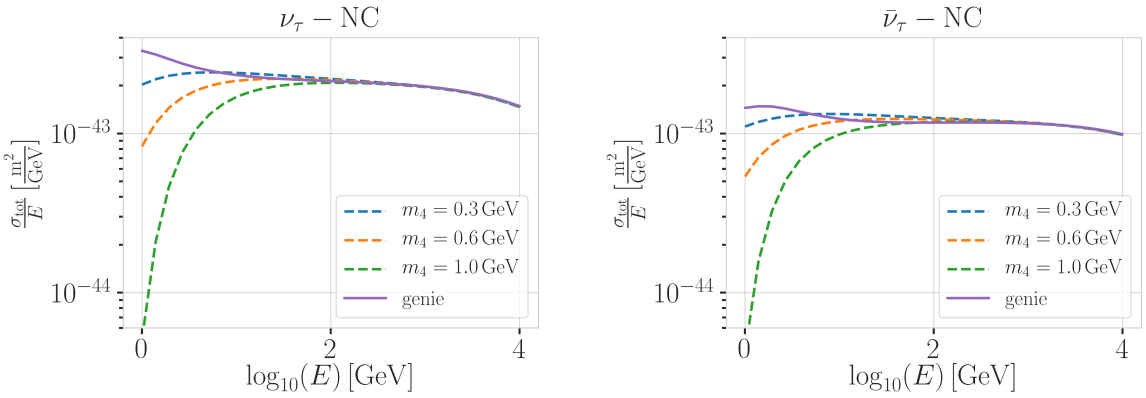

Figure 4.5: Custom HNL total cross-sections for the three target masses compared to the total ($\nu_\tau/\bar{\nu}_\tau$ NC) cross-sections used for SM neutrino simulation production with GENIE.

The GRV98LO PDFs were added to the cross-section spline maker and used to create the HNL cross-sections for consistency with the neutrino simulation explained in Section 4.3.1. The double-differential ($d^2\sigma/dxdy$) and total (σ) cross-sections were produced for the chosen target HNL masses and then splined in energy, x, and y for $d^2\sigma/dxdy$ and σ in the energy. Figure 4.5 shows the total cross-sections that were produced compared to the cross-section used for the production of the SM $\nu_\tau/\bar{\nu}_\tau$ NC background simulation. They agree above $\sim$ 200 GeV, where the modification should not have any effect on the cross-sections. This is the desired result of using the identical input PDFs, and confirms that the unmodified cross-sections produced with NuXSSplMkr agree with the GENIE cross-sections.

Decay Channels

The accessible decay channels are dependent on the mass of the HNL and the allowed mixing. For this analysis, where only $|U_{\tau 4}|^2 \neq 0$, the decay channels considered are listed in Table 4.3 and the corresponding branching ratios are shown in Figure 4.4. The individual branching ratio for a specific mass is calculated as $\mathrm{BR}_i(m_4) = \Gamma_i(m_4)/\Gamma_{\text{total}}(m_4)$, where $\Gamma_{\text{total}}(m_4) = \sum \Gamma_i(m_4)$. The individual decay widths Γ_i are computed using the state-of-the-art calculations from [73], which are described in the following.

[73]: Coloma et al. (2021), "GeV-scale neutrinos: interactions with mesons and DUNE sensitivity"

Channel	Opens
$\nu_4 \to \nu_\tau \nu_\alpha \bar{\nu_\alpha}$	0 MeV
$\nu_4 \to \nu_\tau e^+ e^-$	1 MeV
$\nu_4 \to \nu_\tau \pi^0$	135 MeV
$\nu_4 \to \nu_\tau \mu^+ \mu^-$	211 MeV
$\nu_4 \to \nu_\tau \eta$	548 MeV
$\nu_4 \to \nu_\tau \rho^0$	770 MeV
$\nu_4 \to \nu_\tau \omega$	783 MeV
$\nu_4 \to \nu_\tau \eta'$	958 MeV

Table 4.3: Possible decay channels of the HNL, considering only $|U_{\tau 4}|^2 \neq 0$, and the mass at which each channel opens.

2-Body Decay Widths The decay to a neutral pseudoscalar meson is

$$\Gamma_{\nu_4 \to \nu_\tau P} = |U_{\tau 4}|^2 \frac{G_F^2 m_4^3}{32\pi} f_P^2 (1 - x_p^2)^2 \,, \tag{4.5}$$

with $x_P = m_P/m_4$ and the *effective decay constants* f_P given by

$$f_{\pi^0} = +0.1300\,\text{GeV} \,, \tag{4.6}$$
$$f_\eta = +0.0816\,\text{GeV} \,, \text{and} \tag{4.7}$$
$$f_{\eta'} = -0.0946\,\text{GeV} \,, \tag{4.8}$$

while the decay to a neutral vector meson is given by

$$\Gamma_{\nu_4 \to \nu_\tau V} = |U_{\tau 4}|^2 \frac{G_F^2 m_4^3}{32\pi} \left(\frac{f_V}{m_V}\right)^2 g_V^2 (1 + 2x_V^2)(1 - x_V^2)^2 \,, \tag{4.9}$$

with $x_V = m_V/m_4$,

$$f_{\rho^0} = 0.171\,\text{GeV}^2 \,, \tag{4.10}$$
$$f_\omega = 0.155\,\text{GeV}^2 \,, \tag{4.11}$$

and

$$g_{\rho^0} = 1 - 2\sin^2\theta_w \,, \tag{4.12}$$
$$g_\omega = \frac{-2\sin^2\theta_w}{3} \,, \tag{4.13}$$

and $\sin^2\theta_w = 0.2229$ [104], where θ_w is the Weinberg angle.

[104]: Tiesinga et al. (2021), "CODATA recommended values of the fundamental physical constants: 2018"

3-Body Decay Widths The (invisible) decay to three neutrinos, one of flavor τ and two of any flavor α, is

$$\Gamma_{\nu_4 \to \nu_\tau \nu_\alpha \bar{\nu_\alpha}} = |U_{\tau 4}|^2 \frac{G_F^2 m_4^5}{192\pi^3} \,, \tag{4.14}$$

while the decay to two charged leptons (using $x_\alpha = (m_\alpha/m_4)^2$) of the same flavor reads

$$\Gamma_{\nu_4 \to \nu_\tau l_\alpha^+ l_\alpha^-} = |U_{\tau 4}|^2 \frac{G_F^2 m_4^5}{192\pi^3} \left[C_1 f_1(x_\alpha) + C_2 f_2(x_\alpha)\right] \,, \tag{4.15}$$

with the constants defined as

$$C_1 = \frac{1}{4}(1 - 4\sin^2\theta_w + 8\sin^4\theta_w)\,, \tag{4.16}$$

$$C_2 = \frac{1}{2}(-\sin^2\theta_w + 2\sin^4\theta_w)\,, \tag{4.17}$$

the functions as

$$f_1(x_\alpha) = (1 - 14x_\alpha - 2x_\alpha^2 - 12x_\alpha^3)\sqrt{1-4x_\alpha} + 12x_\alpha^2(x_\alpha^2 - 1)L(x_\alpha)\,, \tag{4.18}$$

$$f_2(x_\alpha) = 4[x_\alpha(2 + 10x_\alpha - 12x_\alpha^2)\sqrt{1-4x_\alpha} + 6x_\alpha^2(1 - 2x_\alpha + 2x_\alpha^2)L(x_\alpha)]\,, \tag{4.19}$$

and

$$L(x) = \ln\left(\frac{1 - 3x_\alpha - (1-x_\alpha)\sqrt{1-4x_\alpha}}{x_\alpha(1+\sqrt{1-4x_\alpha})}\right). \tag{4.20}$$

JVS: consider also writing down the (trivial) 2-body decay kinematics for completeness and consistency. This transition is a bit jarring as it is (RED)

2-Body Decay Kinematics

3-Body Decay Kinematics with MadGraph

The 3-body decay kinematics cannot be computed analytically, instead, we employ MadGraph4 (v3.4.0) [105] for this purpose. MadGraph is a tool to simulate particle collisions and decay processes, and is widely used in the high-energy physics community. The 3-body decay kinematics are calculated in the rest frame of the HNL, using decay diagrams calculated with FeynRules 2.0 [106] and the Lagrangians derived in [73] as input. The *Universal FeynRules Output (UFO)* from effective_HeavyN_Majorana_v103 were used for our calculation. For each mass and corresponding decay channels, we produce 1×10^6 decay kinematic variations in the rest frame and store those in a text file. During event generation, we uniformly select an event from that list, to simulate the decay kinematics of a 3-body decay.

[106]: Alloul et al. (2014), "FeynRules 2.0 - A complete toolbox for tree-level phenomenology"

[73]: Coloma et al. (2021), "GeV-scale neutrinos: interactions with mesons and DUNE sensitivity"

4.2.2 Sampling Distributions

Table 4.4: Generation level sampling distributions and ranges/values of the model-dependent simulation samples.

Variable	Distribution	Range/Value
energy	E^{-2}	[2 GeV, 1×10^4 GeV]
zenith	uniform (in $\cos(\theta)$)	[80°, 180°]
azimuth	uniform	[0°, 360°]
vertex x, y	uniform	r=600 m
vertex z	uniform	−600 m to 0 m
m_4	fixed	[0.3, 0.6, 1.0] GeV
L_{decay}	L^{-1}	[0.0004, 1000] m

In principle, the generation level sampling distributions should be chosen such that at the final level of the event selection chain the phase space relevant for the analysis is covered with sufficient statistics to make a reasonable estimate of the event expectation. Initial distributions insufficiently covering the phase space leads to an underestimation of the expected rates, because some of the events that would pass the selection are not produced. This limits the expected analysis potential. Three discrete simulation samples

were produced with HNL masses of 0.3 GeV, 0.6 GeV, and 1.0 GeV. During development of the analysis it became clear that short decay lengths were undersampled at the final selection level. Therefore, each discrete mass sample consists of a part that is generated for very short decay lengths and one for long decay lengths. The remaining sampling distributions are identical for all samples and are listed in Table 4.4. The target number of events for each sample was 2.5×10^9 at generation to result in sufficient MC statistics at final level. Figure 4.6 shows some selected generation level distributions. Additional distributions can be found in Figure A.3.

What is the message of these plots? Make it clear

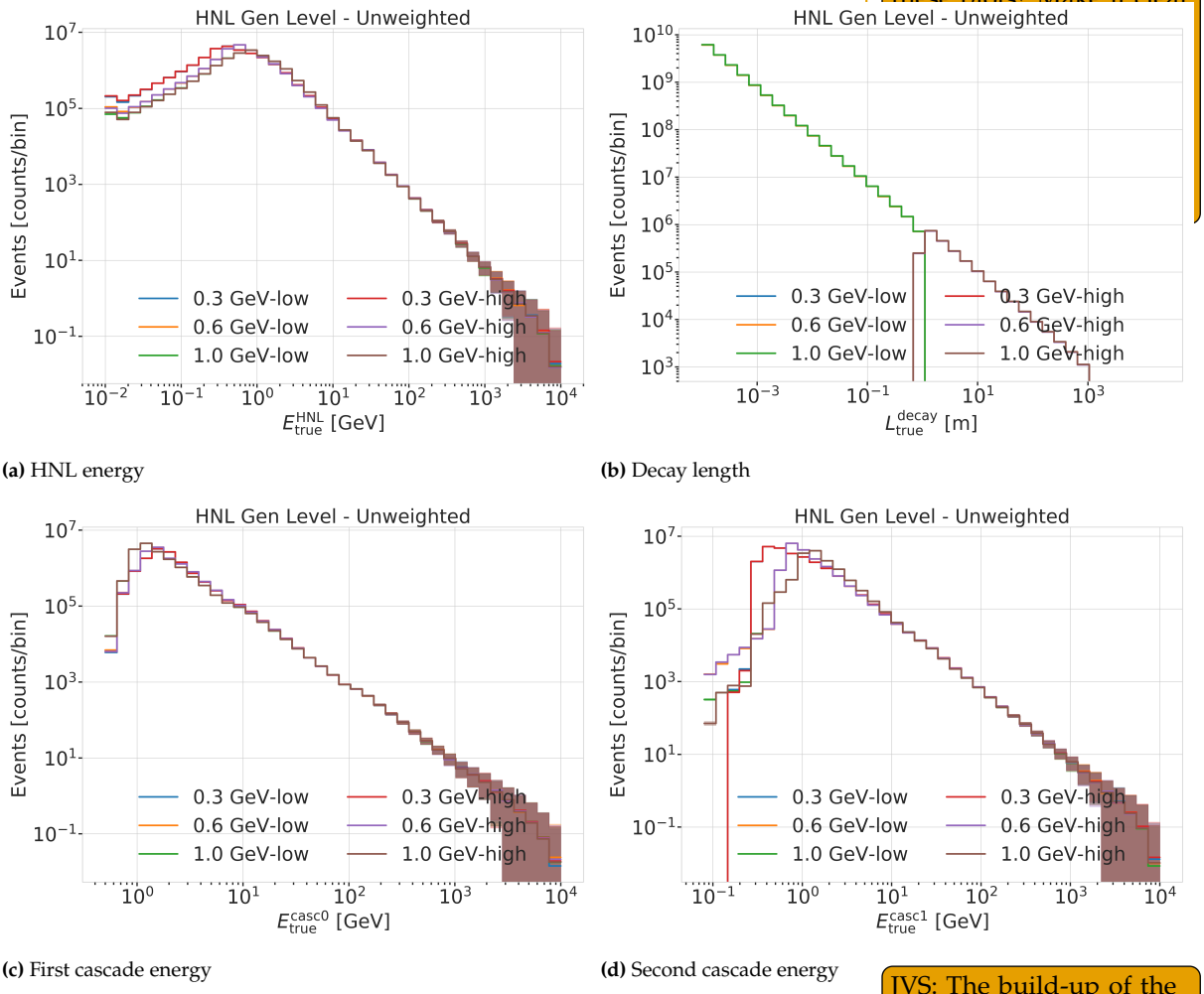

(a) HNL energy

(b) Decay length

(c) First cascade energy

(d) Second cascade energy

Figure 4.6: Generation level distributions of the model-dependent simulation.

JVS: The build-up of the weight expression is hard to follow without knowing where it's going. It may be better to start with the fact that the importance sampling weight is the ratio of PDFs, then write down each pdf, then drill down into each of the terms (basically, the standard "tell me what you're going to tell me, then tell me, then tell me what you told me" scheme). (RED)

4.2.3 Weighting Scheme

To produce physically correct event distributions based on the simplified generation sampling distributions for the HNL simulation, the forward folding method that was already introduced for the SM simulation in Section 4.3 is also used. The only required input is the mixing strength $|U_{\tau 4}|^2$, which is the variable physics parameter in this analysis. For each event the gamma factor

$$\gamma = \frac{\sqrt{E_{\text{kin}}^2 + m_4^2}}{m_4}\,, \tag{4.21}$$

is calculated, with the HNL mass m_4, and its kinetic energy E_{kin}. The speed of the HNL is calculated as

$$v = c \cdot \sqrt{1 - \frac{1}{\gamma^2}}\,, \tag{4.22}$$

where c is the speed of light. With these, the lab frame decay length range $[s_{\text{min}}, s_{\text{max}}]$ can be converted into the rest frame lifetime range $[\tau_{\text{min}}, \tau_{\text{max}}]$ for each event

$$\tau_{\text{min/max}} = \frac{s_{\text{min/max}}}{v \cdot \gamma}. \tag{4.23}$$

The proper lifetime of each HNL event can be calculated using the total decay width Γ_{total} from Section **??** and the chosen mixing strength $|U_{\tau 4}|^2$ as

$$\tau_{\text{proper}} = \frac{\hbar}{\Gamma_{\text{total}}(m_4) \cdot |U_{\tau 4}|^2}\,, \tag{4.24}$$

where $\hbar$ is the reduced Planck constant. Since the decay lengths or lifetimes of the events are sampled from an inverse distribution instead of an exponential, as it would be expected from a particle decay, we have to re-weight accordingly to achieve the correct decay lengths or lifetimes distribution. This is done by using the wanted exponential distribution

$$\text{PDF}_{\text{exp}} = \frac{1}{\tau_{\text{proper}}} \cdot e^{\frac{-\tau}{\tau_{\text{proper}}}}\,, \tag{4.25}$$

and the inverse distribution that was sampled from

$$\text{PDF}_{\text{inv}} = \frac{1}{\tau \cdot (\ln(\tau_{\text{max}}) - \ln(\tau_{\text{min}}))}\,. \tag{4.26}$$

This re-weighting factor is then calculated as

$$w_{\text{lifetime}} = \frac{\text{PDF}_{\text{exp}}}{\text{PDF}_{\text{inv}}} = \frac{\Gamma_{\text{total}}(m_4) \cdot |U_{\tau 4}|^2}{\hbar} \cdot \tau \cdot (\ln(\tau_{\text{max}}) - \ln(\tau_{\text{min}})) \cdot e^{\frac{-\tau}{\tau_{\text{proper}}}}\,. \tag{4.27}$$

Adding another factor of $|U_{\tau 4}|^2$ to account for the mixing at the interaction vertex the total re-weighting factor becomes

$$w_{\text{total}} = |U_{\tau 4}|^2 \cdot w_{\text{lifetime}}\,. \tag{4.28}$$

If this additional weighting factor is multiplied to a generation weight with units m^2 (like in Equation 4.29), the livetime in s, and the oscillated primary neutrino flux in $\text{m}^{-2}\text{s}^{-1}$, it results in the number of expected events in the detector for this particular MC event for a chosen mixing (and mass).

4.3 Background Simulation

The MC is used in the analysis by applying a method called *forward folding*, where a very large number of events (signal and background) is produced using sampling distribution that are tuned to have a large selection efficiency. Those distributions don't have to be physically correct distributions, but they need to cover the full parameter space of interest for the analysis. To produce a physical distribution, the events are weighted given a specific choice of physics and nuisance parameters. The large number of raw MC

Flavor	Energy [GeV]	Radius [m]	Length [m]	Events/File	Files
$\nu_e + \bar{\nu}_e$	1-4	250	500	450000	650
	4-12			100000	
	12-100	350	600		
	100-10000	550	1000	57500	
$\nu_\mu + \bar{\nu}_\mu$	1-5	250	500	408000	1550
	5-80	400	900	440000	
	80-1000	450	1500	57500	
	1000-10000	550		6700	
$\nu_\tau + \bar{\nu}_\tau$	1-4	250	500	1500000	350
	4-10			300000	
	10-50	350	600	375000	
	50-1000	450	800	200000	
	1000-10000	550	1500	26000	

Table 4.5: Cylinder volumes used for GENIE neutrino simulation generation. Cylinder is always centered in DeepCore at $(x, y, z) = (46.29, -34.88, -330.00)$ m.

events ensures a good estimation of the expected numbers and weighted distributions.

The analysis itself is then performed by comparing the weighted MC distributions to the observed data. This is done by binning them as described in Chapter 7 and calculating a loss function comparing the bin expectations to the data. The physics and nuisance parameters that best correspond to the observed data are estimated by minimizing this loss function. In order to achieve a reliable result with this method the MC needs to be precise and as close to the data as possible (at least at the final event selection).

4.3.1 Neutrinos

Due to the very low interaction rate of neutrinos, the event generation is performed in a way that forces every event to interact in a chosen sampling volume. The weight of each event is then calculated as the inverse of the simulated neutrino fluence

$$w_{\text{gen}} = \frac{1}{F_{\text{sim}}} \frac{1}{N_{\text{sim}}} , \tag{4.29}$$

where F_{sim} is the number of neutrino events per energy, time, area, and solid angle and N_{sim} is the number of simulated events. If this weight is multiplied by the livetime and the theoretically expected neutrino flux for a given physical model, it results in the number of expected events in the detector for this particular MC event. The baseline neutrino flux used in this thesis, computed for the South Pole, is taken from Honda *et al.* [75].

[75]: Honda et al. (2015), "Atmospheric neutrino flux calculation using the NRLMSISE-00 atmospheric model"

The simulation volume is a cylinder centered in DeepCore with radius and height chosen such that all events possibly producing a signal are contained. The different sizes, chosen depending on energy and neutrino flavor, are shown in Table 4.5. The directions of the neutrinos are sampled isotropically and the energies are sampled from an E^{-2} power law. The number of simulated events is chosen such that the livetime is more than 70 years for each flavor. Neutrinos and antineutrinos are simulated with ratios of 70% and 30%, respectively.

To simulate the neutrino interaction with the ice, the GENIE event generator [107] (version 2.12.8) is used, resulting in the secondary particles and the kinematic and cross-section parameters. As input, the outdated GRV98LO [108] *parton distribution functions (PDFs)* was used, because it was the only option that could incorporate extrapolations to lower Q^2 [109]. Muons produced in these interactions are propagated using PROPOSAL [110], also simulating their Cherenkov light output. The shower development of gamma rays, electrons, and positrons below 100 MeV and hadronic showers below 30 GeV is simulated using Geant4 [96] while for higher energies an analytical approximation from [92] is used.

4.3.2 Muons

Atmospheric muons are generated on a cylinder surface enclosing the full IceCube detector array. The cylinder has a height of 1600 m and a radius of 800 m. The energy is sampled from an E^{-3} power law while the other sampling distributions (position, direction) are found from parameterizations based on [111]. This work uses full CORSIKA [112] simulations of muons to tailor the parameterizations, starting from *cosmic ray (CR)* interactions with atmospheric nuclei using the CR flux model from [113] and producing the muons applying the *hadronic interaction (HI)* model SIBYLL 2.1 [114]. After the generation, they are propagated through the ice with PROPOSAL producing photons, treating them exactly like the muons produced in neutrino interactions.

Since the offline processing and selection steps described in Section 5.2.2 and Section 5.3 reduce the muon contamination to an almost negligible level, the statistical uncertainty on the number of expected muon events at the final selection level is large and therefore two separate sets of muon simulation are produced. **A first set** including all events resulting from the above described generation to tune the lower level selection (up to L4) and **a second set** to estimate the muon contamination at higher levels (above L5), which only accepts muon events if they pass through a smaller cylinder centered in DeepCore (height of 400 m and radius of 180 m) and rejects events based on a KDE estimated muon density at L5 (in energy and zenith) increasing the simulation efficiency at L5 significantly.

[107]: Andreopoulos et al. (2015), "The GENIE Neutrino Monte Carlo Generator: Physics and User Manual"

[108]: Glück et al. (1998), "Dynamical parton distributions revisited"

[109]: Bodek et al. (2003), "Higher twist, xi(omega) scaling, and effective LO PDFs for lepton scattering in the few GeV region"

[110]: Koehne et al. (2013), "PROPOSAL: A tool for propagation of charged leptons"

[96]: Agostinelli et al. (2003), "Geant4—a simulation toolkit"

[92]: Rädel et al. (2012), "Calculation of the Cherenkov light yield from low energetic secondary particles accompanying high-energy muons in ice and water with Geant4 simulations"

[111]: Becherini et al. (2006), "A parameterisation of single and multiple muons in the deep water or ice"

[112]: Heck et al. (1998), "CORSIKA: A Monte Carlo code to simulate extensive air showers"

[113]: Gaisser (2012), "Spectrum of cosmic-ray nucleons, kaon production, and the atmospheric muon charge ratio"

[114]: Engel et al. (2017), "The hadronic interaction model Sibyll – past, present and future"

Standard Model Background Simulation and Data Processing

5

Adapt chapter to reflect switched chapter order (RED)

The analysis presented in this thesis is highly dependent on an efficient event selection to reduce the raw IceCube trigger data to a usable atmospheric neutrino sample. Based on this selection, a precise estimation of both expected SM background and expected BSM signal events can be made using MC simulations. This chapter describes the current simulation and event selection chain used for state-of-the-art IceCube neutrino oscillation measurements like [115]. The whole chain can be broadly split into 4 steps:

[115]: Abbasi et al. (2023), "Measurement of atmospheric neutrino mixing with improved IceCube DeepCore calibration and data processing"

Step 1 Event Generation: The initial step for all particle (non-noise) simulation is the generation of events from selected initial distributions and fluxes. Events are the primary particle and the particles produced in the interaction with the ice.

Step 2 Detector Simulation: The particles from the first step are propagated through the ice, producing Cherenkov photons, which are then propagated further until they reach a DOM or are absorbed. If they hit a DOM the detector response (acceptance and PMT) is simulated.

Step 3 Processing: Starting from the PMT output, both real data and simulation are processed through the in-ice trigger, the online filter and processing, and the low-energy event selection to produce a neutrino dominated sample.

Step 4 Reconstruction: Once the sample is small enough for more sophisticated reconstruction techniques to be feasible to run, the events are reconstructed using a CNN and some high level variables are computed. Based on these variables the final event selection is applied.

This chapter only describes the event generation for the SM background simulation (neutrinos and muons), while the signal simulation is described in Chapter 4. The detector simulation is identical for both signal and background events while processing and reconstruction are applied to all simulation and data in the same way. Splitting the simulation steps has the advantage of reusing the outputs of for example the generation step to propagate the particles with different ice model, in order to estimate the systematic impacts of uncertainties of the ice properties. Similar approach can be taken for varying detector response and through this a more efficient (reduced) use of computing resources can be achieved. The following sections describe the different steps in more detail and the last section, Section 5.4, describes the related systematic uncertainties considered for this work.

5.1 Detector Simulation

The detector simulation is performed after the event generation, where the initial particles and the resulting photons and secondary particles from their propagation were produced. This part of the simulation chain is applied to all muon and neutrino simulation as well as the HNL signal simulation explained in detail in Chapter 4. The detector simulation can be split into

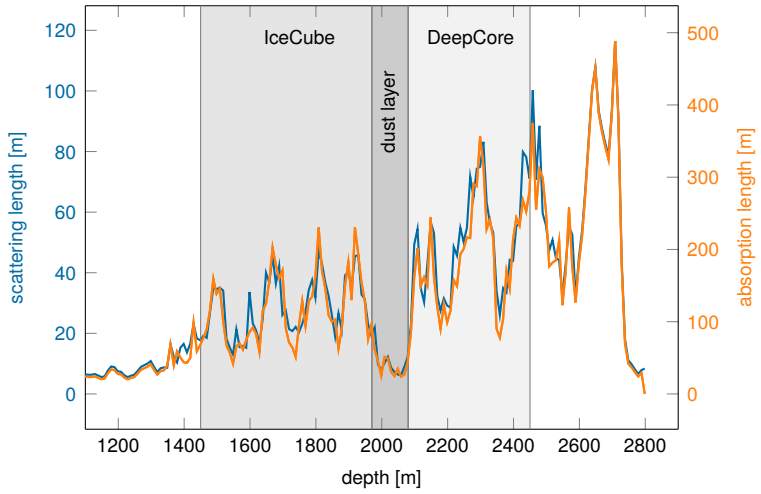

Figure 5.1: Scattering and absorption lengths in the SPICE model used for simulation production as a function of depth, modified from [19].

two parts, the propagation of the photons and the simulation of the detector response (including internal noise).

5.1.1 Photon Propagation

Any photon that was produced in the event generation is individually traced through the ice, simulating scattering and absorption processes. The propagation is done using CLSIM [116] which is an implementation of the *Photon Propagation Code (PPC)* [117] in OpenCL. It is optimized to be run very efficiently on GPUs, which is what is done for IceCube simulation production. The ice is modeled as a set of 10 m thick, almost horizontal layers with specific absorption and scattering lengths. The *South Pole ice (SPICE)* model [118] accounts for the layers being tilted by a small amount (() and the absorption and scattering lengths having a non-uniformity with respect to the azimuth direction. Figure 5.1 shows the values of this model for the different depths, indicating the location of IceCube, DeepCore, and the dust layer.

[117]: Chirkin et al. (2019), "Photon Propagation using GPUs by the IceCube Neutrino Observatory"

[118]: Aartsen et al. (2013), "Measurement of South Pole ice transparency with the IceCube LED calibration system"

put a number on the tilt angle? (YELLOW)

In an initial step, each photon's absorption length is sampled from an exponential distribution with the expectation value at the current layer's absorption length. The following propagation steps are performed in parallel for all photons. In each of those steps, corresponding to a single scattering event, the photon travels a length that is sampled from an exponential distribution with the expectation value at the scattering length of the current layer and the scattering angle chosen based on a combination of a simplified Mie scattering distribution [119] and a Henyey-Greenstein distribution [120]. The parameters defining the shape of these distributions were calibrated using data from *in-situ* LED calibration runs. These steps are continuously repeated until each photon reached a DOM or was absorbed[1]. After all photons have been propagated in that manner, the final step is to output the photons that reached a DOM for further processing.

[119]: Mie (1908), "Beiträge zur Optik trüber Medien, speziell kolloidaler Metallösungen"

[120]: Henyey et al. (1941), "Diffuse radiation in the Galaxy."

1: A photon is absorbed, when it traveled its full absorption length, sampled in the initial step of the photon propagation.

5.1.2 Detector Responses

The second part of simulating the IceCube detector is the DOM response. Whether a photon that reached a DOM produces a signal depends on the

total efficiency and the angular acceptance curve of the specific DOM. The total efficiency includes effects of the DOM glass, PMT quantum and photo-electron collection efficiencies, and it is wavelength dependent. Additionally, there is another angle dependent effect called *hole ice* [121]. This effect is due to varied ice properties resulting from the re-freezing process of the water column inside the borehole after deployment of the string. Accepted photons are converted into a so-called *Monte Carlo photo-electron (MCPE)*. The amount of charge measured for each MCPE is determined by sampling from a mixture of two exponential distributions and a normal distribution. This *single photo-electron (SPE)* distribution was tuned to match the observed distribution in each DOM in an *in-situ* calibration study [122]. Figure 5.2 shows the distribution compared to a lab measurement. Based on the sampled charges and times of MCPEs, the voltage waveforms for the (two) different readout channels are simulated and passed on to the trigger simulation starting with *WaveDeform*, which was already mentioned in Section 3.1.1.

[121]: Fiedlschuster (2019), "The Effect of Hole Ice on the Propagation and Detection of Light in IceCube"

[122]: Aartsen et al. (2020), "In-situ calibration of the single-photoelectron charge response of the IceCube photomultiplier tubes"

Parameter	Value
Therm. rate λ_{th}	180 Hz
Decay rate λ_{dec}	80 Hz
Decay hits η	8.5
Decay μ	4.3 $\log_{10}$(ns)
Decay σ	1.8 $\log_{10}$(ns)

Table 5.1: Typical parameter values used in the vuvuzela noise simulation. Averaged over all DOMs.

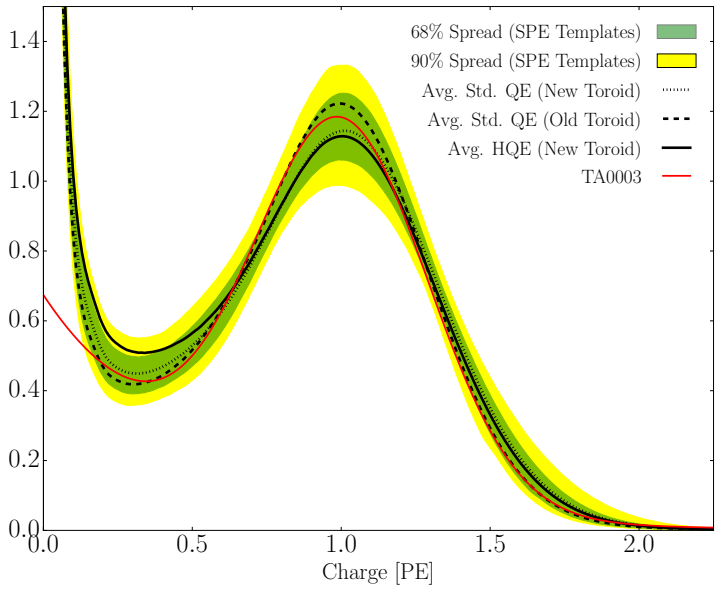

Figure 5.2: Single photo-electron charge distribution shown for a lab measurement in red (TA0003), various hardware configurations in black dashed, dotted, and solid lines, and the 68 % and 90 % spread of the measured charged templates for all DOMs. All curves are normalized to the same area. The figure is taken from [122].

Besides the Cherenkov photons, IceCube also observes photons that are produced in radioactive decays inside the DOMs, both in the glass housing sphere and the PMT glass itself. To simulate this internal noise, the *Vuvuzela* module [123, 124] is used to create additional MCPEs that are fed into the same simulation chain described above. This module takes into account thermal and non-thermal components and their times are sampled using parameterizations of the measured distributions, where the thermal noise component is uncorrelated photons and the non-thermal component is from burst of photons. The noise hits are simulated by drawing the times from a constant rate Poisson process and the number of photons from a Poisson distribution. Then the time differences between the individual photons per hit is found, based on a Log-Normal distribution. The simulation is defined by 5 parameters that are calibrated for each DOM individually. Table 5.1 shows the average values for these parameters.

[123]: Larson (2013), "Simulation and Identification of Non-Poissonian Noise Triggers in the IceCube Neutrino Detector"
[124]: Larson (2018), "A Search for Tau Neutrino Appearance with IceCube-DeepCore"

5.2 Processing

After the detector simulation is performed, all MC and data are processed in exactly the same way. This section explains the trigger and event selection that is applied starting from the raw voltage measured by the PMTs. Most parts of this processing are identical to the procedure already described in [19, 125]. It is split in different steps run inside the ice, at the South Pole, and after the data was transferred to the North. The complexity and computational cost of the processing increases with each step, while the total number of events reduces, making it feasible and reducing the use of computational resources on events that are not of interest for the analysis.

[19]: Trettin (2023), "Search for eV-scale sterile neutrinos with IceCube DeepCore"
[125]: Lohfink (2023), "Testing non-standard neutrino interaction parameters with IceCube-DeepCore"

5.2.1 Trigger and Filter

Before the data can be sent to the North, the initial signal coming from the PMT is a voltage waveform that has to be digitized (for data) and then information of photon hits has to be extracted (also for the MC coming from the detector response simulation). The trigger and filter explained here are tailored to select events that passed through the DeepCore volume, while rejecting background events (either from atmospheric muons or from random noise). There are other filters used in IceCube which will not be explained here, since they are not relevant for this work. A full description of the instrumentation and the online systems can be found in [126].

[126]: Aartsen et al. (2017), "The IceCube Neutrino Observatory: Instrumentation and Online Systems"

Include some low level plots like the trigger efficiency for the HNL simulation (ORANGE)

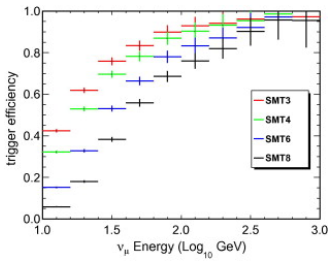

Figure 5.3: Efficiencies of different IceCube and DeepCore triggers, taken from [87].

[83]: Abbasi et al. (2009), "The IceCube data acquisition system: Signal capture, digitization, and timestamping"
[6]: Aartsen et al. (2017), "The IceCube Neutrino Observatory: instrumentation and online systems"
[87]: Abbasi et al. (2012), "The design and performance of IceCube DeepCore"

In-ice Trigger

The trigger is applied inside the DOM in the ice before sending the information to the ICL on the surface. The time dependent voltage curves are captured if a pre-defined threshold value is exceeded. Once the threshold set to the equivalent of 0.25 PE is crossed, 6.4 µs of the waveform are coarsely digitized by a *Fast Analog-to-Digital Converter (FADC)* with a sampling rate of 40 MHz. Additionally, the first 427 ns are digitized using an *Analog Transient Waveform Recorder (ATWD)* with a sampling rate of 300 MHz [83], but only if some trigger condition is met, because this readout frequency is too high to be sampled directly and requires some buffering. For DeepCore, the HLC condition already mentioned in Section 3.1.1 has to be met for three DOMs inside the fiducial volume within a time window of 5 µs. If this is the case, all waveforms that crossed the threshold within a 20 µs time window around the trigger are digitized and sent to the ICL for further processing. This trigger is called *Simple Multiplicity Trigger 3 (SMT-3)*. The DOM hits that are read out in this process, but do not meet the HLC condition, are called *soft local coincidence (SLC)* hits. The rate of the DeepCore SMT-3 trigger is ~250 Hz [6], accepting ~70 % of ν_μ-CC events at 10 GeV and ~90 % at 100 GeV [87]. The trigger efficiencies for different SMT triggers, including the DeepCore SMT-3, are shown in Figure 5.3.

Online Filter

The digitized waveforms are sent to the ICL, where a further filter is applied *online*[2]. First, the WaveDeform algorithm is run to extract photon arrival times and charge from the waveforms, then the DeepCore filter is applied,

2: Where *online* means running on hardware at the South Pole.

which is an iterative hit cleaning starting from HLC hits and removing any hits outside a 125 m radius and a 500 ns time window (called *radius-time cleaning (RT-cleaning)*) of the initial hit. This mainly rejects unphysical SLC hits, which are potentially caused by random noise. The following selection steps are done using the resulting cleaned pulses.

Next, an additional cut is applied to reject events that are likely to be caused by atmospheric muons. This is done by splitting the hits depending on whether they were inside the DeepCore fiducial volume or outside and then calculating the speed of each hit outside the fiducial volume towards the *center of gravity (COG)* of the hits inside. If one of them has a speed close to the speed of light, the whole event is rejected, because this is a strong indication for a muon event.

As input for the further selection levels, a few event properties, like vertex position and direction, are determined using fast and simple event reconstructions. After the DeepCore online filter, the rate is about 15 Hz, which can be sent to the North via satellite for further processing.

5.2.2 Event Selection

After the data was sent to the North, the *offline* filters and selection are applied to further recude reduce the background of atmospheric muons and noise. The selection is split into three levels referred to as *Level 3-5 (L3-L5)*, which bring down the neutrino and muon rate to ∼1 mHz, while the remaining fraction of random noise is below 1 %.

Level 3

At the first offline filtering level, Level 3, 1D cuts are used to reduce atmospheric muons, pure noise, and coincident muons. These cuts are targeting regions where the data/MC agreement is poor, so that more sophisticated *machine learning (ML)* techniques can be applied at later levels. The cuts are made using 12 control variables, that are inexpensive to compute for the very large sample at this stage. The variables are related to position, time, and overall number of hits in the event.

Pure noise hits, that are temporally uncorrelated, are cleaned by applying a 300 ns sliding window, requiring the containment of more than 2 hits at its maximum. Additionally, an algorithm is run to check whether the hits show some directionality, accepting them only if they do.

To reduce the amount of muons a series of cuts is applied using spatial and temporal information. Events that have more than 9 hits observed above −200 m or the first HLC hit above −120 m are rejected as well as events where the fraction of hits in the first 600 ns of the event is above 0.37, ignoring the first two hit DOMs. Additionally, the ratio between hits in the veto region and the DeepCore fiducial volume is required to be below 1.5.

If a muon enters the detector after the data acquisition was already triggered, it causes events that span over a much larger time range. To reduce those coincident events, the time difference between first and last pulse cannot be above 5000 ns. This cut mainly affects a region of very poor data to MC agreement, because coincident events are not simulated at all.

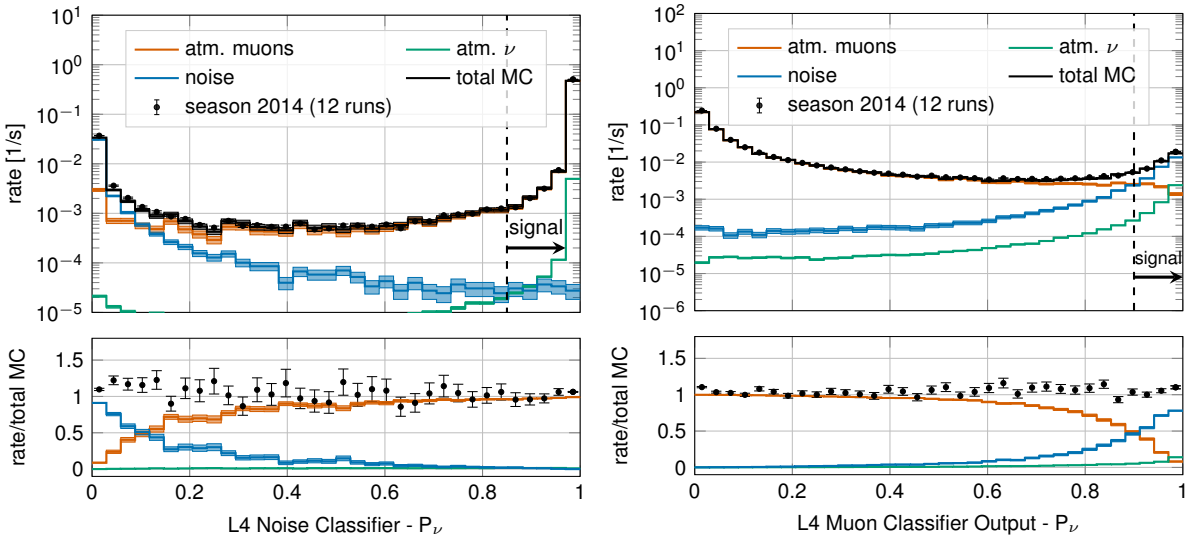

Figure 5.4: Distributions of Level 4 noise classifier output (left) and muon classifier output (right), where larger values indicate more neutrino-like and lower values more noise-like/muon-like. Taken from [115].

The L3 cuts remove 95 % of the atmospheric muons and >99 % of pure noise hits, while keeping >60 % of the neutrino events. The sample now roughly contains muons/neutrinos/noise at a ratio of 100:10:1 with a total rate of ~0.5 Hz.

add example plots (2?) for L3 cut variables and applied cuts (YELLOW)

Level 4

After the total rate was reduced by the simple cuts of L3 and the overall agreement between data and MC is established, ML techniques can be applied to further reduce the background. For Level 4, two *Boosted Decision Trees (BDTs)* [127] classifier are trained to separate neutrino events from atmospheric muons and noise hits, separately. The output of each classifier, a probability score, can be seen in Figure 5.4. The noise filter is applied first and an event passes the score if it is larger than 0.7, reducing the noise hits by a factor of 100, while keeping 96 % of neutrinos. Then the second BDT classifier is applied to reject muons. It was trained partly on unfiltered data, which consists of >99 % atmospheric muons, to reject the data and keeping the neutrinos from the simulation. Rejecting events with a score smaller than 0.65 removes 94 % of atmospheric muons while keeping 87 % of neutrinos. This fraction varies depending on the flavor and interaction type, ν_μ-CC events for example, which have a muon in the final state, are therefore reduced to 82.5 %. After applying the L4 cuts based on the BDT classifier outputs, the sample is still dominated by atmospheric muons, while the noise rate dropped to below most neutrino types.

[127]: Friedman (2002), "Stochastic gradient boosting"

Level 5

Level 5 is the final selection level, before event reconstructions are applied. This level aims to reduce the remaining atmospheric muon rate below the rate of neutrinos. Muons not rejected by the earlier levels are those that produced little or no light in the veto regions. One possible reason is that they passed through one of the un-instrumented regions between the strings called *corridors*. To reject those, special corridor cuts, based on the number

add some figure showing the corridors? (YELLOW)

of hits they produced close to a potential corridor they passed through. The potential corridor in questions is identified based on a simple infinite track fit. In addition to the corridor cuts, starting containment cuts are applied to reject events that start at the edge of the fiducial volume. Events with more than seven hits in the outermost strings of the detector or those that have a down going direction in the uppermost region are rejected. This further reduces the fraction of muons by 96 % while keeping 48 % of neutrinos. The rates after this level are 1 mHz and 2 mHz for neutrinos and muons, respectively, making it a neutrino dominated sample.

add table with rates per level (split in flavor) - maybe better in analysis chapter to also show signal? (RED)

5.3 Reconstruction

In the energy range most relevant for this work, between 10 GeV and 100 GeV, the light deposition is very low and only a few DOMs detect light, making the reconstructions difficult. In [128] two classical methods are described, which have partly been applied in one recent IceCube atmospheric neutrino oscillation measurement using a sub-sample of the DeepCore sample [115]. The algorithm used in this work on the other hand, is a newer method that applies a *convolutional neural network (CNN)* to reconstruct the events and determine some discriminating quantities. The latest muon neutrino disappearance result from IceCube [129] is based on this reconstruction.

[128]: Abbasi et al. (2022), "Low energy event reconstruction in IceCube DeepCore"

[115]: Abbasi et al. (2023), "Measurement of atmospheric neutrino mixing with improved IceCube DeepCore calibration and data processing"

[129]: Yu et al. (2023), "Recent neutrino oscillation result with the IceCube experiment"

5.3.1 Fast Low-Energy Reconstruction using Convolutional Neural Networks

As the name *Fast Low-Energy Reconstruction using Convolutional Neural Networks (FLERCNN)* already indicates, the FLERCNN reconstruction [130, 131] is a CNN optimized to reconstruct IceCube events at low energies (<100 GeV) in a fast and efficient manner, by leveraging the approximate translational invariance of event patterns within the detector. The architecture of the network is very similar to the preexisting IceCube CNN event reconstruction [132], but optimized on low-energy events and specifically tailored to include the DeepCore sub-array. Only the eight DeepCore strings and the central 19 IceCube strings are used for the reconstruction (compare to Figure 3.4). Because of the different z-positions of the DeepCore and IceCube DOMs, they are divided into two networks that are combined in the final layer of the network. The full architecture is shown in Figure 5.5. The first dimension of the network is the string index, while the second dimension is the order of the DOMs along the vertical axis. The horizontal position of the DOMs is not used, since the strings are arranged in an irregular pattern. The information from the DOM hits is summarized into five charge and time variables, which make up the last dimension of the input layer. The variables are the total summed charge, the time of the first hit, the charge weighted mean time of the hits, the time of the last hit, and the charge weighted standard deviation of the hit times.

[130]: Yu et al. (2021), "Direction reconstruction using a CNN for GeV-scale neutrinos in IceCube"
[131]: Micallef (),

[132]: Huennefeld (2017), "Deep Learning in Physics exemplified by the Reconstruction of Muon-Neutrino Events in IceCube"

add image with selected strings used for flercnn IC and DC (YELLOW)

Five different networks are trained using this architecture. Three networks do the regression of the events' energy, zenith angle, and the starting vertex (x, y, z position), while two of them are used for classification. One is trained to predict the probability of the event being a track (used as PID) and the other to predict the probability of the event being a muon. Each network is trained with an MC sample modified to have a flat distribution in the target

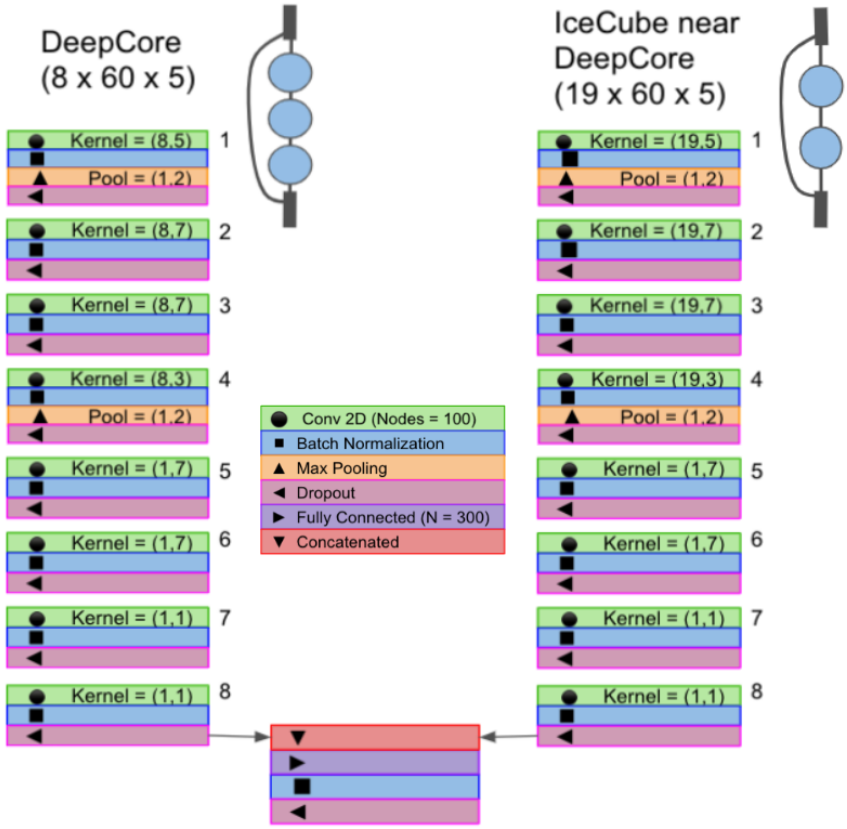

Figure 5.5: Architecture of the FLERCNN neural networks, taken from [130].

variable, to be unbiased for that variable and ideally extending outside the target reconstruction region. For the classification tasks the loss function is the *binary cross entropy* and the activation function is a *sigmoid*. To perform the regression of zenith and vertex position, the loss function is the *mean squared error (MSE)*, while for the energy it is the *mean absolute percentage error*. The activation for all regression tasks is *linear*.

add some performance plots of the FLERCNN reconstruction (ORANGE)

There is more information on pre-processing the samples and preparing the input features, and training each cnn, but I'm not sure if that might be too much detail? (YELLOW)

5.3.2 Analysis Selection

Before the reconstruction is applied a few additional high level variables are computed, which are from fast and inexpensive algorithms. Then the reconstruction is performed by applying the trained FLERCNN networks to get the output quantities. After that, another BDT classifier is trained to further reduce the muon background for the final sample. The BDT is trained on five high level variables, where three are FLERCNN reconstruction variables (vertex z, ρ_{36}[3], and muon probability) and two are lower level variables (L4 muon classifier output and L5 corridor cut variable). To train the BDT, the FLERCNN nominal simulation set is used, only using events with $\cos(\theta_{zenith}) \leq 0.3$. The output of the BDT is the neutrino probability and a cut at 0.8 is applied to reject events with a high probability of being a muon. Figure 5.6 shows the output of the BDT classifier, where the neutrinos in both training and testing sets are gathered at 1 and muons are around 0, which shows great classification power.

3: A radial variable that is often used in IceCube, is the horizontal distance to string 36 called ρ_{36}, which is basically the distance to the center of IceCube.

add reference for flercnn analysis internal note (ORANGE)

To get the final, pure sample of well reconstructed neutrinos another set of cuts is applied. The first cuts are meant to reject events with poor reconstruction quality, by requiring the events to fall into the DeepCore

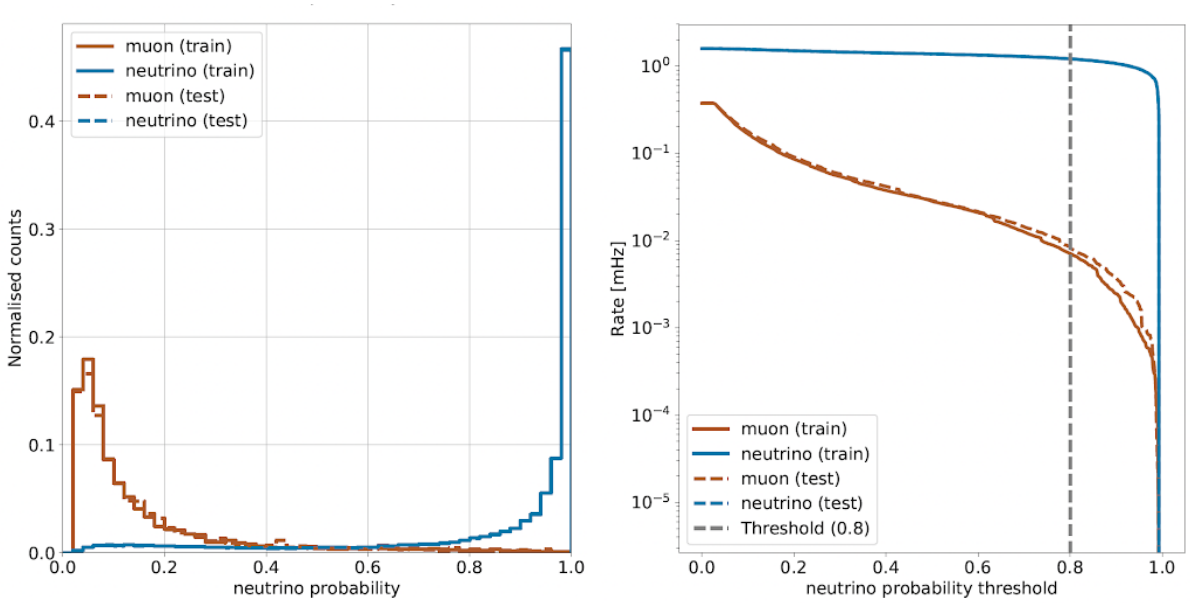

Figure 5.6: FLERCNN muon classifier output score (left) and rate of neutrinos and muons as function of muon classifier cut (right). Taken from [**flercnn_analysis_internal_note**]

Variable	Threshold	Removed
Number of hit DOMs	≥ 7	1.05 %
Radial distance	$< 200\,\mathrm{m}$	0.09 %
Vertical position	$-495\,\mathrm{m} < z < -225\,\mathrm{m}$	5.48 %
Energy	$5\,\mathrm{GeV} < E < 100\,\mathrm{GeV}$	20.70 %
Cosine of zenith angle	< 0.04	19.66 %
Number of direct hits	> 2.5	10.50 %
Number of hits in top layers	< 0.5	0.03 %
Number of hits in outer layer	< 7.5	0.001 %
Muon classifier score	≥ 0.8	23.90 %

Table 5.2: Cuts performed to select the final analysis sample. Parts of the cuts are meant to increase the data/MC agreement, while others are meant to reject events with poor reconstruction quality.

volume, where the denser, better instrumented detector leads to enhanced resolution. The cuts are applied on the vertex z and ρ_{36} and are listed in Table 5.2. The FLERCNN reconstruction was optimized for atmospheric neutrino analyses which are mainly in the region below 100 GeV and there are very few events with energies below 5 GeV, so the reconstructed energy is required to be in that range. Additionally, rejecting events with fewer than seven hits in the selected DOMs used for FLERCNN showed to increase the resolution.

Another set of cuts is applied to make sure the agreement between data and MC is good. To remove coincident muon and neutrino events, cuts are applied to the number of hits in the top 15 layers of IceCube DOMs and the number of hits in the outermost IceCube strings. Coincident random noise events are removed by requiring more than three hit DOMs from direct photons[4]. Neither of the two coincident event types are simulated, which can be seen as bad agreement between data and MC. The last cut is on the reconstructed cosine zenith, which is required to be smaller than 0.04 to reject down-going muons.

4: *Direct photons* are photons that were not scattered on their way from the interaction vertex to the DOM.

5.4 Systematic Uncertainties

There are multiple sources of systematic uncertainties related to the event generation and processing explained in this chapter. All uncertainties considered in this work need to be implemented with parameters that can be varied continuously so that a simultaneous fit of the physics and systematic parameters can be performed. Where possible, a correct model of the effect is used, but in many cases the variations are captured by effective parameters. Uncertainties that solely scale the total event rate are not included individually, since the analysis only uses the relative distribution of events and a single scaling parameter N_ν is used to scale the total neutrino rate instead.

5.4.1 Atmospheric Flux Uncertainties

The flux of atmospheric neutrinos is influenced by multiple factors, the spectrum and composition of CRs, the assumed atmospheric conditions, and the HI model used to describe the air showers development. Uncertainties of the neutrino flux are therefore dictated by the uncertainties on these components, where the variations in atmospheric conditions were found to have negligible effect [115].

[115]: Abbasi et al. (2023), "Measurement of atmospheric neutrino mixing with improved IceCube DeepCore calibration and data processing"

Cosmic ray flux: The selected sample of atmospheric neutrinos lies around energies of up to 100 GeV. The initial primary particles in the CR flux can have 100 times larger energies and therefore the CR flux between 10 GeV and 10 TeV is important, which dominantly consists of hydrogen and helium nuclei [133]. The uncertainty in this CR flux component can be described as a power law correction [134, 135]

[133]: Dembinski et al. (2017), "Data-driven model of the cosmic-ray flux and mass composition from 10 GeV to 10^{11} GeV"
[134]: Barr et al. (2006), "Uncertainties in atmospheric neutrino fluxes"
[135]: Evans et al. (2017), "Uncertainties in atmospheric muon-neutrino fluxes arising from cosmic-ray primaries"

$$\Phi'_\nu = \Phi_\nu \left(\frac{E}{E^\star} \right)^{\Delta\gamma} , \tag{5.1}$$

where $E^\star$ is the pivot energy and $\Delta\gamma$ is the correction to the power law exponent. This modification propagates into the neutrino flux, which is therefore corrected in the same way. $E^\star$ was chosen to be 24 GeV as to minimize the dependence of the overall flux scale on $\Delta\gamma$ [115].

[115]: Abbasi et al. (2023), "Measurement of atmospheric neutrino mixing with improved IceCube DeepCore calibration and data processing"

Hadronic interaction model: Neutrinos are produced in the decaying hadrons in CR air showers, spanning a large parameter space that is sparsely evaluated by experimental data. To include uncertainties based on energy, direction, and neutrino flavor, the MCEq package [136] is used to compute the distribution of atmospheric leptons and to estimate the impact of varying their contributions. The calculations result in the change in flux $d\Phi_l/dB$ for a variation dB of some parameter B. Scaling this variation by some value b, the modified total flux, s is then given by

[137]: Barr et al. (2006), "Uncertainties in Atmospheric Neutrino Fluxes"
[138]: Riehn et al. (2020), "Hadronic interaction model sibyll 2.3d and extensive air showers"
[133]: Dembinski et al. (2017), "Data-driven model of the cosmic-ray flux and mass composition from 10 GeV to 10^{11} GeV"

$$\Phi'_l = \Phi_l + \left(b \cdot \frac{d\Phi_l}{dB} \right) . \tag{5.2}$$

Matching the work in [137], the parameter space is divided in regions of the primary energy, E_i, and the energy fraction of the secondary meson, x_{lab}, with varying uncertainties, derived from fixed target experiment data. The Sibyll2.3c [138] HI model and the GSF CR flux [133] were used to calculate

the related flux changes[5] for the different regions in E_i and x_{lab}, resulting in 17 variables, encoding the possible changes. Figure 5.7 shows the selected regions of the parameter space and the names given to the uncertainties. The variational term in Equation 5.2 is applied for each of these parameters and the total variation is the sum of all individual variations.

5: The choice of flux and HI model have minor impact on the variations.

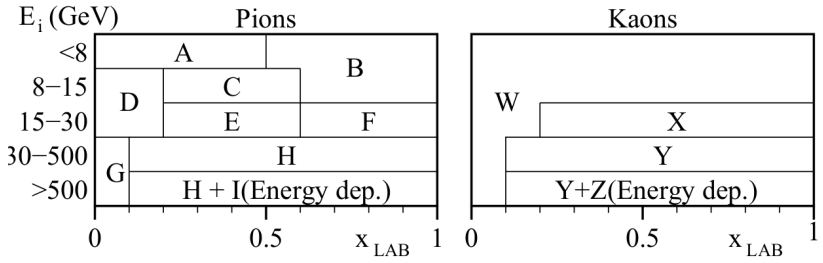

Figure 5.7: Flux uncertainty regions of the hadronic interaction model in the phase space of the primary energy E_i and the energy fraction of the secondary meson x_{lab}. Taken from [137].

5.4.2 Cross-Section Uncertainties

The uncertainties related to the cross-sections are split into low and high energy components, since there is no coherent model to explain both DIS interactions, which are the dominant processes above 20 GeV, and *charged current resonance production (CCRES)* and *charged current quasi elastic scattering (CCQE)*, which are relevant below 20 GeV where interactions with the nucleons as a whole are important. Three parameters are included to account for all relevant cross-sections uncertainties.

At low energies two parameters are included accounting for uncertainties in form factors of CCQE and CCRES events. These uncertainties are due to uncertainties in the *axial mass* M_{A}, which enters the form factor as in

$$F(Q^2) \sim \frac{1}{(1 - (\frac{Q}{M_{\text{A}}})^2)^2}\,, \tag{5.3}$$

where Q^2 is the momentum transfer squared. The axial mass can be determined experimentally and to include uncertainties on the values of $M_{\text{A}}^{\text{CCQE}}$ and $M_{\text{A}}^{\text{CCRES}}$, the cross-sections are computed with GENIE, where the form factors are calculated varying the axial mass by $\pm 20\%(1\sigma)/\pm 40\%(1\sigma)$ around the nominal value. This is an approximation of the recommended uncertainties by the GENIE collaboration, which are -15%, $+25\%$ for $M_{\text{A}}^{\text{CCQE}}$ and $\pm 20\%$ for $M_{\text{A}}^{\text{CCRES}}$ [107]. To apply a continuous uncertainty variation of the axial mass in a fit, the total cross-section is fit with a quadratic function to interpolate between the cross-sections computed with the different axial masses.

which experiments measure the axial mass? (ORANGE)

Even though the DIS interactions can be calculated very precisely, there are still uncertainties in the input PDF, describing the probability of finding a specific parton (quark) with a specific momentum fraction x inside a nucleon. To account for differences between the used method and more sophisticated methods using newer PDFs seen at high energies, an uncertainty parameter is introduced. The parameter is based on the discrepancy between the cross-sections computed with GENIE and the ones computed with CSMS [139] above 100 GeV. The included parameter scales the cross-section from the GENIE values to the CSMS values, which are considered more accurate above 100 GeV. The scaling is done as a function of energy and inelasticity and to

[139]: Cooper-Sarkar et al. (2011), "The high energy neutrino cross-section in the Standard Model and its uncertainty"

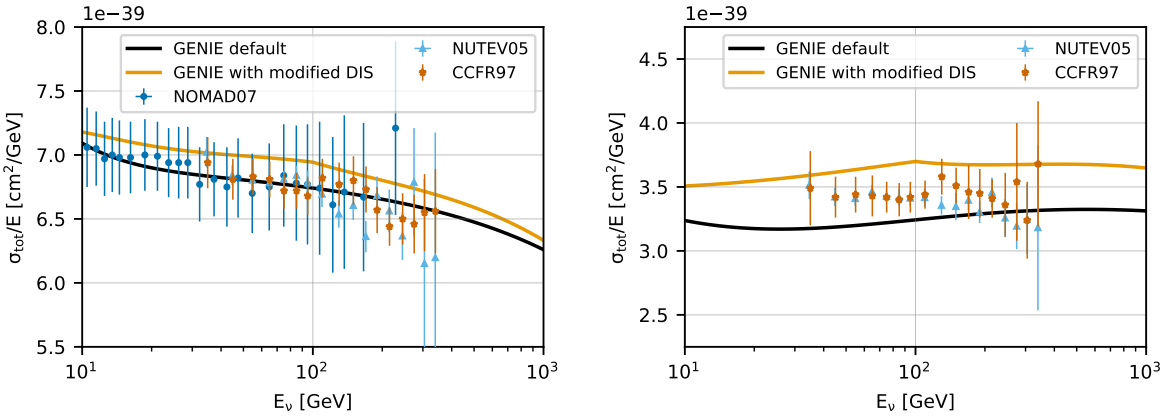

Figure 5.8: Inclusive total neutrino-nucleon cross-sections on an isoscalar target (black) for neutrinos (left) and antineutrinos (right) calculated with GENIE, comparing to measurements from NOMAD [140], NUTEV [141], and CCFR [142]. The scaled GENIE cross-section (orange) is also shown. Taken from [115].

guarantee continuity, the scaling is extrapolated linearly below 100 GeV. The parameter is designed such that a value of 0.0 corresponds to the GENIE cross-sections and a value of 1.0 gives an approximation of the CSMS cross-sections. A comparison of the total cross-sections GENIE (scaled/unscaled) with the data is shown in Figure 5.8.

5.4.3 Detector Calibration Uncertainties

The detection process of neutrinos in IceCube has several sources of uncertainties, where the effects of the properties of the ice itself and the optical efficiency of the DOMs are dominant for this analysis. None of these uncertainties can be described by an analytic expression, so they have to be estimated using MC simulation. This is done by producing additional systematic simulation samples at discrete values of those parameters. The five relevant uncertainty parameters are the absolute efficiency of the DOMs, a global scaling of bulk ice scattering and absorption lengths, and variations of the relative angular acceptance due to hole ice variations in two parameters. To perform the fit, continuous variations with respect to these parameters, will be derived with a method explained in Section 7.2.3.

DOM efficiency: As was already mentioned in Section 3.1.1, the absolute efficiency of the DOMs, ϵ_{DOM} is calibrated using minimum ionizing muons from air showers, due to the lack of a calibrated light source in the detector. Using the muons as a steady, controlled source of light, the efficiency can be estimated by comparing simulated muon data sets with varied DOM response to the measured data. Since the uncertainties found in multiple iterations of this study [85, 86] are at the order of 10 %, this systematic is highly relevant and has to be included in the analysis.

Bulk ice scattering and absorption: Absorption and scattering length are the most important properties that govern the propagation of photons through the ice. The simulation principle and how the depth dependent absorption and scattering coefficients are used was already explained in Section 5.1.1. To account for uncertainties on this model of the bulk ice

[85]: Feintzeig (2014), "Searches for Point-like Sources of Astrophysical Neutrinos with the IceCube Neutrino Observatory"
[86]: Kulacz (2019), "In Situ Measurement of the IceCube DOM Efficiency Factor Using Atmospheric Minimum Ionizing Muons"

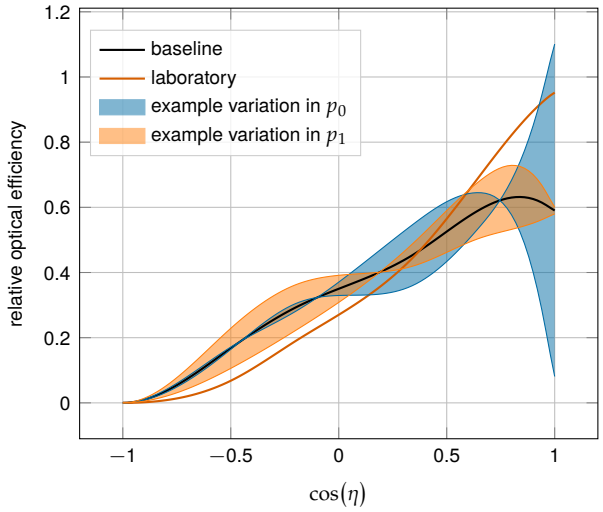

Figure 5.9: Relative angular acceptance modification due to hole ice. Shown is the current baseline model, the variations from changing p_0 and p_1, and a laboratory measurement. Modified from [19].

coefficients, a global scaling for each of the two parameters (global absoprtion, global scatteriong) is applied.

Hole ice angular acceptance: Due to bubble formation in the re-freezing process of the boreholes, the hole ice seems to be less transparent in the center of the columns [143]. This effectively decreases the chance of photons hitting the DOMs directly from below, which can be described as an additional angular modification of the DOM acceptance. The modification is parameterized by a two dimensional, normalized[6] function, where the two dominant of the parameters (p_0, p_1), dictating its form, are enough to describe all past and the current hole ice models from both *in-situ* and laboratory measurements. Figure 5.9 shows the acceptance modification as a function of the incident photon angle $\cos(\eta)$. The current baseline model, the variations achieved through modifying p_0 and p_1, and a laboratory measurement can be seen.

[143]: Rongen, Martin (2016), "Measuring the optical properties of IceCube drill holes"

6: The hole ice angular acceptance modification is normalized so that it does not affect the total charge.

Ice Model: The ice model used in IceCube is continuously improved, and the recent models incorporate the birefringent polycriystalline microstructure [144] into the bulk ice properties. To account for the uncertainty, due to this un-modeled effect in the ice model used for the simulation production, an additional simulation sample is produced using the newer version of the ice model, that incorporates the *birefringence (BFR)* effect.

[144]: Abbasi et al. (2024), "In situ estimation of ice crystal properties at the South Pole using LED calibration data from the IceCube Neutrino Observatory"

5.4.4 Muon Uncertainties

The muon fraction in the final level selection (see Section 5.3.2) is below 1 %, therefore additional muon systematic uncertainties apart from the spectral index are not implemented, but rather a total muon scaling parameter is added. This total scale is somewhat degenerate with the DOM efficiency, since an increased DOM efficiency leads to better muon rejection. Both the total muon scaling and the muon spectral index have a very small impact on the analysis as will be shown in Section 7.2.3.

cite this? (YELLOW)

Detecting Low Energy Double Cascades

6

6.1 Reconstruction

All existing reconstruction algorithms applied for low energy atmospheric neutrino events mentioned in Section 5.3 are either assuming a single cascade hypothesis or a track and cascade hypothesis, which are the two SM morphologies observable at these energies, as was described in Section 3.3. A HNL being produced and decaying inside the IceCube detector however, will produce two cascade like light depositions. The morphology, spatial separation between the cascades, and their individual properties depend on the model parameters discussed in Section 2.3.4. To investigate the performance of the detector to observe and identify these events, a low energy double cascade reconstruction algorithm was developed. It is based on a pre-existing algorithm used to search for double cascades produced from high energy astrophysical tau neutrinos [145] that was established in [146], but first mentioned in [147].

[145]: Abbasi et al. (2020), "Measurement of Astrophysical Tau Neutrinos in IceCube's High-Energy Starting Events"

[146]: Usner (2018), "Search for Astrophysical Tau-Neutrinos in Six Years of High-Energy Starting Events in the IceCube Detector"

[147]: Hallen (2013), "On the Measurement of High-Energy Tau Neutrinos with IceCube"

6.1.1 Table-Based Minimum Likelihood Algorithms

The aforementioned reconstruction is relying on a minimum likelihood algorithm, which is the *classical* approach to IceCube event reconstructions, as opposed to ML based methods. It compares the observed light depositions in the detector to the expected light depositions from a given event hypothesis, where the event hypothesis can be constructed from building blocks of single cascade and track segment expectations. Varying the energies of the track segments and cascade components, will change the expected light and can be used to find the best fit to the observed light. A Poissonian likelihood is constructed, which compares the observed photon numbers, n, with their arrival times to the expected light depositions, μ, for a given even hypothesis as

$$\ln(L) = \sum_j \sum_t n_{j,t} \cdot \ln\big(\mu_{j,t}(\Theta) + \rho_{j,t}\big) - (\mu_{j,t}(\Theta) + \rho_{j,t}) - \ln\big(n_{j,t}!\big) \ , \quad (6.1)$$

where ρ are the number of expected photons from noise, Θ are the parameters governing the source hypothesis, and the likelihood is calculated summing over all DOMs j splitting observed photons into time bins t. The light expectations are calculated using look-up tables [102] that contain the results from MC simulations of cascade events or track segments. By varying the parameters defining the event hypothesis, the likelihood of describing the observed light pattern by the expected light depositions is minimized to find the reconstructed event. Algorithms of this kind used in IceCube are described in great detail in [84]. For the table production a specific choice of ice model has to be made, while the calibrated DOM information is taken from the measurement itself.

[102]: Whitehorn et al. (2013), "Penalized splines for smooth representation of high-dimensional Monte Carlo datasets"

[84]: Aartsen et al. (2014), "Energy Reconstruction Methods in the IceCube Neutrino Telescope"

Based on the tabulated light expectations for cascades and track segments, various event hypothesis can be constructed, like the common cascade only

or the track and cascade hypotheses. The hypothesis describing the double cascade signature of the HNL is using two cascades that are separated by a certain distance. The whole hypothesis is defined by 9 parameters and assumes that the two cascades are aligned with each other, which is a safe assumption for strongly forward boosted interactions. The parameters are the position of the first cascade, x, y, z, the direction of both cascades, ϕ, θ, and its time, t, as well as the decay length, L, between the two cascades. Assuming the speed of the HNL to be the speed of light, c, this already defines the full hypothesis, because the time and position of the second cascade are then fully determined by properties of the first cascade and the decay length. Note here, that the HNL particle does not produce any light while traveling, as it is electrically neutral. Since the likelihood only sums over DOMs that have observed photons, the non-observation of light is used as information and will exclude hypotheses with light expectation in those DOMs. The full 9 parameters describing the event are $\Theta = (x, y, z, t, \theta, \phi, E_0, E_1, L)$. To compute the full likelihood, the term in Equation 6.1 defined for a single event hypothesis, is summed over both cascade contributions, as $\sum_i \ln(L_i)$, with i being the cascade index.

Elaborate whether this is the case (show it in a plot?). Discuss directionality of cascades in general. (ORANGE)

6.1.2 Optimization for Low Energies

Optimizing the double cascade reconstruction for low energy events was done in parallel to the development of the model dependent simulation generator introduced in Section 4.2. A preliminary sample of HNL events from the model dependent simulation was used, containing a continuum of masses between 0.1 GeV and 1.0 GeV and lab frame decay lengths sampled uniformly in the range from 5 m to 500 m. Even though this sample is not representative of a physically correct model and therefore not useful to predict the event expectation, it can still be used to optimize the reconstruction. The double cascade nature of the individual events and the evenly spaced decay length distribution are especially useful for this purpose.

The simulation is processed up to Level 5 of the selection chain described in Section 5.2.2 and one of the reconstructions from [128] is applied to the events, fitting a cascade and a track and cascade hypothesis. The results from this reconstruction are used as an input for the double cascade reconstruction, where the position of the vertex, the direction of the event, and its interaction time are used as the input quantities for the first cascade, and the length of the track reconstruction is used as a seed for the distance between the two cascades.

[128]: Abbasi et al. (2022), "Low energy event reconstruction in IceCube DeepCore"

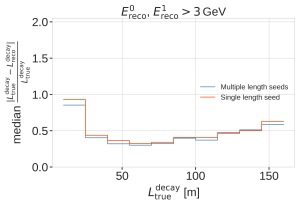

Figure 6.1: Decay length resolution as a function of the true decay length, comparing the same fit routine seeded with just the seed decay length and seeded with a decay length of 5 m, 25 m, 50 m, 100 m, and 200 m on the left. Only events that had more than 3 GeV in both cascades are used, and the resolutions are unweighted.

Decay Length Seeds

The full 9 dimensional likelihood space is very complex and can have many local minima, depending on the specific event and its location in the detector. Especially the seed value of the length between the two cascades was found to have a very strong impact on whether the global minimum was found during the minimization. To mitigate this effect, multiple fits are performed, seeding with variations of the input length at different orders of magnitude. The best result is used, selected based on the total likelihood value of the best fit parameter set. A small improvement in the decay length resolution can be found by using this approach as compared to a single length seed. The effect can be seen in Figure 6.1, which shows the median of the absolute,

Remake with better dimensions, so it fits in the margin, remove or make better title corresponding to the subsubsection titles (RED)

fractional error with respect to the true decay length, as a function of the true decay length for a single length seed and multiple length seeds. Only events that have both reconstructed cascade energies above 3 GeV are used for this comparison, where this threshold was roughly chosen to select well reconstructed double cascade events.

Fit Routine

Because the length seed showed to have such a large impact on the reconstruction performance, a more sophisticated fit routine than fitting all 9 parameters at once was tested. In a first fit iteration, some parameters are fixed and the resulting best fit point is used to fit all 9 parameters in a second iteration. In Figure 6.2 it can be seen how a fit split into two consecutive steps, where the first step fits only both cascade energies and the decay length and the second step fits the full 9 parameters, performs better as compared to a single, full 9 parameter fit. The initial seed remains identical for both the routines.

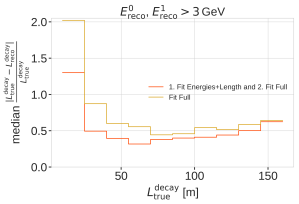

Figure 6.2: Decay length resolution as a function of the true decay length, comparing a full 9 parameters fit to an iterative approach where first the energies and the decay length are fit, while fixing the other 7 parameters and then the full fit is performed. Only events that had more than 3 GeV in both cascades are used, and the resolutions are unweighted.

Remake with better dimensions, so it fits in the margin, remove or make better title corresponding to the subsubsection titles (RED)

Minimizer Settings

To investigate the effect of the minimizer used to find the best fit parameters, the reconstruction was performed using three different minimizers, which were easily accessible within the reconstruction framework. The minimizers used were Minuit1 Simplex, Minuit2 Simplex, and Minuit2 Migrad. The initial idea was to test a global minimizer, or a routine that can find the rough position of the global minimum first and then a local minimizer to find the exact minimum, but unfortunately this was not possible with the minimizers available in the framework. As can be seen in Figure 6.3, Minuit1 Simplex performed best and was chosen as the default for the reconstruction.

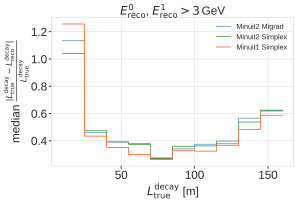

Figure 6.3: Decay length resolution as a function of the true decay length, comparing the same fit routine performed with different minimizers. Only events that had more than 3 GeV in both cascades are used, and the resolutions are unweighted.

Remake with better dimensions, so it fits in the margin, remove or make better title corresponding to the subsubsection titles (RED)

6.1.3 Performance

The chosen reconstruction chain used to test the performance of the detector to observe low energy double cascades is the following; Minuit1 Simplex is used as the minimizer, the decay length is seeded with 3 different values, 0.5x, 1.0x, and 1.5x the length of the preceding track reconstruction, and the fit routine is split into two steps, where the first step fits the energies and the decay length and the second step fits the full 9 parameters. In the first step, the number of time bins in Equation 6.1 is set to 1, so just the number of photons and their spatial information is used. The second step is seeded with the best results from the first step, and here the number of time bins is chosen such that each photon falls into a separate time bin, which means all time information is used. The average runtime per event is ~16 s on a single CPU core, but is very dependent on the number of photons observed in the event, since the likelihood calculation in the second step scales with this number and a table lookup has to be performed for each photon.

To get a more realistic estimate of the reconstruction performance, it is run on a second preliminary sample of HNL events from the model dependent simulation, containing masses between 0.1 GeV and 3.0 GeV and the lab frame decay length is sampled from an inverse distribution in the range from 1 m to 1000 m, which is a better approximation of the expected exponential

cite these buggers again, and or point back to where they were mentioned? (RED)

decay distribution of the HNL. The performance is shown for events where the reconstruction chain was successfully run, the event selection criteria up to the final selection level of low energy analyses are fulfilled, and the reconstructed energy of both cascades is above 3 GeV.

Energy Resolutions

The energy resolution is inspected by looking at the two-dimensional distribution of reconstructed energy versus the true energy as shown in Figure 6.4. The bin entries are shown as well as the median and ±25 % calculated per vertical column, to get an idea of the distribution for a given energy slice. The color scale is showing the PDF along each true energy slice, which is the full information highlighted by the median ±25 % quantile lines. The reconstructed energy is only the energy that is observable from photons, while the true energy is the total cascade energy, including the parts that go into EM neutral particles that do not produce light. It is therefore expected that the reconstructed energy is lower than the true and the median therefore does not line up with the axis diagonal.

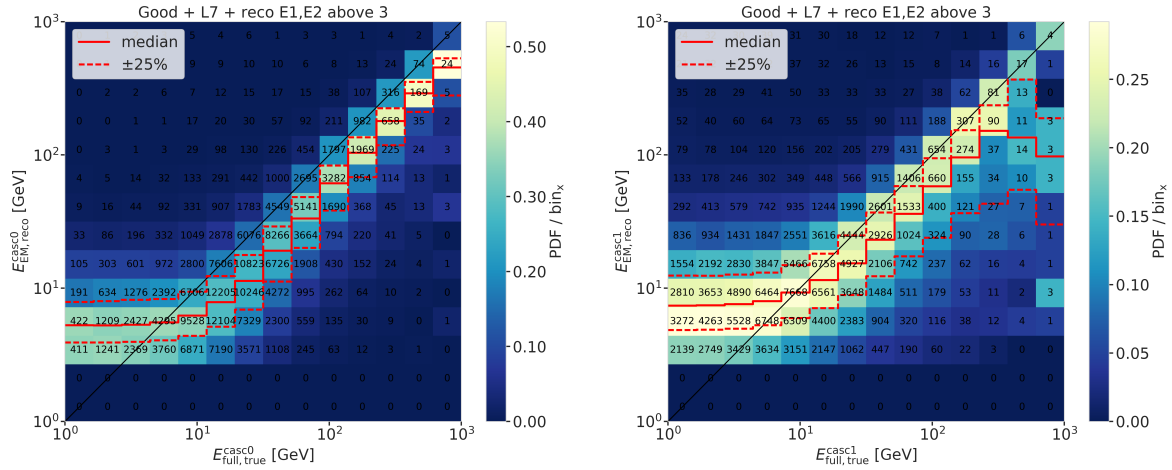

Figure 6.4: Reconstructed (EM) energy versus true energy (full) energy for the first cascade (left) and second cascade (right). The color scale is according to the PDF in each vertical true energy slice, with the solid and dashed lines showing the median ±25 % quantiles. The bin entries are shown as numbers.

The histogram for the first cascade energy is shown on the left and above an energy of ~10 GeV the reconstruction performs well, with the median being parallel to the diagonal and the spread being small. Below this energy the reconstruction is over-estimating the true energy , because events that enter the sample are events with an over fluctuation in their light deposition, which makes them pass into the selection and being reconstructible in the first place.

For the second cascade the overall behavior is similar, only that the energy where the reconstruction starts to perform well is higher around ~20 GeV. The spread around the median is also larger and starts to expand a lot above 200 GeV, where the statistics are lower as can be seen from the bin counts. It is also very apparent that the majority of events have a lower true energy in the second cascade, peaking between 1 GeV and 20 GeV. This can be seen by the indicated bin counts in the right part of Figure 6.4.

For both cascade resolutions the effect of the reconstruction being biased towards lower values can be seen. This is due to the comparison of the full true energy to the reconstructed EM energy as mentioned before.

Length Resolutions

The decay length resolution is also investigated by looking at the two-dimensional histogram, where the reconstructed decay length is plotted versus the true decay length. The left part of Figure 6.5 shows the distributions after the same selection criteria from Section 6.1.3 are applied. It can be observed that for short true lengths the reconstruction is over-estimating the length, while for long true lengths the reconstruction is strongly under-estimating the length. There is a region between true lengths of 20 m and 80 m where the median reconstruction is almost unbiased, but the 50 % interquartile range is large and increasing from ~50 m to ~70 m with true decay lengths.

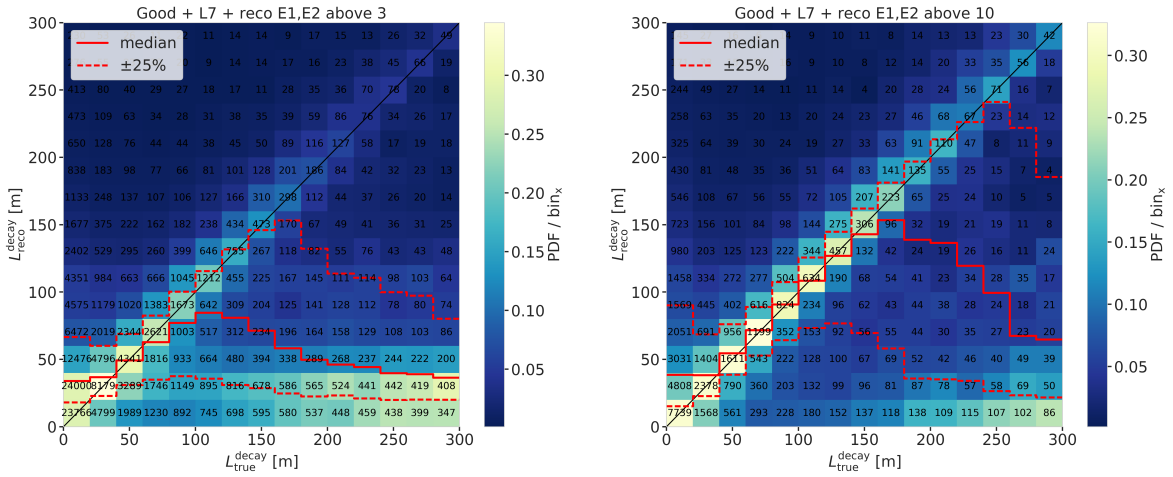

Figure 6.5: Reconstructed decay length versus true decay length for ~3 GeV (left) and ~10 GeV (right) minimum reconstructed cascade energies. The color scale is according to the PDF in each vertical true length slice, with the solid and dashed lines showing the median ±25 % quantiles. The bin entries are shown as numbers.

blow up figures to make better visible? (ORANGE)

The over-estimation at small true lengths can be explained by multiple factors, one being that the shortest DOM spacing is ~7 m, vertically for DeepCore strings, but mostly larger than that, so resolving lengths below this is very complicated, and the reconstruction tends to be biased towards estimating the length around where the light was observed. Additionally, approaching a length of 0.0, the reconstructed length will of course always be a one-sided distribution, because the lengths have to be positive.

The under-estimation at large true lengths is more puzzling, and it seems like the distribution becomes bimodal in the reconstructed lengths, with one population around the diagonal, meaning that they are properly reconstructed, and another population at very short reconstructed lengths, which are badly reconstructed. Above 150 m the badly reconstructed population starts to dominate, and the median resolution drops off strongly. The assumption is that for these events, only one cascade was observed with enough light to be reconstructed, and the reconstruction describes the one observed cascade in two parts, separated by a short distance, driven by similar factors as mentioned before. A quick check to confirm whether this

is the case, was to increase the selection criteria to minimum reconstructed cascade energies of 10 GeV, which is shown in the right part of Figure 6.5. It can be seen that the median resolution is already much better, aligning with the expectation between 40 m and 160 m. Judging from the median resolution and the spread in this range, there are very few events with an over-expectation in the energy, since both of them are aligning with the diagonal. Towards lower reconstructed lengths on the other hand, the spread is still very large, and above 200 m the badly reconstructed population starts to dominate again.

Badly Reconstructed Cascade Population

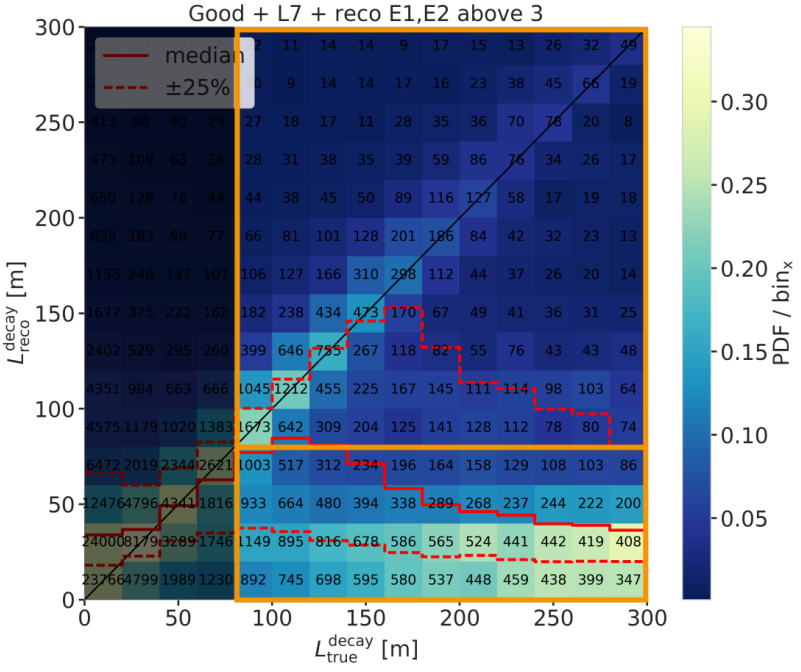

Figure 4.6 remake plot: no bin counts, blow up labels etc. margin possible? (RED)

fix caption (RED)

To investigate the badly reconstructed population further, a rough separation was made to find out what the cause of the difference is. It was already established that a larger reconstructed energy in both cascades, which is related to a larger true energy in form of more deposited light, leads to a better reconstruction in more events. To select the two populations, only events with true decay length larger than 80 m are used as shown in Figure 6.6, and the populations are split by the reconstructed decay length being larger or smaller than 80 m. To investigate the difference between the two populations, several variables were compared to find the reason(s) for the bad reconstruction.

The left part of Figure 6.7 shows the true horizontal distance of the second cascade from string 36. The distance is denoted as ρ_{36} and is a very good proxy for the distance to the center of the detector, because string 36 is almost at the center. While the distributions looks very similar for the first cascade (not shown), for the second cascade the badly reconstructed population extends to larger values. Considering that the DeepCore strings are roughly inside a 70 m radius from the center, and the next layer of IceCube strings is at a radius of 125 m, this is a plausible explanation for a worse reconstruction,

because for the badly reconstructed population the second cascades are more often in regions without DOMs, so less or no light is observed from them.

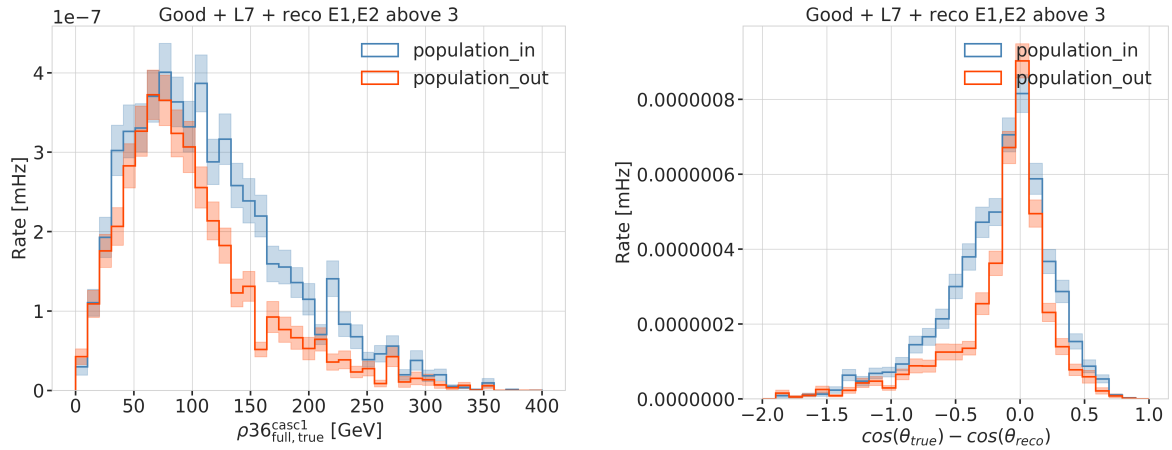

Figure 6.7

re-make normalized? (ORANGE)

fix caption (RED)

Another possible reason why the reconstruction underperforms could be that the initial seed direction itself was off and therefore one of the cascades cannot be found properly. Looking at the error of the cosine of the reconstructed zenith angle shown in the right of Figure 6.7, we see that the badly reconstructed population has a larger error, and is less peaked around 0.0. This could be a hint that the direction is worse for the badly reconstructed population, which could be due to a bad seed direction, or just the result of one cascade not depositing enough light to be observed.

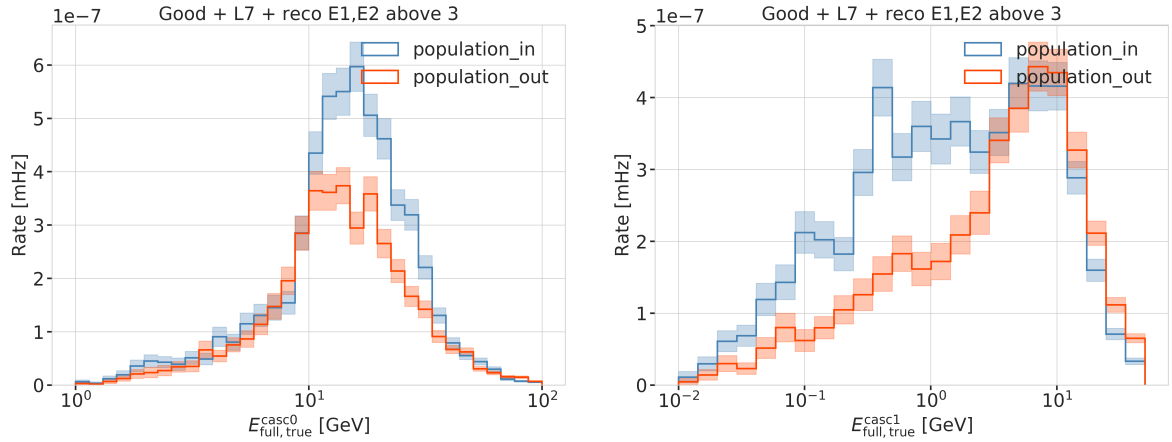

Figure 6.8

re-make normalized? (ORANGE)

fix caption (RED)

The true energies of both cascades are shown in Figure 6.8, where it can be observed that the first cascade energy is generally much larger than the second, peaking between 10 GeV and 20 GeV, while the second cascade peaks below 10 GeV. For the first cascade there is no significant difference between the two populations, but for the second cascade the badly reconstructed population has a larger fraction of events with lower energies and the distribution is almost uniform in the range of 2 GeV to 10 GeV, while the well reconstructed population has a peak around 10 GeV and falls off faster

towards lower energies. This is a strong indication that the main reason for the bad reconstruction is the low energy of the second cascade.

6.2 Double Cascade Classification

Even though the performance results show that it is very complicated to reconstruct these low energy double cascade events, the attempt to identify them in the background of SM neutrino events was made. For this purpose a classifier was trained to distinguish between HNL *signal* events and SM neutrino *background* events, using the same preliminary sample of HNL events as was used to assess the reconstruction performance. To mitigate the effect of the bad reconstruction, a set of cuts was applied to make sure the classifier is trained on well reconstructed events. The cuts are a minimum reconstructed energy of both cascades of 5 GeV and a minimum reconstructed decay length of 40 m. and they are applied to both signal and background events.

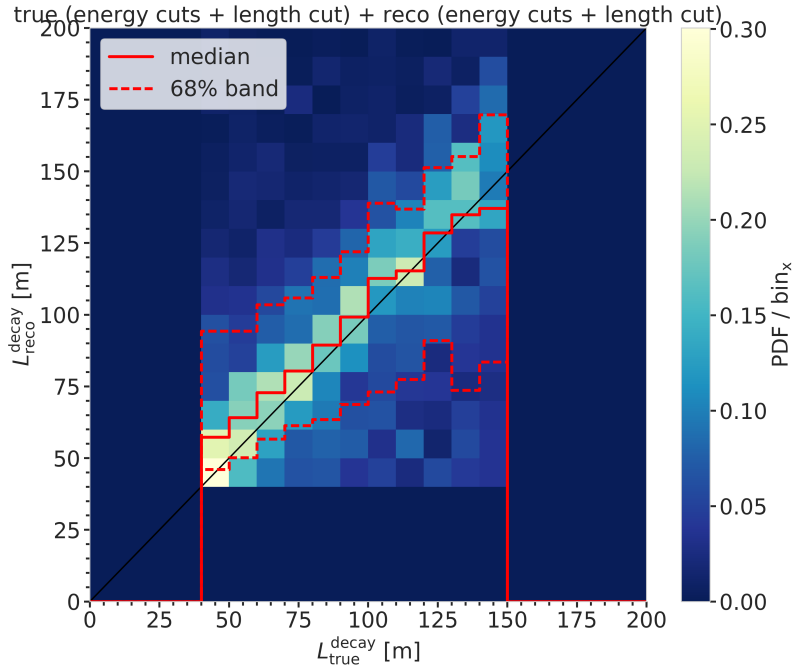

Figure 6.9 fix caption (RED)

Additionally, some cuts on the true energies and decay length were applied for the signal, which are a minimum true energy of both cascades of 5 GeV, and a true decay length between 40 m and 150 m. These were chosen to make sure the HNL events were theoretically double cascade like and at a sensible length scale inside DeepCore. Figure 6.9 shows the decay length two-dimensional histogram after the cuts were applied.

add table with cuts? (YELLOW)

The classifier used was a *Boosted Decision Tree (BDT)* from the *scikit-learn (sklearn)* package [148] and the input features are taken from the double cascade reconstruction explained in Section 6.1 as well as some additional variables from earlier levels of the processing explained in Section 5.2. Figure 6.10 shows the distributions of two example input features, where the left plot shows the output probability of the classifier trained to distinguish track from cascade like events, which is used in the oscillation analysis,

[148]: Pedregosa et al. (2011), "Scikit-learn: Machine Learning in Python"

and the right plot shows the reconstructed decay length from the double cascade reconstruction. Shown are the distributions for the the HNL signal, the individual background components, and the total background.

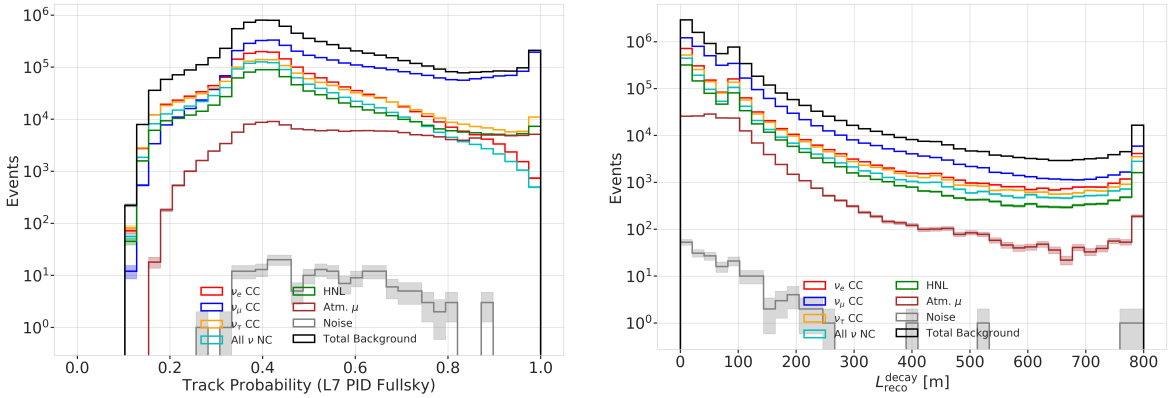

Figure 6.10

fix caption of this figure (RED)

A single classifier and a combination of two classifiers were tested. The single classifier was trained to distinguish between HNL signal events and all SM background events at once. The two classifiers were trained separately, one to distinguish signal from track like background, and the other to distinguish signal from cascade like background. Since the SM neutrino events at these energies are either track like or cascade like, the latter approach was expected to perform better. Despite the fact that several combinations of features and classifier hyperparameters were tested, it was not possible to identify a pure double cascade region with a single classifier.

By applying the two classifiers trained to distinguish signal from track and signal from cascade, it is possible to select a region with only signal events. This is visualized in Figure 6.11, where the probabilities of 1 implies very signal like, and only the regions close to 1 are shown for both outputs, to highlight the interesting region, where a pure HNL sub-sample can be selected. When physical weights are applied to those signal events however, the expected event rate is very low, and even by assuming a highly optimistic mixing of 1, it would take more than 20 years of data taking to observe a single event. Additionally, with this low simulation statistics the prediction is not very reliable, either. Making a weaker cut to select a signal like region will contain a large amount of background events, which dominate over the signal at $\sim$ 2 orders of magnitude for a mixing of 0.1. The conclusion from this is, that with the current selection and reconstruction chain and a classical BDT, it is not possible to distinguish signal events at a level feasible to perform an analysis.

Make a single plot, showing S/B or so? (RED)

fix caption of this figure (RED)

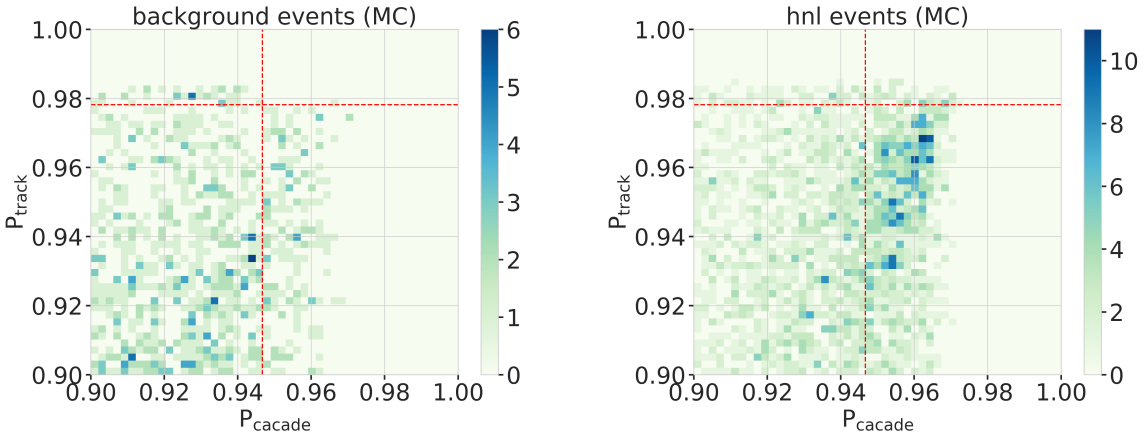

Figure 6.11

6.3 Generalized Double Cascade Performance

All the above results were obtained using preliminary development versions of the model dependent HNL simulation. To investigate the effect of the low energy event selection and the double cascade reconstruction performance in a more generic way, the model independent simulation introduced in Section 4.1 is used to repeat the performance checks and to run a series of additional checks. The important advantage of the model independent samples is the controllable parameter space, especially in cascade energies and decay length, because the event kinematics are not coupled to the underlying HNL model, but can be chosen freely. This means that some benchmark edge cases can be investigated, and the performance can also be assessed for a realistic scenario in addition to mapping out the effects of the event selection and where the reconstruction breaks down.

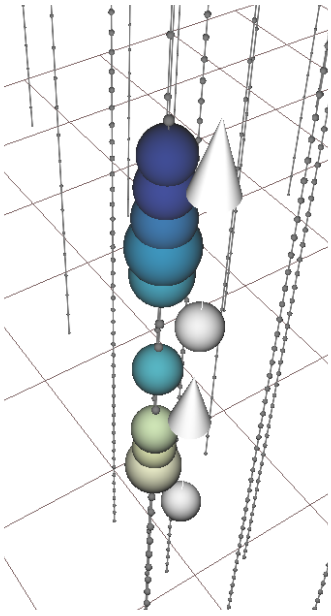

Figure 6.12: Event view of an idealistic double cascade event, with cascade energies of 2.4 GeV and 4.9 GeV, and a decay length of 65.8 m. The colored spheres show the DOMs that have observed light, where the size is proportional to the number of observed photons and the color indicates the time (yellow is early, blue is late). The strings are shown as black lines, with small spheres indicating the DOM positions, and the true cascade vertices and directions are shown as white spheres with white arrows.

fix caption of this figure (RED)

6.3.1 Idealistic Events

The *best case* scenario to observe an event is to be directly on top of a string with a straight up-going direction. Using the simulation sample introduced in Section 4.1.1 and running the double cascade reconstruction from Section 6.1 on these events, it is possible to estimate the performance limit of the reconstruction. Figure 6.12 shows one example event view from that sample, where the cascade energies are 2.4 GeV and 4.9 GeV, and the decay length is 144.5 m. It can be seen that despite the low energies, both cascades deposit light in the DOMs and the reconstruction is expected to work.

The performance of the length reconstruction is shown in Figure 6.13, where the median of the absolute, fractional decay length resolution is shown on the left and the two-dimensional histogram of the reconstructed versus the true decay length is shown on the right. For these results and the following, all events that were reconstructed with non-zero cascade energies and non-zero decay length are used, and the events are unweighted. The length is very well reconstructed, with the median resolution being below 30 % above a true decay length of ~10 m, and falling off with increasing true length, down to ~10 % at 100 m.

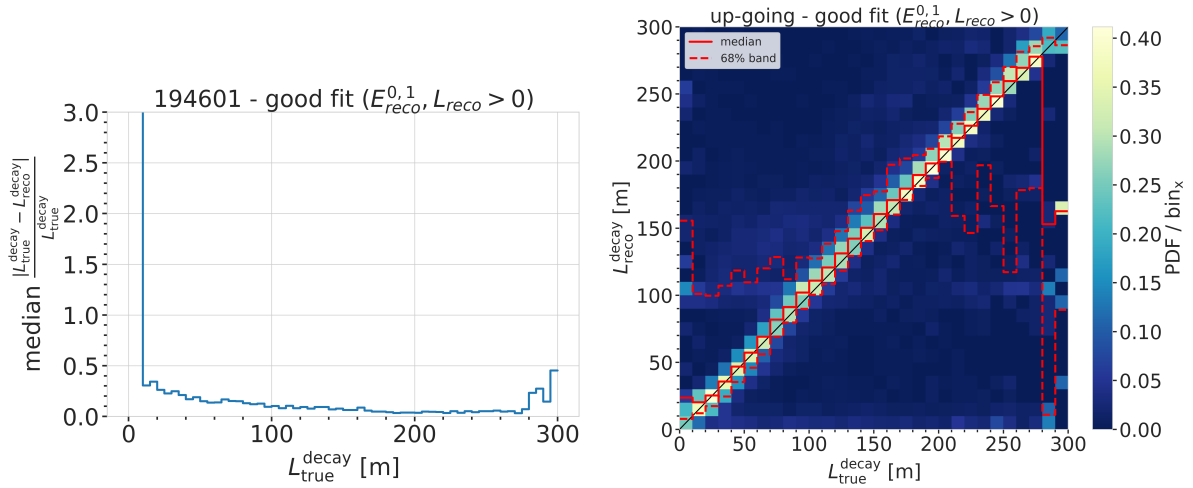

Figure 6.13

The two-dimensional histogram shows that there is no under-estimation of the length up to a true decay length of ~210 m, which shows that if there are DOMs in the region between the two cascades that have not observed any light, the reconstruction is very stable. Considering the underlying Poisson likelihood in Equation 6.1 used for the reconstruction, this makes sense, since DOMs being present, but not observing any light is affecting the light expectation that goes into the likelihood and therefore makes these hypotheses unlikely and therefore incompatible with the data.

6.3.2 Realistic Events

The sample of HNL events introduced in Section 4.1.2, which is a more realistic representation of the expected HNL events, but still offers more controlled energy and length distributions, is used to investigate the selection efficiency, to cross check the reconstruction performance, and to benchmark the limits where the reconstruction breaks down. An example event view is shown in Figure 6.14, for cascade energies of 30.8 GeV and 25.3 GeV, and a decay length of 144.5 m. Since the size of the colored spheres is proportional to the number of photons observed in the DOMs, it can be seen from the event view that even for these higher energies, only individual or few photons are observed. This makes detecting and reconstructing them significantly more challenging and is purely due to the larger distance of the cascades from the DOMs.

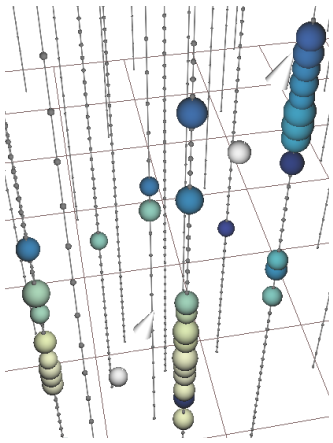

Figure 6.14: Event view of a realistic double cascade event, with cascade energies of 30.8 GeV and 25.3 GeV, and a decay length of 144.5 m. The colored spheres show the DOMs that have observed light, where the size is proportional to the number of observed photons and the color indicates the time (yellow is early, blue is late). The strings are shown as black lines, with small spheres indicating the DOM positions, and the true cascade vertices and directions are shown as white spheres with white arrows.

To assess the efficiency of the low energy event selection introduced in Section 5.2, the energy and length distributions are shown across the different selection levels in Figure **??**. Table **??** shows the total efficiency of the selection, where it can be seen that at level xx it is reduced the most and only xx% of the events pass the selection to level 5.

Make/add relevant plots here (RED)

Plot energy (true total) and true decay length across the different levels (RED)

Make table with the rates across the different levels for benchmark mass/mixing (RED)

The energy distributions in Figure 6.15 show a similar behavior to the results discussed in Section 6.1.3. The difference is that now, there is no bias in the reconstructed energy, because the events are simulated as EM cascades, which means all energy is deposited in light and can be reconstructed. Above around 5 GeV to 6 GeV the median is very stable, and the 1-sigma resolution band is 50 % narrow and decreasing with energy down to 20 % at 100 GeV.

Interestingly, the second cascade energy reconstruction performs slightly worse, although they have the same energy ranges for this sample. This could hint at an asymmetry in the reconstruction process, which might relate to how the two cascades are parameterized, or be due to the different positions and the dominantly up-going direction used in the sampling combined with the DOMs looking down. The total energy resolution shown in the left part of Figure 6.16 is very good, above 10 GeV it is unbiased and the 1-sigma resolution band is below 20 %.

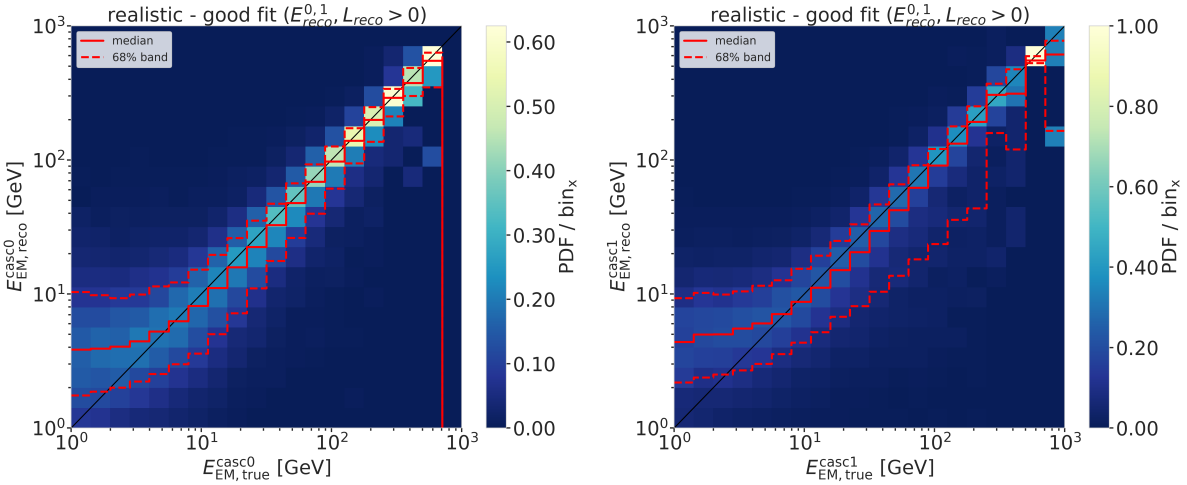

Figure 6.15
fix caption of this figure (RED)

The decay length resolution shown in the right part of Figure 6.16 looks similarly bad to the results discussed in Section 6.1.3 and shows the same features with a region between 20 m and 80 m where it is roughly unbiased, but the 1-sigma resolution band is wide with a lot of outliers towards short reconstructed lengths. Below 65.8 m the reconstructed lengths are always over-estimating the true and above 80 m a population of events start to dominate where the decay lengths is not getting reconstructed at all, as investigated before.

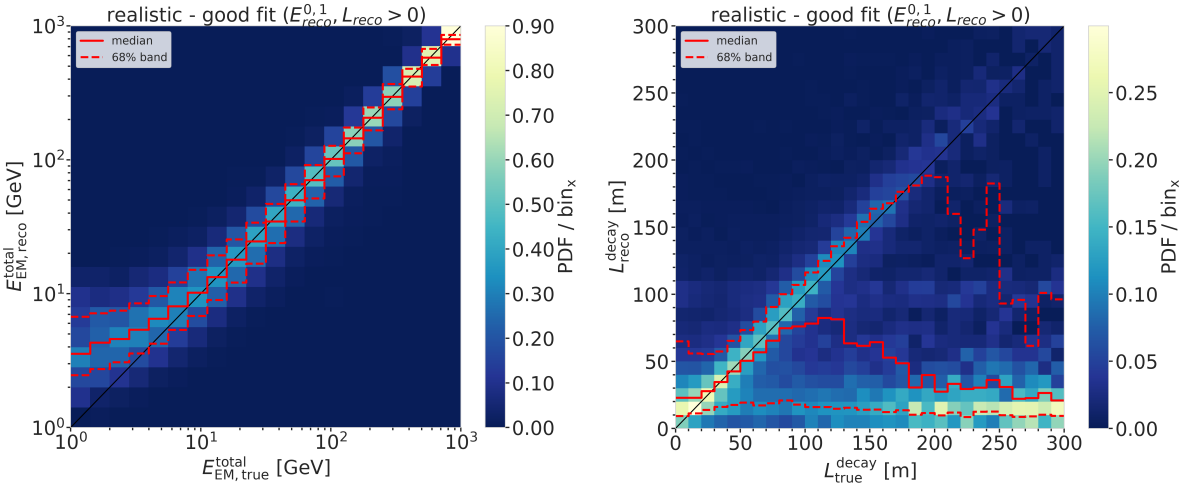

Figure 6.16
fix caption of this figure (RED)

To get an estimate of what minimum energies are necessary for the reconstruction to perform reasonably well, the fractional decay length resolution

is shown as a function of the total true energy and the minimum energy of both individual cascades in Figure 6.17. In the left part it can be seen that the median of the decay length resolution stabilizes around 0 for a total energy above 20 GeV, but the spread of the distribution is still quite large with a 1-sigma band of 80 % to 100 %, decreasing down to ~60 % at 100 GeV. Based on the right part of the figure, the decay length resolution starts to be unbiased for a minimum energy of any cascade of 7 GeV, with an equivalently large spread. A rough takeaway from this is that the decay length reconstruction is not reliable for events with one cascade energy below 7 GeV and with a total energy below 20 GeV. Above these values the median resolution is roughly unbiased, but the spread is still large, decreasing with increasing energy.

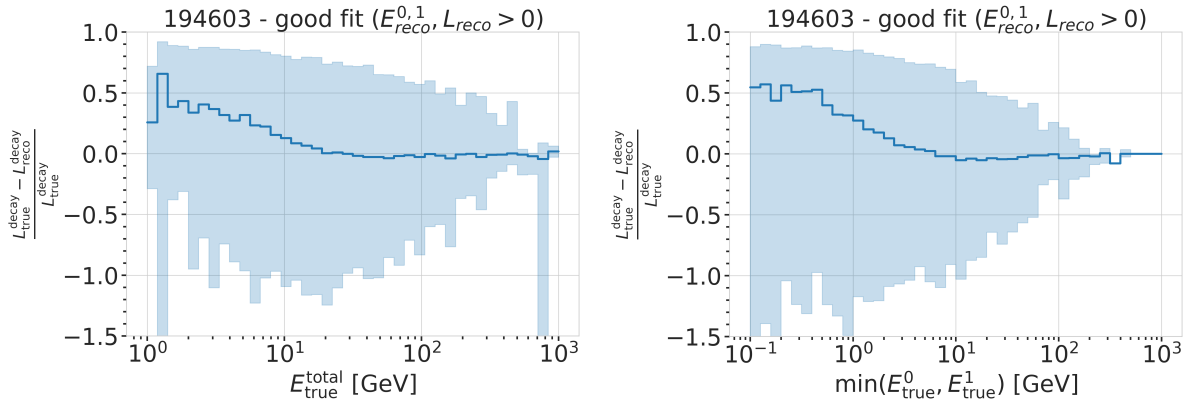

Figure 6.17

fix caption of this figure (RED)

6.4 Summary and Outlook

write summary and outlook (RED)

From the investigation of the good and badly reconstructed events, it can be concluded that the main reason for the bad reconstruction is the low energy of the second cascade. Despite the fact that the split into the two populations was very rudimentary, it is clear that this is the dominant cause, while other factors, like the position of the second cascade, or the potentially bad input seed direction are also contributing. For a thorough investigation, a more sophisticated separation would be needed.

- upgrade? - other selection? - other reconstruction?

Search for Tau Neutrino Induced Heavy Neutral Lepton Events

7

This chapter describes the search for HNL events using 10 years of IceCube DeepCore data. The expected number of HNL events in the data sample depends on the mass of the additional heavy state, m_4, and the mixing element $|U^2_{\alpha 4}|$, with $\alpha = e, \mu, \tau$, between the SM flavors and the new mass state. As discussed in Section 2.3, this work focuses on the mixing to the tau sector, $|U^2_{\tau 4}|$, which has the weakest constraints to date. Since the mass itself influences the production and decay kinematics of the event and the accessible decay modes, individual mass samples were produced as described in Section 4.2. The mass influences the decay length and energy distributions, while the mixing both changes the overall expected rate of the HNL events and the shape in energy and length. We perform three independent searches for each mass sample, where the mixing is measured in each of the fits.

7.1 Final Level Sample

The final level simulation sample of this analysis consists of the neutrino and muon MC introduced in Section 4.3 and one of the three HNL samples explained in Section 4.2, while the data are the events measured in 10 years of IceCube DeepCore data taking. All simulation and the data are processed through the full event selection chain described in Section 5.2 and Section 5.3 leading to the final level sample. As described in Section 5.3.2, event triggers consisting purely of random coincidences induced by noise in the DOMs have been reduced to a negligible rate, and will not be discussed further.

To get the neutrino expectation, the MC events are weighted according to their generation weight introduced in Section 4.3.1, multiplied by the total lifetime, and the expected neutrino flux. For the correct expectation at the detector, the events have to be weighted by the oscillation probability, depending on their energy and their distance traveled from the atmosphere to the detector. The oscillation probabilities are calculated using a PYTHON implementation of the calculations from [149], which use the matter profile of the Earth following the *Preliminary Reference Earth Model (PREM)* [150] as input. Apart from the energy and the distance, the two relevant parameters defining the oscillation probabilities are the atmospheric neutrino oscillation parameters θ_{23} and Δm^2_{31}. Since the HNL events originate from the tau neutrinos that were produced as muon neutrinos in the atmosphere and then oscillated into ν_τ, this weighting is also applied in addition to the specific weighting scheme for the HNL events described in Section 4.2.3, which itself is defined by the mixing $|U^2_{\tau 4}|$ and the mass m_4.

[149]: Barger et al. (1980), "Matter effects on three-neutrino oscillations"
[150]: Dziewonski et al. (1981), "Preliminary reference Earth model"

7.1.1 Expected Rates/Events

The rates and the expected number of events for the SM background are shown in Table 7.1 with around 175000 total events expected in the 10 years.

Only data marked as good is used for the analysis, where *good* refers to measurement time with the correct physics run configuration and without other known issues. The resulting good detector livetime in this data taking period was 9.28 years. The rates are calculated by summing the weights of all events in the final level sample, while the uncertainties are calculated by taking the square root of the sum of the weights squared. The expected number of events is calculated by multiplying the rate with the livetime. The individual fractions show that this sample is neutrino dominated where the majority of events are ν_μ-CC events.

Table 7.1: Final level rates and event expectation of the SM background particle types.

Type	**Rate** [mHz]	**Events** (9.28 years)	**Fraction** [%]
ν_μ^{CC}	0.3531	103321 ± 113	58.9
ν_e^{CC}	0.1418	41490 ± 69	23.7
ν^{NC}	0.0666	19491 ± 47	11.1
ν_τ^{CC}	0.0345	10094 ± 22	5.8
μ_{atm}	0.0032	936 ± 15	0.5
total	0.5992	175332 ± 143	100.0

Table 7.2 shows the rates and expected number of events for the HNL signal simulation. The expectation depends on the mass and the mixing and shown here are two example mixings for all the three masses that are being tested in this work. A mixing of 0.0 would result in no HNL events at all. It can already be seen that for the smaller mixing of $|U_{\tau 4}|^2 = 10^{-3}$ the expected number of events is very low, while at the larger mixing of $|U_{\tau 4}|^2 = 10^{-1}$ the number is comparable to the amount of atmospheric muons in the background sample.

Table 7.2: Final level rates and event expectations of the HNL signal for all three masses and two example mixing values.

HNL mass	**Rate** [µHz]	**Events (in** 9.28 years)
$\lvert U_{\tau 4}\rvert^2 = 10^{-1}$		
0.3 GeV	3.3	975 ± 2
0.6 GeV	3.1	895 ± 2
1.0 GeV	2.5	731 ± 2
$\lvert U_{\tau 4}\rvert^2 = 10^{-3}$		
0.3 GeV	0.006	1.67 ± 0.01
0.6 GeV	0.022	6.44 ± 0.01
1.0 GeV	0.025	7.27 ± 0.01

7.1.2 Analysis Binning

[129]: Yu et al. (2023), "Recent neutrino oscillation result with the IceCube experiment"

Add fractions of the different particle types in the bins for benchmark mass/mixing (another table?) (ORANGE)

An identical binning to the analysis performed in [129] is used. In total, there are three bins in PID (cascade like, mixed, and track like), 12 bins in reconstructed energy, and 8 bins in cosine of the reconstructed zenith angle as specified in Table 7.3. Extending the binning towards lower energies or

Table 7.3: Three-dimensional binning used in the analysis. All variables are from the FLERCNN reconstruction) explained in Section 5.3.

Variable	N_{bins}	**Edges**	**Spacing**
P_ν	3	[0.00, 0.25, 0.55, 1.00]	linear
E	12	[5.00, 100.00]	logarithmic
$\cos(\theta)$	8	[-1.00, 0.04]	linear

increasing the number of bins in energy or cosine of the zenith angle did not improve the HNL sensitivities significantly, because the dominant signal region is already covered with a sufficiently fine binning to observe the

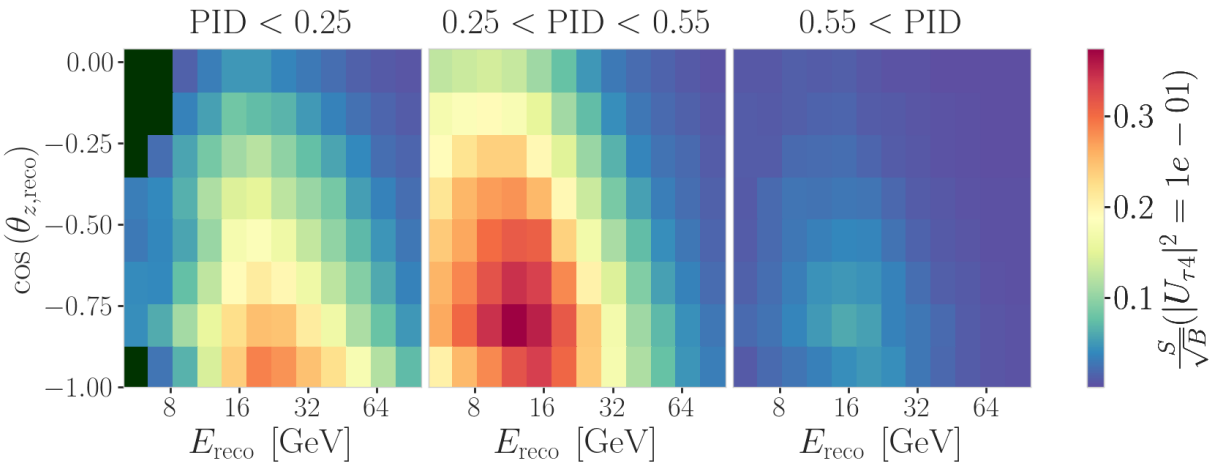

Figure 7.1: Signal over square root of background expectation in 9.28 years for the 1.0 GeV mass sample at a mixing of 0.1, while all other parameters are at their nominal values.

shape and magnitude of the HNL events on top of the SM background. This can be seen in the middle panel of Figure 7.1, which shows the expected signal events divided by the square root of the expected background events for every bin used in the analysis. The signal expectation is using the 1.0 GeV mass sample at a reference mixing of 0.1, with the corresponding three dimensional histogram shown in Figure B.1. Both the nominal background expectation used to calculate the signal to square root of background ratio and the detector data can be seen in Figure 7.2.

Some low energy bins in the cascade like region have very low MC expectations (<1 event) and are therefore not taken into account in the analysis, to prevent unwanted behavior in the fit. Those are shown in dark green in the three dimensional histograms, and both background and data histograms show a strong decrease of events towards low energies in the cascade like bin. This background expectation is not necessarily supposed to agree with the data, because this is the distributions assuming nominal parameter values, before performing the fit to find the parameters that describe the data best. All parameters used in the analysis are discussed in Section 7.2.2, and post-fit data to MC comparisons are shown in Section 7.3.3.

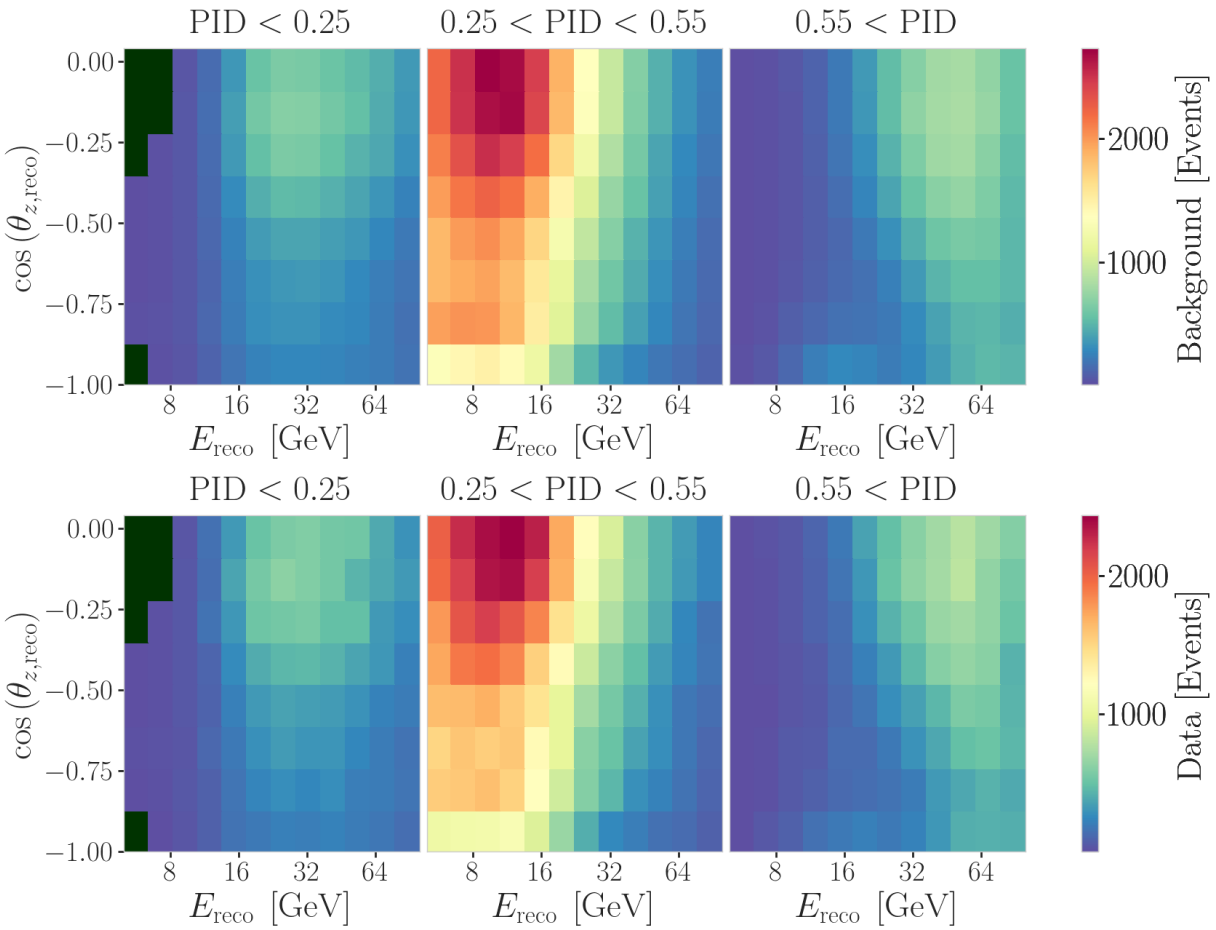

Figure 7.2: Background expectation in 9.28 years for all other parameters are at their nominal values (top) and observed data (bottom).

7.2 Statistical Analysis

7.2.1 Test Statistic

The measurements are performed by comparing the weighted MC to the data. Through variation of the nuisance and physics parameters that govern the weights, the best matching set of parameters can be found, by optimizing a fit metric. The comparison is done using a modified χ^2, defined as

$$\chi^2_{\text{mod}} = \sum_{i \in \text{bins}} \frac{(N_i^{\text{exp}} - N_i^{\text{obs}})^2}{N_i^{\text{exp}} + (\sigma_i^{\nu})^2 + (\sigma_i^{\mu})^2 + (\sigma_i^{\text{HNL}})^2} + \sum_{j \in \text{syst}} \frac{(s_j - \hat{s}_j)^2}{\sigma_{s_j}^2}, \tag{7.1}$$

as the fit metric. It is designed such that taking the difference between a free fit and a fit with fixed parameters based on a chosen hypothesis, $\Delta\chi^2_{\text{mod}}$, can directly be used as a *test statistic (TS)* for hypothesis testing, due to its asymptotic behavior. The total even expectation is $N_i^{\text{exp}} = N_i^{\nu} + N_i^{\mu} + N_i^{\text{HNL}}$, where N_i^{ν}, N_i^{μ}, and N_i^{HNL} are the expected number of events in bin i from neutrinos, atmospheric muons, and HNLs, while N_i^{obs} is the observed number of events in the bin. The expected number of events from each particle type is calculated by summing the weights of all events in the bin $N_i^{\text{type}} = \sum_i^{\text{type}} \omega_i$, with the statistical uncertainty being $(\sigma_i^{\text{type}})^2 = \sum_i^{\text{type}} \omega_i^2$. The additional term in Equation 7.1 is included to apply a penalty term for

prior knowledge of the systematic uncertainties of the parameters where they are known. s_j are the systematic parameters that are varied in the fit, while $\hat{s_j}$ are their nominal values and σ_{s_j} are the known uncertainties.

7.2.2 Physics Parameters

The variable physics parameter in this analysis is the mixing between the HNL and the SM τ sector, $|U_{\tau 4}|^2$. It is varied continuously in the range of [0.0 , 1.0] by applying the weighting scheme described in Section 4.2.3. The fit is initialized at an off-nominal value of 0.1. The other physics parameter, the mass m_4 of the HNL, is implicitly fixed to one of the three discrete masses to be tested, by using the corresponding sample of the HNL simulation described in Section 4.2.

7.2.3 Nuisance Parameters

All systematic parameters introduced in Section 5.4 apart from the detector calibration uncertainties, are already parameterized in a continuous way and can be varied in the fit. To be able to do the same with the detector uncertainties, a novel method is applied that will briefly be introduced here before going into the selection of the free parameters.

Treatment of Detector Systematic Uncertainties

Since the variations related to the detector calibration uncertainties introduced in Section 5.4.3 are estimated by simulating MC at discrete values of the systematic parameters, a method to derive continuous variations is needed to perform the fit. The method applied here was initially introduced in [151] and first used in the low energy sterile neutrino search in [19] (section 7.4.3). Using a *likelihood-free inference* technique, re-weighting factors are found for every event in the nominal MC sample, given a specific choice of detector systematic parameters. These factors quantify how much more or less likely the event would be for the corresponding change in detector response from the nominal parameters. Without going into the details of the method, which were already exhaustively discussed in [151] and [19], the performance is assessed here for the HNL signal simulation. In order to do so, the weights are applied to the nominal MC samples, choosing the detector systematic values used to produce the discrete samples and the resulting event expectations are compared to the expectations from the individual, discrete MC samples. The bin counts are compared by calculating the pull defined as

[151]: Fischer et al. (2023), "Treating detector systematics via a likelihood free inference method"
[19]: Trettin (2023), "Search for eV-scale sterile neutrinos with IceCube DeepCore"

$$p = \frac{N_{\text{reweighted}} - N_{sys}}{\sqrt{\sigma^2_{\text{reweighted}} + \sigma^2_{sys}}} , \tag{7.2}$$

where N are the bin-wise event expectations and σ are their MC uncertainty. For the SM BG simulation, the performance was already investigated in [125] (section 7.4.4, appendix B5) and the re-weighted nominal MC was shown to be in agreement with the discrete systematic sets at a sufficient level. Figure **??** shows the bin-wise pulls for the 1.0 GeV HNL mass sample at a mixing of 0.1 for a selection of the discrete systematic samples, where the DOM efficiency and the bulk ice absorption was varied by ±10%. As expected,

[125]: Lohfink (2023), "Testing non-standard neutrino interaction parameters with IceCube-DeepCore"

the pull distributions follow a standard normal distribution, without strong clustering or any systematic deviations. A similar performance is found for the additional systematic variations and the detailed figures can be found in Section B.2.

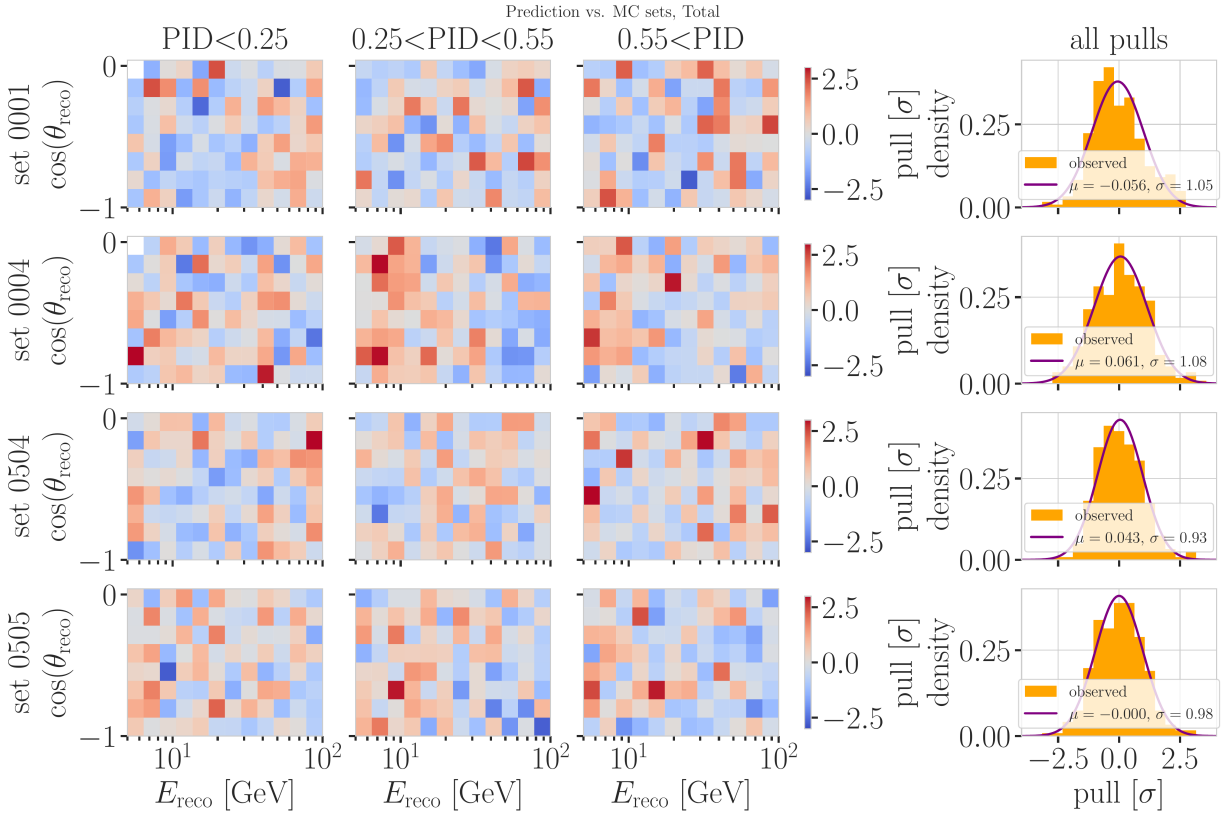

Figure 7.3: Three dimensional pulls and set-wise pull distributions between the nominal set and the specific systematic sets, after the nominal set was re-weighted to the correspoinding systematic parameter value.

fix caption (add description of what specific set number means (RED))

Free Parameters

To decide which systematic uncertainties should be included in the fit, we test the potential impact they have on the TS if they are neglected. The test is performed by creating Asimov data using the BG simulation and the HNL simulation of the 1.0 GeV mass sample at a mixing value of 0.1, which is chosen as a benchmark physics parameter, but the explicit choice does not have a significant impact on the test. The systematic parameter of interest is set to a value above its nominal expectation, either pulled up by $+1\sigma$ or by an educated estimate for parameters without a well-defined uncertainty. A fit is performed fixing the systematic parameter of interest and leaving all additional parameters free. The resulting TS is the fit metric difference between between this fit and a fit with all parameters free, which would result in a fit metric of 0.0 for this Asimov test. This difference is called mis-modeling significance and parameters below a significance of 0.1 σ are fixed. The test is performed in an iterative manner until the final set of free parameters is found.

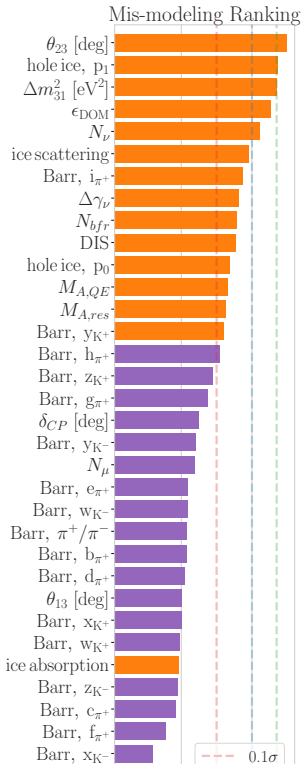

Figure 7.4 shows the resulting significances of one of these tests. The parameters tested are the systematic parameters introduced in Section 5.4 and the atmospheric oscillation parameters mentioned in Section 7.1. In the

final selection of free parameters the Barr h_{π^+} parameter was also left free, to sufficiently cover the relevant energy production range of the Pions, as can be seen in Figure 5.7, where both for Kaons and Pions the uncertainties are included for primary energies above 30 GeV and $x_{\text{lab}} > 0.1$. Additionally, the ice absorption is still kept free, despite showing a small significance, which is done because the bulk ice parameters are not well constrained and are known to have a large impact, which might be concealed in this idealized test, due to correlations with the other parameters. In this test, the effect of correlations is challenging to consider, because only the impact of one parameter is tested at a time, using the overall mis-modeling significance as a measure. The mis-modeling could be reduced by a correlated parameter capturing the effect of the parameter of interest. For this reason a very conservative threshold of $0.1\,\sigma$ is chosen and some parameters below the threshold are still left free in the fit.

All nuisance parameters that are left free in the fit are summarized in Table 7.4, showing their nominal values, the allowed fit ranges, and their Gaussian prior, if applicable. The scaling parameter N_ν is included to account for the overall normalization of the neutrino rate, and it has the identical effect on the SM neutrino events and the BSM HNL events, because they both originate from the same neutrino flux. Despite being known to ~5 % in this energy range, there is no prior applied to this parameter, because the fit itself is able to constrain it well, which can be seen by the large impact it shows in Figure 7.4. Concerning the atmospheric neutrino flux, the CR power law flux correction factor $\Delta\gamma_\nu$ introduced in Section 5.4.1 is included with nominal value of 0.0 which corresponds to the baseline flux model by Honda *et al* [75]. A slightly conservative prior of 0.1 is applied to the parameter, while latest measurements show an uncertainty of 0.05 [135]. The Barr parameters are contrained by a Gaussian prior, taken from [137]. All the detector systematic uncertainties discussed in Section 5.4.3 are included in the fit. The DOM efficiency ϵ_{DOM} is constrained by a Gaussian prior with a width of 0.1, which is a conservative estimate based on the studies of the optical efficiency using minimum ionizing muons from [85, 86]. The two atmospheric neutrino oscillation parameters θ_{23} and Δm^2_{31} are also included in the fit with nominal values of 47.5° and $2.48 \times 10^{-3}\,\text{eV}^2$ [129], respectively. Since they govern the shape and the strength of the tau neutrino flux, by defining the oscillation from ν_μ to ν_τ, they are also relevant for the HNL signal shape.

Need cite here! (RED)

[75]: Honda et al. (2015), "Atmospheric neutrino flux calculation using the NRLMSISE-00 atmospheric model"

[135]: Evans et al. (2017), "Uncertainties in atmospheric muon-neutrino fluxes arising from cosmic-ray primaries"

[137]: Barr et al. (2006), "Uncertainties in Atmospheric Neutrino Fluxes"

[85]: Feintzeig (2014), "Searches for Point-like Sources of Astrophysical Neutrinos with the IceCube Neutrino Observatory"

[86]: Kulacz (2019), "In Situ Measurement of the IceCube DOM Efficiency Factor Using Atmospheric Minimum Ionizing Muons"

[129]: Yu et al. (2023), "Recent neutrino oscillation result with the IceCube experiment"

7.2.4 Low Energy Analysis Framework

The analysis is performed using the PISA [152] [153] software framework, which was developed to perform analyses of small signals in high-statistics neutrino oscillation experiments. It is used to generate the expected event distributions from several MC samples, which can then be compared to the observed data. The expectation for each MC sample is calculated by applying physics and nuisance parameter effects in a stage-wise manner, before combining them to the final expectation.

I could add some final level effects of some systematics on the 3D binning and maybe discuss how they are different from the signal shape, or so? (ORANGE)

[152]: Aartsen et al. (2020), "Computational techniques for the analysis of small signals in high-statistics neutrino oscillation experiments"

Table 7.4: Systematic uncertainty parameters that are left free to float in the fit. Their allowed fit ranges are shown with the nominal value and the Gaussian prior width if applicable.

Parameter	Nominal	Range	Prior
$\theta_{23}[°]$	47.5047	[0.0, 90.0]	-
$\Delta m^2_{31}[\text{eV}^2]$	0.002475	[0.001, 0.004]	-
N_ν	1.0	[0.1, 2.0]	-
$\Delta\gamma_\nu$	0.0	[-0.5, 0.5]	0.1
Barr h_{π^+}	0.0	[-0.75, 0.75]	0.15
Barr i_{π^+}	0.0	[-3.05, 3.05]	0.61
Barr y_{K^+}	0.0	[-1.5, 1.5]	0.3
DIS	0.0	[-0.5, 1.5]	1.0
$M_{\text{A,QE}}$	0.0	[-2.0, 2.0]	1.0
$M_{\text{A,res}}$	0.0	[-2.0, 2.0]	1.0
ϵ_{DOM}	1.0	[0.8, 1.2]	0.1
hole ice p_0	0.101569	[-0.6, 0.5]	-
hole ice p_1	-0.049344	[-0.2, 0.2]	-
bulk ice absorption	1.0	[0.85, 1.15]	-
bulk ice scattering	1.05	[0.9, 1.2]	-
N_{bfr}	0.0	[-0.2, 1.2]	-

7.3 Analysis Checks

Fitting to data is performed in a *blind* manner, where the analyzer does not immediately see the fitted physics and nuisance parameter values, but first checks that a set of pre-defined *goodness of fit (GOF)* criteria are fulfilled. This is done to circumvent the so-called *confirmation bias* [154], where the analyzer might be tempted to construct the analysis in a way that confirms their expectation. After the GOF criteria are met to satisfaction, the fit results are unblinded and the full result can be revealed. Before these blind fits to data are performed, the robustness of the analysis method is tested using pseudo-data that is generated from the MC.

[154]: Nickerson (1998), "Confirmation Bias: A Ubiquitous Phenomenon in Many Guises"

7.3.1 Minimization Robustness

To find the set of parameters that best describes the data, a staged minimization routine is used. In the first stage, a fit with coarse minimizer settings is performed to find a rough estimate of the *best fit point (BFP)*. In the second stage, the fit is performed again in both octants[1] of θ_{23}, starting from the BFP of the coarse fit. For each individual fit the *MIGRAD* routine of IMINUIT [155] is used to minimize the χ^2_{mod} fit metric defined in Equation 7.1. Iminuit is a fast, python compatible minimizer based on the MINUIT2 C++ library [156]. The individual minimizer settings for both stages are shown in Table 7.5.

1: There is a degeneracy between the lower octant ($\theta_{23} < 45°$) and the upper octant ($\theta_{23} > 45°$), which can lead to fit metric minima (local and global) at two positions that are mirrored around 45° in θ_{23}.

[155]: Dembinski et al. (2022), *scikit-hep/iminuit: v2.17.0*

[156]: James et al. (1975), "Minuit: A System for Function Minimization and Analysis of the Parameter Errors and Correlations"

Fit	Err.	Prec.	Tol.
Coarse	1e-1	1e-8	1e-1
Fine	1e-5	1e-14	1e-5

Table 7.5: Migrad settings for the two stages in the minimization routine. *Err.* are the step size for the numerical gradient estimation, *Prec.* is the precision with which the LLH is calculated, and *Tol.* is the tolerance for the minimization.

To test the minimization routine and to make sure it consistently recovers any physics parameters, pseudo-data sets are produced from the MC by choosing the nominal nuisance parameters and specific physics parameters, without adding any statistical or systematic fluctuations to it. These so-called *Asimov*[2] data sets are then fit back with the full analysis chain. This type of test is called *Asimov inject/recover test*. A set of mixing values between 10^{-3} and 10^{0} is injected and fit back. Without fluctuations the fit is expected to always recover the injected parameters (both physics and nuisance parameters). The fitted mixing values from the Asimov inject/recover tests are compared to the true injected values in Figure 7.5 for all three mass samples. As desired, the fit is always able to recover the injected physics parameter and the

FInd first occurance of "Asimov" and add reference and explain it there (RED)

2: A pseudo-data set without statistical fluctuations is called Asimov data set.

nuisance parameters within the statistical uncertainty or at an insignificant fit metric difference.

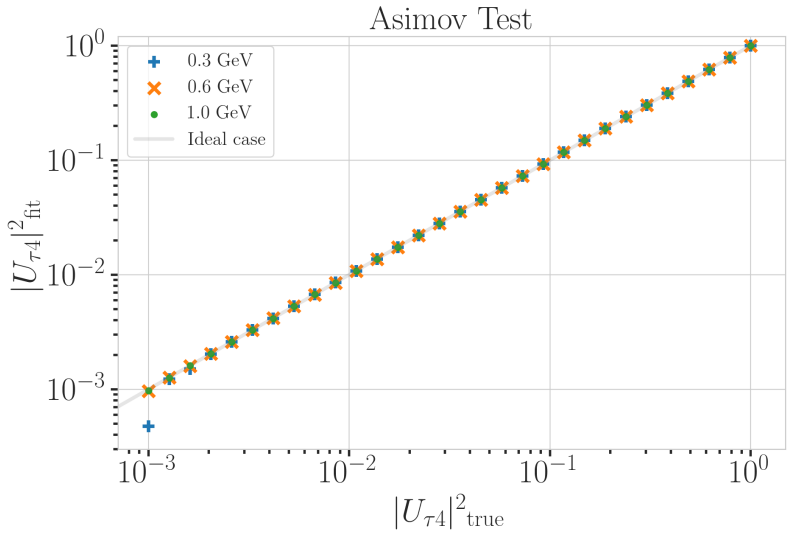

Figure 7.5: Asimov inject/recover test results for all three mass samples. Mixing values between 10^{-3} and 10^0 are injected and fit back with the full analysis chain. The injected parameter is always recovered within the statistical uncertainty or at an insignificant fit metric difference.

7.3.2 Goodness of Fit

To estimate the GOF, pseudo-data is generated from the MC by injecting the BFP parameters as true parameters and then fluctuating the expected bin counts to account for MC uncertainty and Poisson fluctuations in data. First, the expectation value of each bin is drawn from a Gaussian distribution centered at the nominal expectation value with a standard deviation corresponding to the MC uncertainty of the bin. Based on this sampled expectation value, each bin count is drawn from a Poisson distribution, independently, to get the final pseudo-data set. These pseudo-data sets are analyzed with the same analysis chain as the real data, resulting in a final fit metric value for each pseudo-data set. By comparing the distribution of fit metric values from this *ensemble* of pseudo-data trials to the fit metric of the fit to real data, a p-value can be calculated. The p-value is the probability of finding a value of the fit metric at least as large as the one from the data fit. Figure 7.6 shows the distribution from the ensemble tests for the 0.6 GeV mass sample and the observed value from the fit, resulting in a p-value of 28.5 %. The p-values for the 0.3 GeV and 1.0 GeV are 28.3 % and 26.0 %, respectively, and the corresponding plots are shown in Section **??**. Based on this test, it is concluded that the fit result is compatible with the expectation from the ensemble of pseudo-data trials.

7.3.3 Data/MC Agreement

At the BFP, the agreement between the data and simulation is probed by comparing both the one dimensional analysis distributions for PID, energy, and cosine of the zenith angle as well as the full three dimensional distributions. Figure 7.7 shows the three dimensional pull distribution between data and the total MC expectation for the 0.6 GeV mass sample at the BFP. The pulls are evenly spaced and show no strong clustering. In

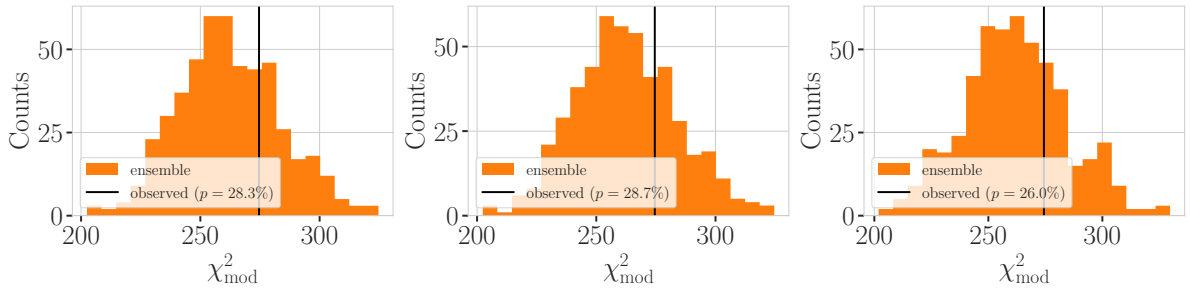

Figure 7.6: Observed fit metric (data fit) and fit metric distribution from pseudo-data ensemble generated around the best fit point. Shown are the results for all three mass samples, with the ensemble distribution on orange, the observed value in black, and the p-value in the legend.

Figure **??**, two examples of the one dimensional distributions for the energy and cosine of the zenith angle are shown for the 0.6 GeV mass sample. The data is compared to the total MC expectation, which is also split up into the individual signal and background components for illustration. Good agreement can be observed in the pull distributions, and is quantified by a reduced χ^2, which is close to 1.0 for all distributions. The reduced χ^2 for all investigated distributions is listed in Table **??**, while the distributions themselves can be found in Section **??**.

add 1-d data/mc agreement for example mass sample (0.6?) and all 3 analysis variables (RED)

add table with reduced chi2 for all 1-d distributions (RED)

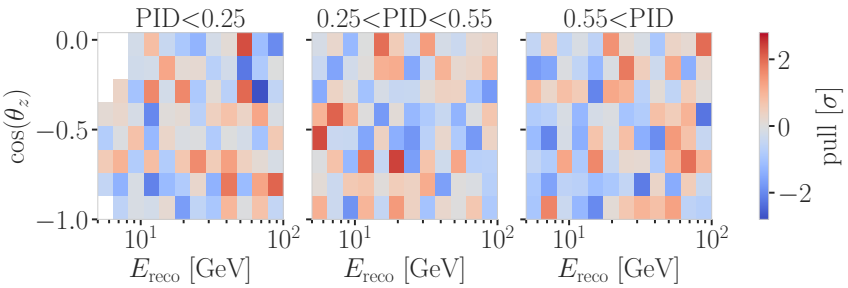

Figure 7.7

fix caption and describe plot in text (RED)

7.4 Results

7.4.1 Best Fit Nuisance Parameters

The resulting nuisance parameter values from the fits are illustrated in Figure 7.8, where the differences to the nominal values are shown, normalized by the distance to the closest boundary. The results from all three fits are shown in the same plot and the fits prefer values of the same size for all three mass samples. For parameters that have a Gaussian prior, the 1 σ range is also displayed. As was already confirmed during the blind fit procedure, all fitted parameters are within this range. The effective ice model parameter, N_{bfr}, prefers a value of ~0.74 , indicating that the data fits better to an ice model that includes real birefringence effects. For completeness, the explicit results are listed in Table B.1. There, the nominal values and the absolute differences to the best fit value are also presented.

Cite (again)! (RED)

Show best fit hole ice angular acceptance compared to nominal and flasher/in-situ fits, maybe? (YELLOW)

7.4.2 Agreement with Standard Model Three-Flavor Oscillation Measurement

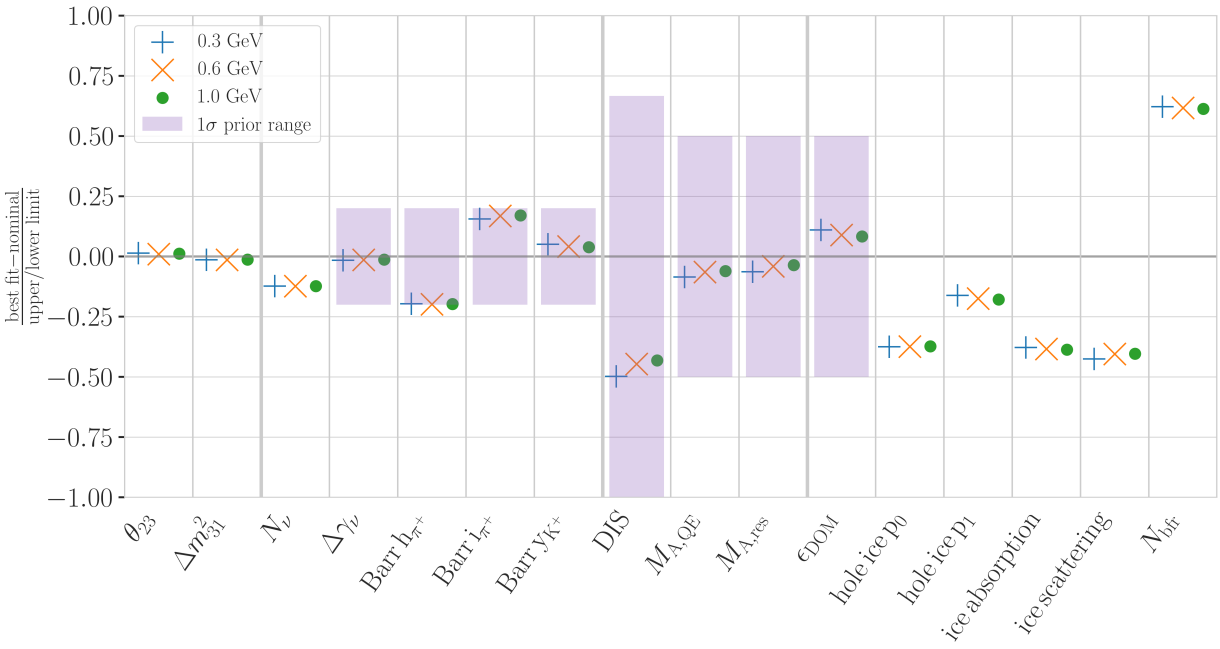

Figure 7.8: Best fit nuisance parameter distances to the nominal values, normalized by the distance to the closest boundary. For parameters with a Gaussian prior, the +1 σ range is also shown.

The recently performed atmospheric neutrino oscillation measurement by the IceCube collaboration resulted in a best fit point of $\sin^2\theta_{23} = 0.544^{+0.030}_{-0.096}$ and $\Delta m^2_{32} = 2.40^{+0.03}_{-0.06} \times 10^{-3}\text{eV}^2$ [129]. The result used the identical 10 years of data at the same final level selection, assuming normal mass ordering. The differences to this analysis are the choice of fit metric and the use of the previous treatment of detector systematic uncertainties. Both the choice of the fit metric and the detector systematic uncertainty treatment should not influence the best fit values and a naive comparison of the results to the results from this work is done, to validate this is the case. The best fit values are listed in Table 7.6 and are all compatible with the IceCube result within the uncertainties. Since they are statistically fully dependent, a more rigorous quantitative comparison would be more involved and is not performed here. The agreement is still interpreted as a first validation of the new detector systematics treatment.

m_4	$\sin^2\theta_{23}$	Δm^2_{32} [eV^2]
0.3 GeV	0.554	0.0238
0.6 GeV	0.551	0.0238
1.0 GeV	0.553	0.0238

Table 7.6: Best fit oscillation parameters from the three mass sample fits. The values are compatible with the IceCube result within the uncertainties.

[129]: Yu et al. (2023), "Recent neutrino oscillation result with the IceCube experiment"

7.4.3 Best Fit Parameters and Limits

The fitted mixing values are

$$|U_{\tau 4}|^2(0.3\,\text{GeV}) = 0.003^{+0.084}\,,$$
$$|U_{\tau 4}|^2(0.6\,\text{GeV}) = 0.080^{+0.134}\,,\text{and}$$
$$|U_{\tau 4}|^2(1.0\,\text{GeV}) = 0.106^{+0.132}\,,$$

with their +1 σ uncertainty. All of them are compatible with the null hypothesis of 0.0 mixing, although the 0.6 GeV and 1.0 GeV fits indicate a mixing value of 0.08 and 0.106 , respectively. The best fit mixing values and the corresponding upper limits at 68 % and 90 % *confidence level (CL)* are listed in Table 7.7, also showing the p-value to reject the null hypothesis. The CLs and p-value are estimated by assuming that *Wilks' theorem* [157] holds, meaning that the TS follows a χ^2 distribution with one degree of freedom.

[157]: Wilks (1938), "The Large-Sample Distribution of the Likelihood Ratio for Testing Composite Hypotheses"

Table 7.7: Best fit mixing values and the corresponding upper limits at 68 % and 90 % confidence level, as well as the p-value to reject the null hypothesis, estimated by assuming that Wilks' theorem holds.

HNL mass	$\lvert U_{\tau 4}\rvert^2$	68 % CL	90 % CL	NH p-value
0.3 GeV	0.003	0.09	0.19	0.97
0.6 GeV	0.080	0.21	0.36	0.79
1.0 GeV	0.106	0.24	0.40	0.63

Figure 7.9 shows the observed TS profiles as a function of $|U_{\tau 4}|^2$ for all three fits. The TS profile is the difference in χ^2_{mod} between the free fit and a fit where the mixing is fixed to a specific value. Also shown is the expected TS profile, based on 100 pseudo-data trials, produced at the BFP and then fluctuated using both Poisson and Gaussian fluctuations, to include the data and the MC uncertainty as was explained in Section 7.3.2. The Asimov expectation and the 68 % and 90 % bands are shown and the observed TS profiles lie within the 68 % band for all three, confirming that they are compatible with statistical fluctuations of the observed data. For the 0.3 GeV fit, the observed contour is slightly tighter than the Asimov expectation, meaning that the observed upper limits in $|U_{\tau 4}|^2$ are slightly stronger than expected. For the 0.6 GeV the opposite is the case and the observed upper limit is therefore slightly weaker than expected. For the 1.0 GeV fit, the observed upper limit is very close to the Asimov expectation in the region where the 68 % and 90 % CLs thresholds are crossed. The observed upper limits are also shown in Table 7.7.

make summary plot (masses and mixing limits on one) and then discuss wrt to other experiments? (RED)

7.4.4 Comparison to Other Experiments

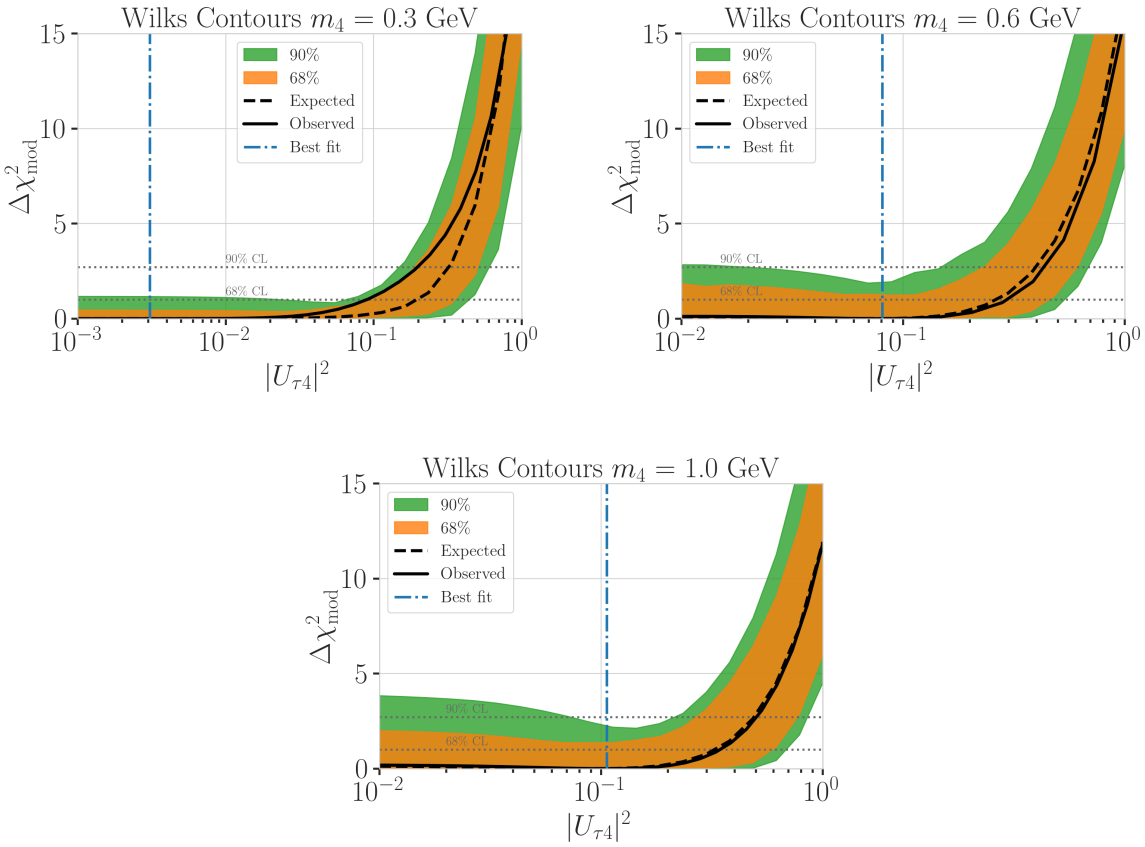

Figure 7.9: Best fit point TS profiles as a function of $|U_{\tau 4}|^2$ for the 0.3 GeV, 0.6 GeV, and 1.0 GeV mass samples. Shown are the observed profiles, the Asimov expectation at the best fit point, and the 68 % and 90 % bands, based on 100 pseudo-data trials. Also indicated are the 68 % and 90 % CL levels assuming Wilks' theorem.

7.5 Outlook

7.5.1 Shape Analysis Improvements

- estimate full contribution from cascade only events (underestimated due to limited sampling distributions)
- include double cascade classifier into Binning
- further optimize binning

7.5.2 Test Coupling to Electron/Muon Flavor

7.5.3 Test Additional Coupling Processes

7.5.4 IceCube Upgrade

8 Conclusion

Write conclusion (RED)

what was done?

1. set up model dependent and independent signal simulation for low energy double cascade events from HNL production and decay inside IceCube DeepCore

2. estimate performance of reconstructing and identifying these events

3. search for (cascade-like) events in 10 years of IceCube DeepCore data

Appendix

A

Heavy Neutral Lepton Signal Simulation

A.1 Model Independent Simulation Distributions

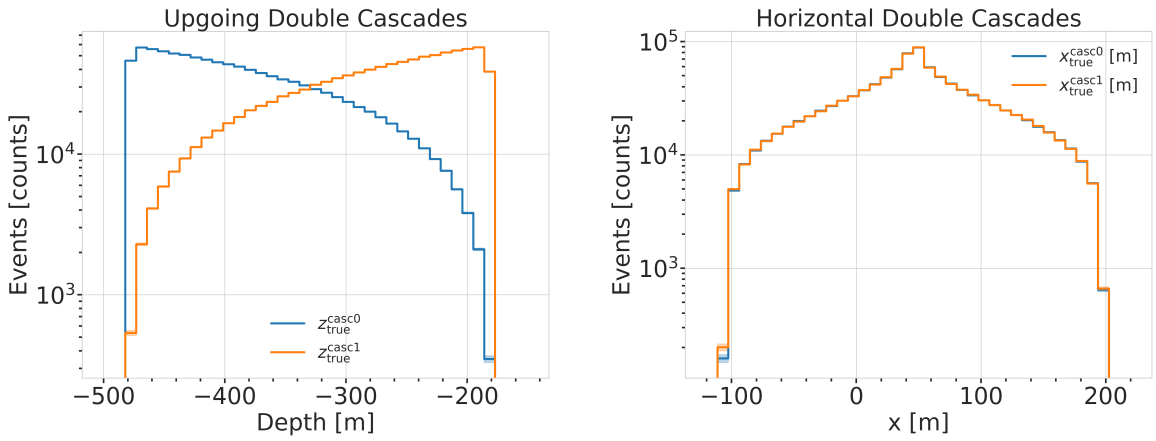

Figure A.1: Generation level distributions of the simplistic simulation sets. Vertical positions (left) and horizontal positions (right) of both sets are shown.

- Re-make plot with x,y for horizontal set one plot!
- Re-make plot with x, y, z for both cascades in one.
- Re-arrange plots in a more sensible way.

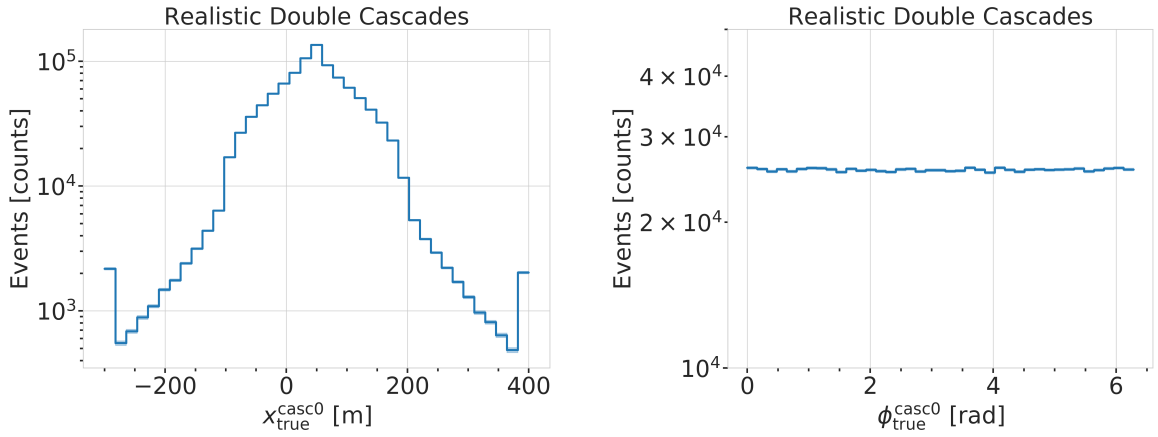

Figure A.2: Generation level distributions of the realistic simulation set. Shown are the cascade x, y, z positions (left) and direction angles (right).

A.2 Model Dependent Simulation Distributions

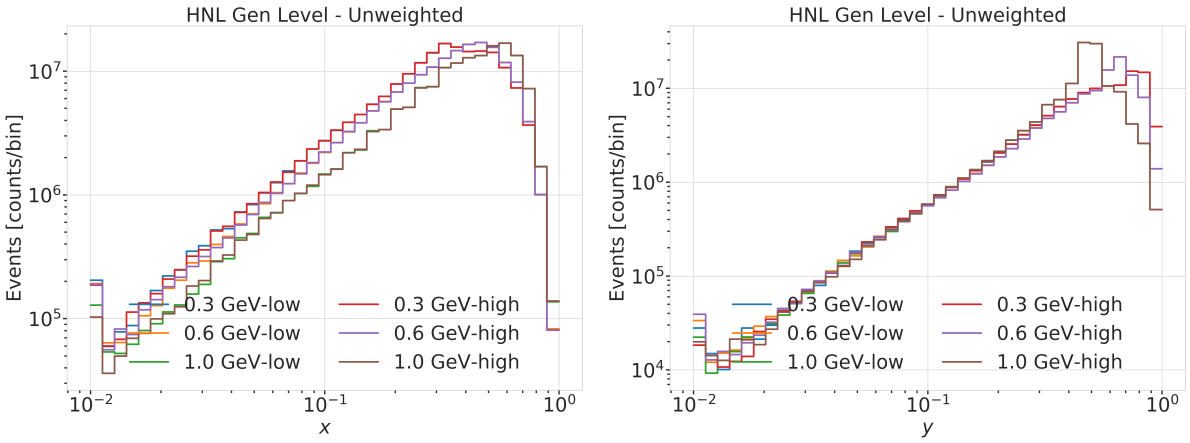

(a) Bjorken x

(b) Bjorken y

Figure A.3: Generation level distributions of the model dependent simulation.

B

Analysis Results

B.1 Final Level Simulation Distributions

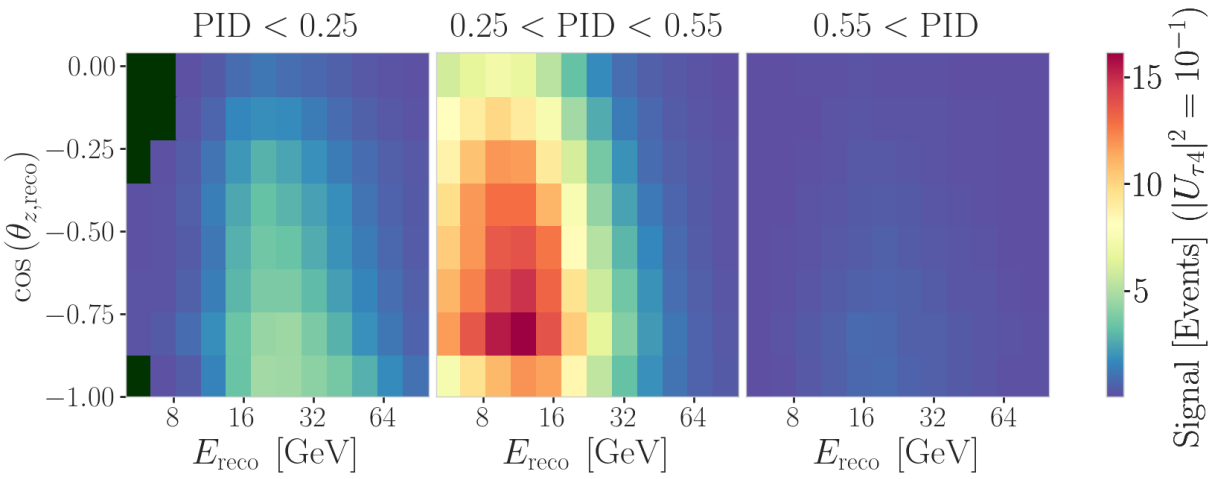

Figure B.1: Signal expectation in 9.28 years for the 1.0 GeV mass sample at a mixing of 0.1, while all other parameters are at their nominal values (top) and observed data (bottom).

B.2 Treatment of Detector Systematic Uncertainties

add description of what specific set number means (RED)

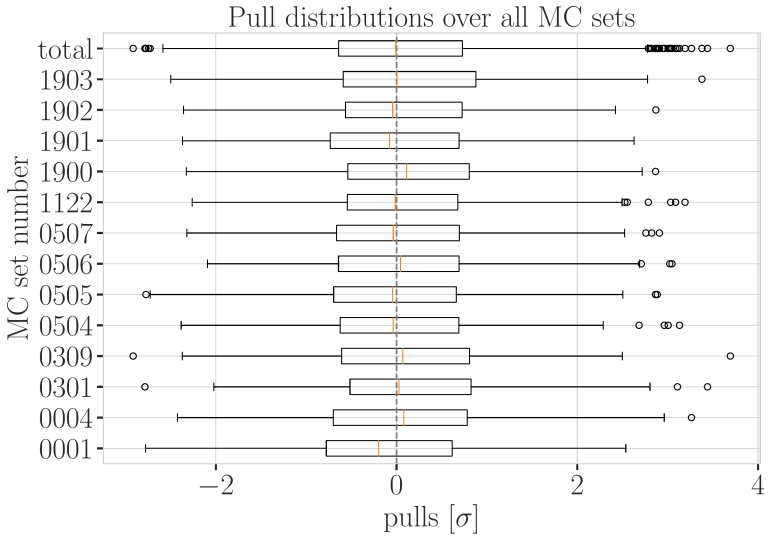

Figure B.2: Overall performance of the detector systematic uncertainty treatment. Shown are the pull distributions of the three dimensional pulls shown in Figure 7.3 and Figure B.3 between the nominal set and the specific systematic set, after the nominal set was re-weighted to the correspoinding systematic parameter value.

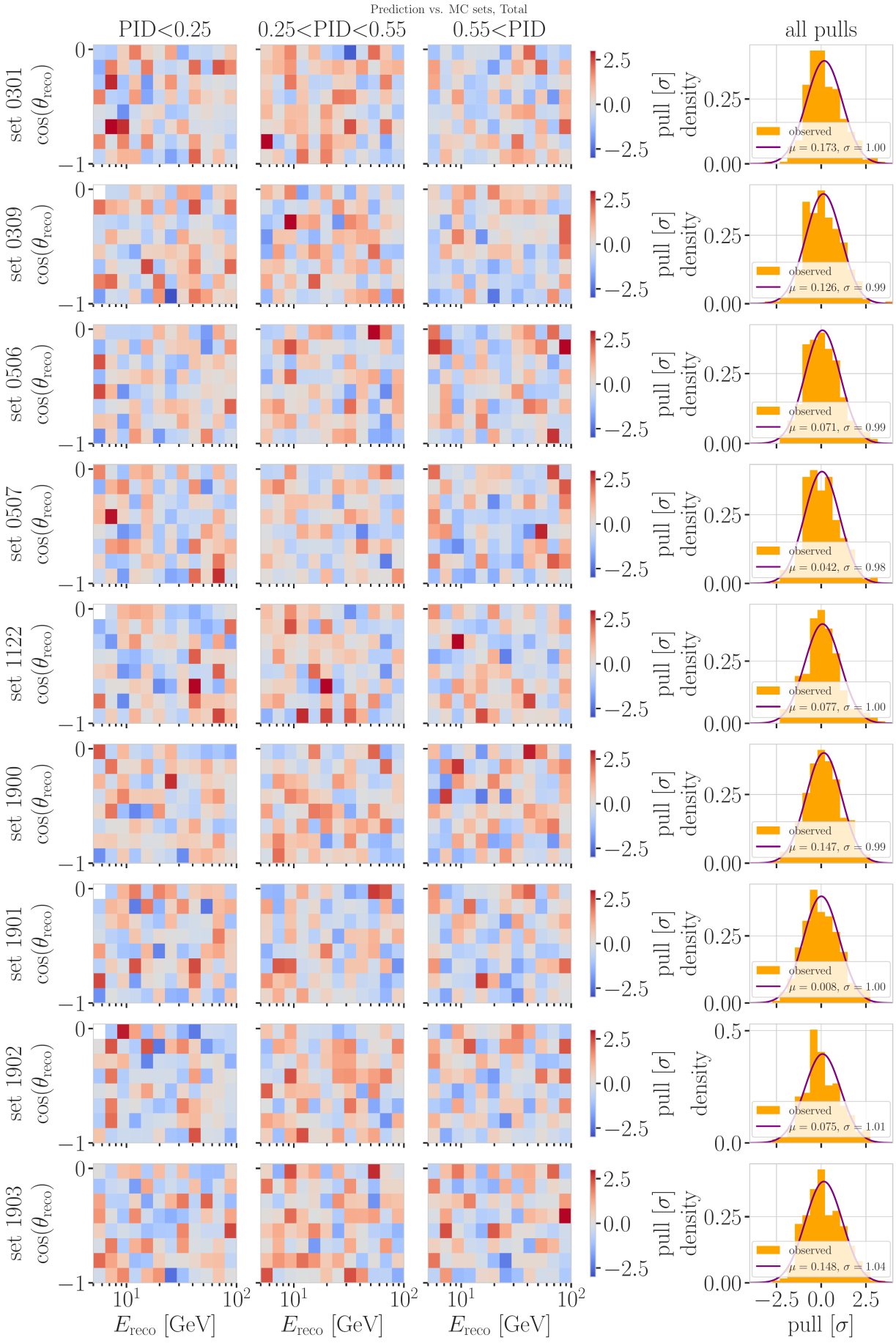

Figure B.3: Three dimensional pulls and set-wise pull distributions between the nominal set and the specific systematic sets, after the nominal set was re-weighted to the correspoinding systematic parameter value.

B.3 Best Fit Nuisance Parameters

Table B.1: Best fit nuisance parameters for the three mass samples. Also shown is the nominal value and the difference between the nominal and the best fit.

Parameter	Nominal	Best Fit			Nominal - Best Fit		
		0.3 GeV	0.6 GeV	1.0 GeV	0.3 GeV	0.6 GeV	1.0 GeV
$\|U_{\tau 4}\|^2$	-	0.003019	0.080494	0.106141	-	-	-
$\theta_{23}[^\circ]$	47.5047	48.117185	47.918758	48.010986	−0.612485	−0.414058	−0.506286
$\Delta m^2_{31}[\mathrm{eV}^2]$	0.002475	0.002454	0.002454	0.002455	0.000020	0.000021	0.000019
N_ν	1.0	0.889149	0.889055	0.889559	0.110851	0.110945	0.110441
$\Delta\gamma_\nu$	0.0	−0.007926	−0.006692	−0.006596	0.007926	0.006692	0.006596
Barr h_{π^+}	0.0	−0.147475	−0.148481	−0.148059	0.147475	0.148481	0.148059
Barr i_{π^+}	0.0	0.475448	0.513393	0.521626	−0.475448	−0.513393	−0.521626
Barr y_{K^+}	0.0	0.076176	0.062893	0.057548	−0.076176	−0.062893	−0.057548
DIS	0.0	−0.248709	−0.223302	−0.215666	0.248709	0.223302	0.215666
$M_{\mathrm{A,QE}}$	0.0	−0.170528	−0.128150	−0.120345	0.170528	0.128150	0.120345
$M_{\mathrm{A,res}}$	0.0	−0.125855	−0.080875	−0.070716	0.125855	0.080875	0.070716
ϵ_{DOM}	1.0	1.021984	1.017789	1.016689	−0.021984	−0.017789	−0.016689
hole ice p_0	0.101569	−0.161341	−0.161051	−0.160129	0.262910	0.262620	0.261698
hole ice p_1	−0.049344	−0.073701	−0.075596	−0.076261	0.024357	0.026252	0.026917
ice absorption	1.00	0.943261	0.942463	0.942000	0.056739	0.057537	0.058000
ice scattering	1.05	0.986152	0.989289	0.989438	0.063848	0.060711	0.060562
N_{bfr}	0.0	0.746684	0.740255	0.736215	−0.746684	−0.740255	−0.736215

fix design + significant digits to show (ORANGE)

maybe show range/prior and then deviation in sigma, or absolute for the ones without prior

List of Figures

List of Tables

Bibliography

Here are the references in citation order.

[1] W. Pauli. "Dear radioactive ladies and gentlemen". In: *Phys. Today* 31N9 (1978), p. 27 (cited on page 2).

[2] C. L. Cowan et al. "Detection of the Free Neutrino: a Confirmation". In: *Science* 124.3212 (1956), pp. 103–104. DOI: 10.1126/science.124.3212.103 (cited on page 2).

[3] G. Danby et al. "Observation of High-Energy Neutrino Reactions and the Existence of Two Kinds of Neutrinos". In: *Phys. Rev. Lett.* 9 (1 July 1962), pp. 36–44. DOI: 10.1103/PhysRevLett.9.36 (cited on page 2).

[4] K. Kodama et al. "Observation of tau neutrino interactions". In: *Physics Letters B* 504.3 (2001), pp. 218–224. DOI: https://doi.org/10.1016/S0370-2693(01)00307-0 (cited on page 2).

[5] R. Davis, D. S. Harmer, and K. C. Hoffman. "Search for Neutrinos from the Sun". In: *Phys. Rev. Lett.* 20 (21 May 1968), pp. 1205–1209. DOI: 10.1103/PhysRevLett.20.1205 (cited on pages 2, 8).

[6] M. G. Aartsen et al. "The IceCube Neutrino Observatory: instrumentation and online systems". In: *Journal of Instrumentation* 12.3 (Mar. 2017), P03012. DOI: 10.1088/1748-0221/12/03/P03012 (cited on pages 2, 23, 25, 46).

[7] C. N. Yang and R. L. Mills. "Conservation of Isotopic Spin and Isotopic Gauge Invariance". In: *Physical Review* 96.1 (Oct. 1954), pp. 191–195. DOI: 10.1103/PhysRev.96.191 (cited on page 5).

[8] S. Weinberg. "A Model of Leptons". In: *Phys. Rev. Lett.* 19 (21 Nov. 1967), pp. 1264–1266. DOI: 10.1103/PhysRevLett.19.1264 (cited on page 5).

[9] S. L. Glashow. "Partial-symmetries of weak interactions". In: *Nuclear Physics* 22.4 (Feb. 1961), pp. 579–588. DOI: 10.1016/0029-5582(61)90469-2 (cited on page 5).

[10] R. Jackiw. "Physical Formulations: Elementary Particle Theory. Relativistic Groups and Analyticity. Proceedings of the eighth Nobel Symposium, Aspenäsgården, Lerum, Sweden, May 1968. Nils Svartholm, Ed. Interscience (Wiley), New York, and Almqvist and Wiksell, Stockholm, 1969. 400 pp., illus. $31.75." In: *Science* 168.3936 (1970), pp. 1196–1197. DOI: 10.1126/science.168.3936.1196.b (cited on page 5).

[11] P. Higgs. "Broken symmetries, massless particles and gauge fields". In: *Physics Letters* 12.2 (1964), pp. 132–133. DOI: https://doi.org/10.1016/0031-9163(64)91136-9 (cited on page 5).

[12] S. Chatrchyan et al. "Observation of a New Boson at a Mass of 125 GeV with the CMS Experiment at the LHC". In: *Phys. Lett. B* 716 (2012), pp. 30–61. DOI: 10.1016/j.physletb.2012.08.021 (cited on page 5).

[13] G. Aad et al. "Observation of a new particle in the search for the Standard Model Higgs boson with the ATLAS detector at the LHC". In: *Phys. Lett. B* 716 (2012), pp. 1–29. DOI: 10.1016/j.physletb.2012.08.020 (cited on page 5).

[14] M. Gell-Mann. "A Schematic Model of Baryons and Mesons". In: *Resonance* 24 (1964), pp. 923–925 (cited on page 5).

[15] G. Zweig. "An SU(3) model for strong interaction symmetry and its breaking. Version 2". In: *DEVELOPMENTS IN THE QUARK THEORY OF HADRONS. VOL. 1. 1964 - 1978.* Ed. by D. B. Lichtenberg and S. P. Rosen. Feb. 1964, pp. 22–101 (cited on page 5).

[16] D. J. Gross and F. Wilczek. "Ultraviolet Behavior of Non-Abelian Gauge Theories". In: *PRL* 30.26 (June 1973), pp. 1343–1346. DOI: 10.1103/PhysRevLett.30.1343 (cited on page 5).

[17] C. Giunti and C. W. Kim. *Fundamentals of Neutrino Physics and Astrophysics*. Oxford University Press, Mar. 2007 (cited on page 5).

[18] M. D. Schwartz. *Quantum Field Theory and the Standard Model*. Cambridge University Press, 2013 (cited on page 5).

[19] A. Trettin. "Search for eV-scale sterile neutrinos with IceCube DeepCore". PhD thesis. Berlin, Germany: Humboldt-Universität zu Berlin, Mathematisch-Naturwissenschaftliche Fakultät, 2023. DOI: https://github.com/atrettin/PhD-Thesis (cited on pages 7, 10, 44, 46, 55, 75).

[20] N. Deruelle, J.-P. Uzan, and P. de Forcrand-Millard. *Relativity in Modern Physics*. Oxford University Press, Aug. 2018 (cited on page 8).

[21] R. L. Workman et al. "Review of Particle Physics". In: *Progress of Theoretical and Experimental Physics* 2022.8 (Aug. 2022), p. 083C01. DOI: 10.1093/ptep/ptac097 (cited on pages 8, 27, 28).

[22] M. Fukugita and T. Yanagida. "Barygenesis without grand unification". In: *Physics Letters B* 174.1 (1986), pp. 45–47. DOI: https://doi.org/10.1016/0370-2693(86)91126-3 (cited on page 8).

[23] Y. Fukuda et al. "Evidence for Oscillation of Atmospheric Neutrinos". In: *Phys. Rev. Lett.* 81 (8 Aug. 1998), pp. 1562–1567. DOI: 10.1103/PhysRevLett.81.1562 (cited on page 8).

[24] Q. R. Ahmad and other. "Direct Evidence for Neutrino Flavor Transformation from Neutral-Current Interactions in the Sudbury Neutrino Observatory". In: *Phys. Rev. Lett.* 89 (1 June 2002), p. 011301. DOI: 10.1103/PhysRevLett.89.011301 (cited on page 8).

[25] S. Alam et al. "Completed SDSS-IV extended Baryon Oscillation Spectroscopic Survey: Cosmological implications from two decades of spectroscopic surveys at the Apache Point Observatory". In: *Phys. Rev. D* 103 (8 Apr. 2021), p. 083533. DOI: 10.1103/PhysRevD.103.083533 (cited on page 8).

[26] N. Aghanim et al. "Planck2018 results: VI. Cosmological parameters". In: *Astronomy & Astrophysics* 641 (Sept. 2020), A6. DOI: 10.1051/0004-6361/201833910 (cited on page 8).

[27] M. Aker et al. "Direct neutrino-mass measurement with sub-electronvolt sensitivity". In: *Nature Phys.* 18.2 (2022), pp. 160–166. DOI: 10.1038/s41567-021-01463-1 (cited on page 8).

[28] T. Asaka, S. Blanchet, and M. Shaposhnikov. "The nuMSM, dark matter and neutrino masses". In: *Phys. Lett. B* 631 (2005), pp. 151–156. DOI: 10.1016/j.physletb.2005.09.070 (cited on page 10).

[29] T. Asaka and M. Shaposhnikov. "The νMSM, dark matter and baryon asymmetry of the universe". In: *Phys. Lett. B* 620 (2005), pp. 17–26. DOI: 10.1016/j.physletb.2005.06.020 (cited on page 10).

[30] P. Minkowski. "$\mu \to e\,\gamma$ at a rate of one out of 10^9 muon decays?" In: *Physics Letters B* 67.4 (Apr. 1977), pp. 421–428. DOI: 10.1016/0370-2693(77)90435-X (cited on page 10).

[31] T. Yanagida. "Horizontal Symmetry and Masses of Neutrinos". In: *Progress of Theoretical Physics* 64.3 (Sept. 1980), pp. 1103–1105. DOI: 10.1143/PTP.64.1103 (cited on page 10).

[32] S. L. Glashow. "The Future of Elementary Particle Physics". In: *NATO Sci. Ser. B* 61 (1980), p. 687. DOI: 10.1007/978-1-4684-7197-7_15 (cited on page 10).

[33] M. Gell-Mann, P. Ramond, and R. Slansky. "Complex Spinors and Unified Theories". In: *Conf. Proc. C* 790927 (1979), pp. 315–321 (cited on page 10).

[34] R. N. Mohapatra and G. Senjanovi ć. "Neutrino Mass and Spontaneous Parity Nonconservation". In: *Phys. Rev. Lett.* 44 (14 Apr. 1980), pp. 912–915. DOI: 10.1103/PhysRevLett.44.912 (cited on page 10).

[35] M. G. Aartsen et al. "eV-Scale Sterile Neutrino Search Using Eight Years of Atmospheric Muon Neutrino Data from the IceCube Neutrino Observatory". In: *Phys. Rev. Lett.* 125.14 (2020), p. 141801. DOI: 10.1103/PhysRevLett.125.141801 (cited on page 10).

[36] J.-L. Tastet, O. Ruchayskiy, and I. Timiryasov. "Reinterpreting the ATLAS bounds on heavy neutral leptons in a realistic neutrino oscillation model". In: *JHEP* 12 (2021), p. 182. DOI: 10.1007/JHEP12(2021)182 (cited on page 10).

[37] D. A. Bryman and R. Shrock. "Constraints on Sterile Neutrinos in the MeV to GeV Mass Range". In: *Phys. Rev. D* 100 (2019), p. 073011. DOI: 10.1103/PhysRevD.100.073011 (cited on pages 11, 12).

[38] A. Aguilar-Arevalo et al. "Improved search for heavy neutrinos in the decay $\pi \to e\nu$". In: *Phys. Rev. D* 97.7 (2018), p. 072012. DOI: 10.1103/PhysRevD.97.072012 (cited on page 11).

[39] G. Bellini et al. "New limits on heavy sterile neutrino mixing in B8 decay obtained with the Borexino detector". In: *Phys. Rev. D* 88.7 (2013), p. 072010. DOI: 10.1103/PhysRevD.88.072010 (cited on pages 11, 14).

[40] D. Britton et al. "Improved search for massive neutrinos in $\pi + \rightarrow e + \nu$ decay". In: *Physical Review D* 46 (1992) (cited on page 11).

[41] C. J. Parkinson et al. "Search for heavy neutral lepton production at the NA62 experiment". In: *PoS* EPS-HEP2021 (2022), p. 686. DOI: 10.22323/1.398.0686 (cited on pages 11, 12).

[42] K. Abe et al. "Search for heavy neutrinos with the T2K near detector ND280". In: *Phys. Rev. D* 100.5 (2019), p. 052006. DOI: 10.1103/PhysRevD.100.052006 (cited on pages 11, 12).

[43] P. Abreu et al. "Search for neutral heavy leptons produced in Z decays". In: *Z. Phys. C* 74 (1997). [Erratum: Z.Phys.C 75, 580 (1997)], pp. 57–71. DOI: 10.1007/s002880050370 (cited on pages 11, 13).

[44] R. Barouki, G. Marocco, and S. Sarkar. "Blast from the past II: Constraints on heavy neutral leptons from the BEBC WA66 beam dump experiment". In: *SciPost Phys.* 13 (2022), p. 118. DOI: 10.21468/SciPostPhys.13.5.118 (cited on pages 11–13).

[45] F. Bergsma et al. "A Search for Decays of Heavy Neutrinos". In: *Phys. Lett. B* 128 (1983). Ed. by J. Tran Thanh Van, p. 361. DOI: 10.1016/0370-2693(83)90275-7 (cited on page 11).

[46] G. Aad et al. "Search for heavy neutral leptons in decays of W bosons produced in 13 TeV pp collisions using prompt and displaced signatures with the ATLAS detector". In: *JHEP* 10 (2019), p. 265. DOI: 10.1007/JHEP10(2019)265 (cited on pages 11, 12).

[47] G. Aad et al. "Search for Heavy Neutral Leptons in Decays of W Bosons Using a Dilepton Displaced Vertex in $\sqrt{s}$ = 13TeV pp Collisions with the ATLAS Detector". In: *Phys. Rev. Lett.* 131 (6 Aug. 2023), p. 061803. DOI: 10.1103/PhysRevLett.131.061803 (cited on pages 11, 12).

[48] A. M. Sirunyan et al. "Search for heavy neutral leptons in events with three charged leptons in proton-proton collisions at $\sqrt{s}$ = 13 TeV". In: *Phys. Rev. Lett.* 120.22 (2018), p. 221801. DOI: 10.1103/PhysRevLett.120.221801 (cited on pages 11, 12).

[49] A. Tumasyan et al. "Search for long-lived heavy neutral leptons with displaced vertices in proton-proton collisions at $\sqrt{s}$ =13 TeV". In: *JHEP* 07 (2022), p. 081. DOI: 10.1007/JHEP07(2022)081 (cited on pages 11, 12).

[50] A. Vaitaitis et al. "Search for neutral heavy leptons in a high-energy neutrino beam". In: *Phys. Rev. Lett.* 83 (1999), pp. 4943–4946. DOI: 10.1103/PhysRevLett.83.4943 (cited on pages 11, 12).

[51] E. Fernandez-Martinez et al. "Effective portals to heavy neutral leptons". In: *JHEP* 09 (2023), p. 001. DOI: 10.1007/JHEP09(2023)001 (cited on pages 11–13).

[52] G. Bernardi et al. "Search for Neutrino Decay". In: *Phys. Lett. B* 166 (1986), pp. 479–483. DOI: 10.1016/0370-2693(86)91602-3 (cited on page 11).

[53] S. Ito et al. "Search for heavy neutrinos in $\pi^+ \rightarrow \mu^+\nu$ decay and status of lepton universality test in the PIENU experiment". In: *JPS Conf. Proc.* 33 (2021). Ed. by N. Saito, pp. 011131-1–011131-6. DOI: 10.7566/JPSCP.33.011131 (cited on page 11).

[54] A. V. Artamonov et al. "Search for heavy neutrinos in $K^+ \rightarrow \mu^+\nu_H$ decays". In: *Phys. Rev. D* 91.5 (2015). [Erratum: Phys.Rev.D 91, 059903 (2015)], p. 052001. DOI: 10.1103/PhysRevD.91.052001 (cited on pages 11, 12).

[55] P. Abratenko et al. "Search for Heavy Neutral Leptons in Electron-Positron and Neutral-Pion Final States with the MicroBooNE Detector". In: *Phys. Rev. Lett.* 132.4 (2024), p. 041801. DOI: 10.1103/PhysRevLett.132.041801 (cited on pages 11, 12).

[56] P. Astier et al. "Search for heavy neutrinos mixing with tau neutrinos". In: *Phys. Lett. B* 506 (2001), pp. 27–38. DOI: 10.1016/S0370-2693(01)00362-8 (cited on page 11).

[57] J. Orloff, A. N. Rozanov, and C. Santoni. "Limits on the mixing of tau neutrino to heavy neutrinos". In: *Phys. Lett. B* 550 (2002), pp. 8–15. DOI: 10.1016/S0370-2693(02)02769-7 (cited on pages 12, 13).

[58] I. Boiarska et al. "Constraints from the CHARM experiment on heavy neutral leptons with tau mixing". In: *Phys. Rev. D* 104.9 (2021), p. 095019. DOI: 10.1103/PhysRevD.104.095019 (cited on pages 12, 13).

[59] A. Cooper-Sarkar et al. "Search for heavy neutrino decays in the BEBC beam dump experiment". In: *Physics Letters B* 160.1 (1985), pp. 207–211. DOI: https://doi.org/10.1016/0370-2693(85)91493-5 (cited on page 12).

[60] B. Shuve and M. E. Peskin. "Revision of the LHCb Limit on Majorana Neutrinos". In: *Phys. Rev. D* 94.11 (2016), p. 113007. DOI: 10.1103/PhysRevD.94.113007 (cited on page 12).

[61] R. Aaij et al. "Search for heavy neutral leptons in $W^+ \to \mu^+\mu^\pm$jet decays". In: *Eur. Phys. J. C* 81.3 (2021), p. 248. DOI: 10.1140/epjc/s10052-021-08973-5 (cited on page 12).

[62] R. Plestid. "Luminous solar neutrinos I: Dipole portals". In: *Phys. Rev. D* 104 (2021), p. 075027. DOI: 10.1103/PhysRevD.104.075027 (cited on pages 13, 14).

[63] A. Osipowicz et al. "KATRIN: A Next generation tritium beta decay experiment with sub-eV sensitivity for the electron neutrino mass. Letter of intent". In: (Sept. 2001) (cited on page 13).

[64] S. Mertens et al. "A novel detector system for KATRIN to search for keV-scale sterile neutrinos". In: *Journal of Physics G: Nuclear and Particle Physics* 46.6 (2019), p. 065203. DOI: 10.1088/1361-6471/ab12fe (cited on page 13).

[65] M. Aker et al. "Search for keV-scale sterile neutrinos with the first KATRIN data". In: *Eur. Phys. J. C* 83.8 (2023), p. 763. DOI: 10.1140/epjc/s10052-023-11818-y (cited on page 13).

[66] B. Abi et al. "Deep Underground Neutrino Experiment (DUNE), Far Detector Technical Design Report, Volume II: DUNE Physics". In: (Feb. 2020) (cited on page 13).

[67] S. Friedrich et al. "Limits on the Existence of sub-MeV Sterile Neutrinos from the Decay of ^{7}Be in Superconducting Quantum Sensors". In: *Phys. Rev. Lett.* 126.2 (2021), p. 021803. DOI: 10.1103/PhysRevLett.126.021803 (cited on page 13).

[68] C. Hagner et al. "Experimental search for the neutrino decay v3+vj+e++e- and limits on neutrino mixing". English. In: 52.3 (1995), pp. 1343–1352. DOI: 10.1103/PhysRevD.52.1343 (cited on page 13).

[69] R. Plestid. "Luminous solar neutrinos II: Mass-mixing portals". In: *Phys. Rev. D* 104 (2021). [Erratum: Phys.Rev.D 105, 099901 (2022)], p. 075028. DOI: 10.1103/PhysRevD.104.075028 (cited on page 14).

[70] P. Coloma et al. "Double-Cascade Events from New Physics in Icecube". In: *Phys. Rev. Lett.* 119.20 (2017), p. 201804. DOI: 10.1103/PhysRevLett.119.201804 (cited on page 14).

[71] P. Coloma. "Icecube/DeepCore tests for novel explanations of the MiniBooNE anomaly". In: *Eur. Phys. J. C* 79.9 (2019), p. 748. DOI: 10.1140/epjc/s10052-019-7256-8 (cited on page 14).

[72] M. Atkinson et al. "Heavy Neutrino Searches through Double-Bang Events at Super-Kamiokande, DUNE, and Hyper-Kamiokande". In: *JHEP* 04 (2022), p. 174. DOI: 10.1007/JHEP04(2022)174 (cited on page 14).

[73] P. Coloma et al. "GeV-scale neutrinos: interactions with mesons and DUNE sensitivity". In: *Eur. Phys. J. C* 81.1 (2021), p. 78. DOI: 10.1140/epjc/s10052-021-08861-y (cited on pages 14, 20, 35, 37, 38).

[74] M. Tanabashi et al. "Review of Particle Physics". In: *Phys. Rev. D* 98 (3 Aug. 2018), p. 030001. DOI: 10.1103/PhysRevD.98.030001 (cited on pages 15, 17, 28).

[75] M. Honda et al. "Atmospheric neutrino flux calculation using the NRLMSISE-00 atmospheric model". In: *Phys. Rev. D* 92 (2 July 2015), p. 023004. DOI: 10.1103/PhysRevD.92.023004 (cited on pages 15, 41, 77).

[76] A. Fedynitch et al. "Calculation of conventional and prompt lepton fluxes at very high energy". In: *European Physical Journal Web of Conferences*. Vol. 99. European Physical Journal Web of Conferences. Aug. 2015, p. 08001. DOI: 10.1051/epjconf/20159908001 (cited on page 16).

[77] P. A. M. Dirac. "The Quantum Theory of the Emission and Absorption of Radiation". In: *Proceedings of the Royal Society of London Series A* 114.767 (Mar. 1927), pp. 243–265. DOI: 10.1098/rspa.1927.0039 (cited on page 16).

[78] I. Esteban et al. “The fate of hints: updated global analysis of three-flavor neutrino oscillations”. In: *JHEP* 09 (2020), p. 178. DOI: 10.1007/JHEP09(2020)178 (cited on page 17).

[79] A. Terliuk. “Measurement of atmospheric neutrino oscillations and search for sterile neutrino mixing with IceCube DeepCore”. PhD thesis. Berlin, Germany: Humboldt-Universität zu Berlin, Mathematisch-Naturwissenschaftliche Fakultät, 2018. DOI: 10.18452/19304 (cited on pages 18, 30).

[80] J. A. Formaggio and G. P. Zeller. “From eV to EeV: Neutrino cross sections across energy scales”. In: *Rev. Mod. Phys.* 84 (3 Sept. 2012), pp. 1307–1341. DOI: 10.1103/RevModPhys.84.1307 (cited on page 19).

[81] P. B. Price, K. Woschnagg, and D. Chirkin. “Age vs depth of glacial ice at South Pole”. In: *Geophysical Research Letters* 27.14 (2000), pp. 2129–2132. DOI: https://doi.org/10.1029/2000GL011351 (cited on page 24).

[82] R. Abbasi et al. “In-situ estimation of ice crystal properties at the South Pole using LED calibration data from the IceCube Neutrino Observatory”. In: *The Cryosphere Discussions* 2022 (2022), pp. 1–48. DOI: 10.5194/tc-2022-174 (cited on page 24).

[83] R. Abbasi et al. “The IceCube data acquisition system: Signal capture, digitization, and timestamping”. In: *Nuclear Instruments and Methods in Physics Research Section A: Accelerators, Spectrometers, Detectors and Associated Equipment* 601.3 (2009), pp. 294–316. DOI: https://doi.org/10.1016/j.nima.2009.01.001 (cited on pages 24, 25, 46).

[84] M. G. Aartsen et al. “Energy Reconstruction Methods in the IceCube Neutrino Telescope”. In: *JINST* 9 (2014), P03009. DOI: 10.1088/1748-0221/9/03/P03009 (cited on pages 25, 57).

[85] J. Feintzeig. “Searches for Point-like Sources of Astrophysical Neutrinos with the IceCube Neutrino Observatory”. PhD thesis. University of Wisconsin, Madison, Jan. 2014 (cited on pages 25, 54, 77).

[86] N. Kulacz. “In Situ Measurement of the IceCube DOM Efficiency Factor Using Atmospheric Minimum Ionizing Muons”. MA thesis. University of Alberta, 2019 (cited on pages 25, 54, 77).

[87] R. Abbasi et al. “The design and performance of IceCube DeepCore”. In: *Astropart. Phys.* 35.10 (2012), pp. 615–624. DOI: 10.1016/j.astropartphys.2012.01.004 (cited on pages 26, 46).

[88] P. A. Cherenkov. “Visible Radiation Produced by Electrons Moving in a Medium with Velocities Exceeding that of Light”. In: *Phys. Rev.* 52 (4 Aug. 1937), pp. 378–379. DOI: 10.1103/PhysRev.52.378 (cited on page 27).

[89] V. F. Petrenko and R. W. Whitworth. “214Optical and electronic properties”. In: *Physics of Ice*. Oxford University Press, Jan. 2002. DOI: 10.1093/acprof:oso/9780198518945.003.0009 (cited on page 27).

[90] I. Frank and I. Tamm. “Coherent visible radiation from fast electrons passing through matter”. In: *C. R. Acad. Sci. USSR* 14 (1937), pp. 109–114 (cited on page 27).

[91] I. Tamm. “Radiation Emitted by Uniformly Moving Electrons”. In: *Selected Papers*. Ed. by B. M. Bolotovskii, V. Y. Frenkel, and R. Peierls. Berlin, Heidelberg: Springer Berlin Heidelberg, 1991, pp. 37–53. DOI: 10.1007/978-3-642-74626-0_3 (cited on page 27).

[92] L. Rädel and C. Wiebusch. “Calculation of the Cherenkov light yield from low energetic secondary particles accompanying high-energy muons in ice and water with Geant4 simulations”. In: *Astroparticle Physics* 38 (Oct. 2012), pp. 53–67. DOI: 10.1016/j.astropartphys.2012.09.008 (cited on pages 27, 34, 42).

[93] D. Chirkin and W. Rhode. “Propagating leptons through matter with Muon Monte Carlo (MMC)”. In: (July 2004) (cited on page 28).

[94] L. Raedel. “Simulation Studies of the Cherenkov Light Yield from Relativistic Particles in High-Energy Neutrino Telescopes with Geant4”. MA thesis. Aachen, Germany: Rheinisch-Westfälischen Technischen Hochschule, 2012 (cited on pages 28, 29).

[95] E. Longo and I. Sestili. “Monte Carlo Calculation of Photon Initiated Electromagnetic Showers in Lead Glass”. In: *Nucl. Instrum. Meth.* 128 (1975). [Erratum: Nucl.Instrum.Meth. 135, 587 (1976)], p. 283. DOI: 10.1016/0029-554X(75)90679-5 (cited on page 28).

[96] S. Agostinelli et al. “Geant4—a simulation toolkit”. In: *Nucl. Instr. Meth. Phys. Res.* 506.3 (July 2003), pp. 250–303. DOI: 10.1016/s0168-9002(03)01368-8 (cited on pages 28, 34, 42).

[97] T. Gabriel et al. “Energy dependence of hadronic activity”. In: *Nuclear Instruments and Methods in Physics Research Section A: Accelerators, Spectrometers, Detectors and Associated Equipment* 338.2 (1994), pp. 336–347. DOI: https://doi.org/10.1016/0168-9002(94)91317-X (cited on page 29).

[98] L. Fischer. https://github.com/LeanderFischer/icetray_double_cascade_generator_functions (cited on page 31).

[99] R. Abbasi et al. “LeptonInjector and LeptonWeighter: A neutrino event generator and weighter for neutrino observatories”. In: *Comput. Phys. Commun.* 266 (2021), p. 108018. DOI: 10.1016/j.cpc.2021.108018 (cited on page 34).

[100] J. Alwall et al. “The automated computation of tree-level and next-to-leading order differential cross sections, and their matching to parton shower simulations”. In: *JHEP* 07 (2014), p. 079. DOI: 10.1007/JHEP07(2014)079 (cited on page 35).

[101] C. Argüelles. https://github.com/arguelles/NuXSSplMkr (cited on pages 35, 36).

[102] N. Whitehorn, J. van Santen, and S. Lafebre. “Penalized splines for smooth representation of high-dimensional Monte Carlo datasets”. In: *Computer Physics Communications* 184.9 (2013), pp. 2214–2220. DOI: https://doi.org/10.1016/j.cpc.2013.04.008 (cited on pages 35, 57).

[103] J.-M. Levy. “Cross-section and polarization of neutrino-produced tau’s made simple”. In: *J. Phys. G* 36 (2009), p. 055002. DOI: 10.1088/0954-3899/36/5/055002 (cited on page 36).

[104] E. Tiesinga et al. “CODATA recommended values of the fundamental physical constants: 2018”. In: *Rev. Mod. Phys.* 93 (2 July 2021), p. 025010. DOI: 10.1103/RevModPhys.93.025010 (cited on page 37).

[105] https://launchpad.net/mg5amcnlo/3.0/3.3.x (cited on page 38).

[106] A. Alloul et al. “FeynRules 2.0 - A complete toolbox for tree-level phenomenology”. In: *Comput. Phys. Commun.* 185 (2014), pp. 2250–2300. DOI: 10.1016/j.cpc.2014.04.012 (cited on page 38).

[107] C. Andreopoulos et al. “The GENIE Neutrino Monte Carlo Generator: Physics and User Manual”. In: (2015) (cited on pages 42, 53).

[108] M. Glück, E. Reya, and A. Vogt. “Dynamical parton distributions revisited”. In: *The European Physical Journal C* 5 (Sept. 1998), pp. 461–470. DOI: 10.1007/s100529800978 (cited on page 42).

[109] A. Bodek and U. K. Yang. “Higher twist, xi(omega) scaling, and effective LO PDFs for lepton scattering in the few GeV region”. In: *Journal of Physics G: Nuclear and Particle Physics* 29.8 (2003), p. 1899. DOI: 10.1088/0954-3899/29/8/369 (cited on page 42).

[110] J.-H. Koehne et al. “PROPOSAL: A tool for propagation of charged leptons”. In: *Computer Physics Communications* 184.9 (2013), pp. 2070–2090. DOI: https://doi.org/10.1016/j.cpc.2013.04.001 (cited on page 42).

[111] Y. Becherini et al. “A parameterisation of single and multiple muons in the deep water or ice”. In: *Astroparticle Physics* 25.1 (2006), pp. 1–13. DOI: https://doi.org/10.1016/j.astropartphys.2005.10.005 (cited on page 42).

[112] D. Heck et al. “CORSIKA: A Monte Carlo code to simulate extensive air showers”. In: (Feb. 1998) (cited on page 42).

[113] T. K. Gaisser. “Spectrum of cosmic-ray nucleons, kaon production, and the atmospheric muon charge ratio”. In: *Astropart. Phys.* 35 (2012), pp. 801–806. DOI: 10.1016/j.astropartphys.2012.02.010 (cited on page 42).

[114] R. Engel et al. “The hadronic interaction model Sibyll – past, present and future”. In: *EPJ Web Conf.* 145 (2017). Ed. by B. Pattison, p. 08001. DOI: 10.1051/epjconf/201614508001 (cited on page 42).

[115] R. Abbasi et al. “Measurement of atmospheric neutrino mixing with improved IceCube DeepCore calibration and data processing”. In: *Phys. Rev. D* 108 (1 July 2023), p. 012014. DOI: 10.1103/PhysRevD.108.012014 (cited on pages 43, 48, 49, 52, 54).

[116] C. Kopper et al. https://github.com/claudiok/clsim (cited on page 44).

[117] D. Chirkin et al. “Photon Propagation using GPUs by the IceCube Neutrino Observatory”. In: *2019 15th International Conference on eScience (eScience)*. 2019, pp. 388–393. DOI: 10.1109/eScience.2019.00050 (cited on page 44).

[118] M. G. Aartsen et al. “Measurement of South Pole ice transparency with the IceCube LED calibration system”. In: *Nucl. Instrum. Meth. A* 711 (2013), pp. 73–89. DOI: 10.1016/j.nima.2013.01.054 (cited on page 44).

[119] G. Mie. “Beiträge zur Optik trüber Medien, speziell kolloidaler Metallösungen”. In: *Annalen der Physik* 330.3 (1908), pp. 377–445. DOI: https://doi.org/10.1002/andp.19083300302 (cited on page 44).

[120] L. G. Henyey and J. L. Greenstein. “Diffuse radiation in the Galaxy.” In: *apj* 93 (Jan. 1941), pp. 70–83. DOI: 10.1086/144246 (cited on page 44).

[121] S. Fiedlschuster. “The Effect of Hole Ice on the Propagation and Detection of Light in IceCube”. In: (Apr. 2019) (cited on page 45).

[122] M. G. Aartsen et al. “In-situ calibration of the single-photoelectron charge response of the IceCube photomultiplier tubes”. In: *Journal of Instrumentation* 15.6 (June 2020), P06032. DOI: 10.1088/1748-0221/15/06/P06032 (cited on page 45).

[123] M. Larson. “Simulation and Identification of Non-Poissonian Noise Triggers in the IceCube Neutrino Detector”. Available at https://ir.ua.edu/handle/123456789/1927. MA thesis. University of Alabama, Tuscaloosa, AL, USA, 2013 (cited on page 45).

[124] M. Larson. “A Search for Tau Neutrino Appearance with IceCube-DeepCore”. available at https://discoverycenter.nbi.ku.dk/teaching/thesis_page/mjlarson_thesis.pdf. PhD thesis. University of Copenhagen, Denmark, 2018 (cited on page 45).

[125] E. Lohfink. “Testing nonstandard neutrino interaction parameters with IceCube-DeepCore”. PhD thesis. Mainz, Germany: Johannes Gutenberg-Universität Mainz, Fachbereich für Physik, Mathematik und Informatik, 2023. DOI: http://doi.org/10.25358/openscience-9288 (cited on pages 46, 75).

[126] M. G. Aartsen et al. “The IceCube Neutrino Observatory: Instrumentation and Online Systems”. In: *JINST* 12.03 (2017), P03012. DOI: 10.1088/1748-0221/12/03/P03012 (cited on page 46).

[127] J. H. Friedman. “Stochastic gradient boosting”. In: *Computational Statistics & Data Analysis* 38 (2002), pp. 367–378 (cited on page 48).

[128] R. Abbasi et al. “Low energy event reconstruction in IceCube DeepCore”. In: *Eur. Phys. J. C* 82.9 (2022), p. 807. DOI: 10.1140/epjc/s10052-022-10721-2 (cited on pages 49, 58).

[129] S. Yu and J. Micallef. “Recent neutrino oscillation result with the IceCube experiment”. In: *38th International Cosmic Ray Conference*. July 2023 (cited on pages 49, 72, 77, 81).

[130] S. Yu and on behalf of the IceCube collaboration. “Direction reconstruction using a CNN for GeV-scale neutrinos in IceCube”. In: *Journal of Instrumentation* 16.11 (Nov. 2021), p. C11001. DOI: 10.1088/1748-0221/16/11/C11001 (cited on pages 49, 50).

[131] J. Micallef. https://github.com/jessimic/LowEnergyNeuralNetwork (cited on page 49).

[132] M. Huennefeld. “Deep Learning in Physics exemplified by the Reconstruction of Muon-Neutrino Events in IceCube”. In: *PoS* ICRC2017 (2017), p. 1057. DOI: 10.22323/1.301.1057 (cited on page 49).

[133] H. Dembinski et al. “Data-driven model of the cosmic-ray flux and mass composition from 10 GeV to 10^{11} GeV”. In: *PoS* ICRC2017 (2017), p. 533. DOI: 10.22323/1.301.0533 (cited on page 52).

[134] G. D. Barr et al. “Uncertainties in atmospheric neutrino fluxes”. In: *Phys. Rev. D* 74 (9 Nov. 2006), p. 094009. DOI: 10.1103/PhysRevD.74.094009 (cited on page 52).

[135] J. Evans et al. “Uncertainties in atmospheric muon-neutrino fluxes arising from cosmic-ray primaries”. In: *Phys. Rev. D* 95 (2 Jan. 2017), p. 023012. DOI: 10.1103/PhysRevD.95.023012 (cited on pages 52, 77).

[136] A. Fedynitch et al. https://github.com/afedynitch/MCEq (cited on page 52).

[137] G. D. Barr et al. “Uncertainties in Atmospheric Neutrino Fluxes”. In: *Phys. Rev. D* 74 (2006), p. 094009. DOI: 10.1103/PhysRevD.74.094009 (cited on pages 52, 53, 77).

[138] F. Riehn et al. “Hadronic interaction model sibyll 2.3d and extensive air showers”. In: *Phys. Rev. D* 102 (6 Sept. 2020), p. 063002. DOI: 10.1103/PhysRevD.102.063002 (cited on page 52).

[139] A. Cooper-Sarkar, P. Mertsch, and S. Sarkar. “The high energy neutrino cross-section in the Standard Model and its uncertainty”. In: *JHEP* 08 (2011), p. 042. DOI: 10.1007/JHEP08(2011)042 (cited on page 53).

[140] Q. Wu et al. “A precise measurement of the muon neutrino–nucleon inclusive charged current cross section off an isoscalar target in the energy range 2.5<E<40 GeV by NOMAD”. In: *Physics Letters B* 660.1 (2008), pp. 19–25. DOI: https://doi.org/10.1016/j.physletb.2007.12.027 (cited on page 54).

[141] M. M. Tzanov. “Precise measurement of neutrino and anti-neutrino differential cross sections on iron”. PhD thesis. University of Pittsburgh, Pennsylvania, Jan. 2005 (cited on page 54).

[142] W. G. Seligman. “A next-to-leading-order QCD analysis of neutrino-iron structure functions at the Tevatron”. PhD thesis. Columbia University, New York, Aug. 1997 (cited on page 54).

[143] Rongen, Martin. “Measuring the optical properties of IceCube drill holes”. In: *EPJ Web of Conferences* 116 (2016), p. 06011. DOI: 10.1051/epjconf/201611606011 (cited on page 55).

[144] R. Abbasi et al. “In situ estimation of ice crystal properties at the South Pole using LED calibration data from the IceCube Neutrino Observatory”. In: *The Cryosphere* 18.1 (2024), pp. 75–102. DOI: 10.5194/tc-18-75-2024 (cited on page 55).

[145] R. Abbasi et al. “Measurement of Astrophysical Tau Neutrinos in IceCube’s High-Energy Starting Events”. In: *arXiv e-prints* (Nov. 2020) (cited on page 57).

[146] M. Usner. “Search for Astrophysical Tau-Neutrinos in Six Years of High-Energy Starting Events in the IceCube Detector”. PhD thesis. Berlin, Germany: Humboldt-Universität zu Berlin, Mathematisch-Naturwissenschaftliche Fakultät, 2018. DOI: 10.18452/19458 (cited on page 57).

[147] P. Hallen. “On the Measurement of High-Energy Tau Neutrinos with IceCube”. MA thesis. Aachen, Germany: RWTH Aachen University, 2013 (cited on page 57).

[148] F. Pedregosa et al. “Scikit-learn: Machine Learning in Python”. In: *Journal of Machine Learning Research* 12 (2011), pp. 2825–2830 (cited on page 64).

[149] V. Barger et al. “Matter effects on three-neutrino oscillations”. In: *Phys. Rev. D* 22 (11 Dec. 1980), pp. 2718–2726. DOI: 10.1103/PhysRevD.22.2718 (cited on page 71).

[150] A. M. Dziewonski and D. L. Anderson. “Preliminary reference Earth model”. In: *Physics of the Earth and Planetary Interiors* 25.4 (1981), pp. 297–356. DOI: https://doi.org/10.1016/0031-9201(81)90046-7 (cited on page 71).

[151] L. Fischer, R. Naab, and A. Trettin. “Treating detector systematics via a likelihood free inference method”. In: *Journal of Instrumentation* 18.10 (2023), P10019. DOI: 10.1088/1748-0221/18/10/P10019 (cited on page 75).

[152] M. G. Aartsen et al. “Computational techniques for the analysis of small signals in high-statistics neutrino oscillation experiments”. In: *Nucl. Instrum. Meth. A* 977 (2020), p. 164332. DOI: 10.1016/j.nima.2020.164332 (cited on page 77).

[153] https://github.com/icecube/pisa (cited on page 77).

[154] R. S. Nickerson. “Confirmation Bias: A Ubiquitous Phenomenon in Many Guises”. In: *Review of General Psychology* 2 (1998), pp. 175–220 (cited on page 78).

[155] H. Dembinski et al. *scikit-hep/iminuit: v2.17.0*. Version v2.17.0. Sept. 2022. DOI: 10.5281/zenodo.7115916 (cited on page 78).

[156] F. James and M. Roos. “Minuit: A System for Function Minimization and Analysis of the Parameter Errors and Correlations”. In: *Comput. Phys. Commun.* 10 (1975), pp. 343–367. DOI: 10.1016/0010-4655(75)90039-9 (cited on page 78).

[157] S. S. Wilks. “The Large-Sample Distribution of the Likelihood Ratio for Testing Composite Hypotheses”. In: *The Annals of Mathematical Statistics* 9.1 (1938), pp. 60–62. DOI: 10.1214/aoms/1177732360 (cited on page 81).